UNIVERSITY OF CALIFORNIA

SANTA CRUZ

HYDROLOGIC AND BIOGEOCHEMICAL DYNAMICS FROM CATCHMENT HEADWATER TO COASTAL GROUNDWATER

A dissertation submitted in partial satisfaction

of the requirements for the degree of

DOCTOR OF PHILOSOPHY

in

EARTH AND PLANETARY SCIENCES

by

Emilio Grande

September 2022

The Dissertation of Emilio Grande is

approved:

_____

Professor Margaret Zimmer, chair

_____

Professor Andrew Fisher

_____

Professor Noah Finnegan

_____

Peter Biehl

Vice Provost and Dean of Graduate Studies

Table of Contents

List of Figures

List of Tables

Abstract

Hydrologic and Biogeochemical Dynamics from Catchment Headwater to Coastal Groundwater

by

Emilio Grande

Understanding surface water and groundwater interactions is fundamental to water resources management as surface and subsurface water is a single resource. However, these interactions are variable and intricate. With a warming planet and changes in recharge patterns (i.e., precipitation) and sea-level rise, it is essential to understand how to sustain precious water resources from watershed headwaters to the coastal ocean. In this thesis, we worked on various topics to address many pressing concerns in hydrologic sciences. The first part, containing Chapters 1 and 2, concentrates on the hydrology and geochemistry at the terrestrial-marine interface, using in-situ high-frequency measurements to understand biochemical processes in salt marsh systems at intra-tidal scales. Chapter 3 seeks to improve understanding of the role of intra-annual catchment storage variation on runoff generation, with a particular interest in watersheds with long-term hydrology that places them close to the threshold between water- and energy-limitation.

Salt marshes are dynamic hydrologic systems where terrestrial groundwater, terrestrial surface water, and seawater mix. These systems play an essential role in global biogeochemical cycles, promoting carbon storage and nitrogen removal due to the saturated conditions resulting from frequent inundation. Salt marsh systems can act as buffers between the terrestrial-marine interface, whereby terrestrially derived nutrients

may be retained or processed, potentially reducing the impacts of these pollutants on coastal environments. These processes are critical as excess nutrients discharged to coastal waters can drive eutrophication and hypoxia, which may worsen with expected shifts in climatic patterns. While our understanding of these systems has improved in recent years, we still have limited knowledge of the spatiotemporal variability of critical biogeochemical drivers within salt marshes. Sea-level rise will continue to force change in salt marsh function, highlighting the urgency of filling this knowledge gap.

A limitation to generating robust water quality knowledge in coastal wetlands is an insufficient understanding of short-time dynamics and limited sampling at timescales over which nutrients are cycled, retained, and transported. We developed an experimental transect in the Elkhorn Slough National Estuarine Research Reserve (ESNERR) to advance understanding of biogeochemical processes and their relationships with hydrology at intra-tidal scales. We instrumented three marsh positions along an elevation gradient that resulted in different degrees of tidal inundation, which we hypothesized would lead to varied biogeochemical characteristics and hydrological interactions.

For Chapter 1, we continuously monitored redox potential, subsurface water levels, and temperature at depths of 10, 30, and 50 cm below the ground surface at each marsh position. To understand how drivers of subsurface biogeochemical processes fluctuate across tidal cycles, we used wavelet analyses to quantify relations between redox potential and water level. We found that tidal forcing significantly affects key drivers of biogeochemical processes, including redox potential variability, likely driving subsurface hydro-biogeochemistry of the salt marsh. Wavelet coherence showed that the redox

potential - water level relationship is non-linear, with a variable lead-lag relationship. We found that precipitation events perturb redox potential at monitored depths over timescales of hours, even though water levels show modest change during events. Chapter 1 highlights the importance of high-frequency measurements, such as redox potential, to elucidate factors that control subsurface geochemistry and hydrological processes in salt marshes.

For Chapter 2, we continuously monitored nitrate concentrations at each marsh position at depths of 10, 30, and 50 cm below the ground surface with subsurface water levels measured from 70 cm below the ground surface wells over seven, ~10-day deployment periods in calendar year 2021. We quantified tidal event hysteresis between nitrate and water level to understand how nitrate concentrations fluctuate across tidal cycles. Marked seasonal wet/dry periods common in California's climate caused significant hysteresis in nitrate-water level variations. In dry periods, hysteresis was generally clockwise, indicating a limited, proximal nitrate source that is not replenished over the event, or nitrate consumption over the tidal event. This contrasts with wet-period hysteresis, where generally counterclockwise hysteresis suggests water contributions with higher nitrate concentrations from potentially distal sources or in situ nitrogen processing. This study shows that multi-scale hydrologic control nitrate dynamics may influence ecological processes in coastal environments.

In Chapter 3, we advance understanding of the critical role of intra-annual storage variations for runoff generation across multiple watersheds over the hydroclimatic spectrum. We studied runoff generation as a function of catchment storage in four watersheds, focusing on two catchments close to the water-/energy-

limitation threshold to identify how year-to-year storage variability influenced intra-annual runoff generation efficiency variations. Primarily, we focused on one energy-limited catchment in the humid subtropics and one water-limited catchment in a Mediterranean climate. We utilized daily catchment water balances to calculate daily variations in the relative magnitude of storage. We analyzed runoff and precipitation events to draw connections between catchment storage depth and runoff generation and compared findings to the same metrics in two intensely energy-limited landscapes.

We observed a distinctive shape in daily storage across years in the threshold catchments: with distinct wet-up, plateau, and dry-down stages. For landscapes in the threshold of water-/energy-limitation, the extent of annual changes in storage was a considerable fraction of the water balance, in sharp contrast to the intensely energy-limited catchments. As characterized by event and monthly runoff ratios, runoff generation varied as a function of storage state in the threshold landscapes. Higher runoff ratios during the plateau differed from lower runoff ratios during the wet-up and dry-down stages. Depending on the storage stage, we observed that the same storage amount was partitioned to evapotranspiration or runoff differently throughout the year. Despite their different positions on opposite sides of the threshold, the similarity between the two focus catchments suggests a potential characteristic behavior of systems at the threshold common to both humid and semi-arid landscapes. This work sheds light on the intra-annual variability of catchment storage and its role in runoff generation. Our approach will prove helpful under a changing climate as shifts between water/energy-limitation are likely to become more common in watersheds at the threshold

Acknowledgments

A mi madre, Raquel del Valle, quien se ha sacrificado por mi y me ha dado todo sin pedir nada a cambio. Gracias, madre. I dedicate this work to my mother. She has given me everything and does not expect anything in return, and that is the encouragement that pushes me forward, makes me resilient, and keeps me going. I also want to dedicate this work to Nina (Yelina), my beloved niece. This work would not have been possible without the invaluable support of my partner, Jenna Hadick. Thank you for always finding something to celebrate, even the smallest victories.

To my friend Eliso: Who is no longer with us. 2021 had some extremely cruel moments. Whenever I am sad, I close my eyes and think of Eliso. I think about when he would do funny things when we were in college together when we did not know that life could be so short. And like back then, Eliso makes me smile. We love you, Chicho. You were always the best of friends.

In my life, I have been blessed by the opportunity to work with great scientists and mentors. My advisor, Margaret Zimmer, has been influential in my scientific career and the overall development of this thesis. Thank you, Margaret. Margaret is responsible for giving me a new set of hydrology-colored glasses to look at the world with. Over the past three years working with Margaret, I have grown to be a better scientist, and I have learned to think critically about the world and hydrologic systems. I have learned that science is not only about facts, values, and elemental equations. I learned that science is also about people and collaboration. This work would not have been possible without you. You gave me the freedom to pursue diverse research goals, and this thesis is only

the beginning of our work together. I appreciate all the time you have spent reading my grant proposals and my manuscripts. Hopefully, there will be many more of those.

I would also like to thank Andy Fisher. Every time I have a conversation with Andy, I learn as much as if I had read a book. Andy, I appreciate your patience and humility when teaching hydrogeologic concepts. You make groundwater modeling look easy. I have learned a big deal from you, and I hope that I might be capable of being as good a teacher as you are one day.

I have truly enjoyed my interactions with all the faculty members from the Earth Sciences Department. Thus, I would like to thank them. Particularly, I want to thank Noah Finnegan for his helpful advice and comments before and during my qualifying exam. I feel like Covid robbed me of the opportunity to spend more time in the field with Noah and learn more from him. Nevertheless, I am grateful for the interactions that we did have. I also want to thank Matthew Clapham. Matthew, thank you for teaching me R, you have changed my life.

Thank you to my scientific "mother" and my M.Sc. advisor, Jean Moran. Jean has always been there for me, even after I "left" her lab. She has always supported me. From borrowing instruments to conversations that extend for hours, it is always a pleasure to spend time and learn from her. Thank you, Jean.

I am also grateful for our scientific family in the Zimmer lab. Encouragement by other lab members has kept me going over the past couple of years. It is a privilege to work alongside such talented scientists that have helped me in my short career and have inspired me to continue my career in academia.

I want to express my deepest gratitude to the NITRATES team. This fantastic group of scientists is an inspiration and has helped me understand coastal areas' hydrology and biochemistry. Especially, I want to thank Bhavna Arora for her support and guidance in the first chapter of this thesis. Bhavna and I met weekly for many months while I learned how to perform and interpret wavelet analysis and information theory. Further, I want to thank Erin Seybold for teaching me everything I know about using optical probes to measure high-frequency nitrate. The second chapter of this thesis came together thanks to Erin's efforts and support over the past three years. In addition, I want to thank Corianne Tatariw for her helpful feedback and comments about biochemical processes in wetlands. In my short career, I have never enjoyed reading feedback from a collaborator as I enjoy Corianne's insightful and funny comments. I want to thank Ate Visser for his support throughout my MSc and Ph.D. I have been lucky to work closely with Ate for the past five years, and I am always amazed by all the knowledge that Ate shares with me. The first chapter of this thesis received significant feedback from Ate, and I am grateful for his support.

Thanks also to John Mallard for his support over the past two years. I met John through Margaret at AGU 2019. From a figure in an AGU poster, we developed the manuscript that now is part of Chapter 3 of this thesis. John spent many (many) hours meeting with us over the past two years. I have truly enjoyed working with John, and I am looking forward to more collaborations.

Finally, I am extremely grateful for the funding that enabled this work. I was funded under a Cota-Robles fellowship, a NOAA Margaret A. Davidson fellowship, and a Casey Moore Fund award. Further the work presented in the first two chapters of this

dissertation was partially funded by the California SeaGramt and the U.S. Department of Energy.

Chapter 1 -Tidal frequencies and quasiperiodic subsurface water level variations dominate redox dynamics in a salt marsh system

1.1 Abstract

Salt marshes are hotspots of nutrient processing en route to sensitive coastal environments. While our understanding of these systems has improved over the years, we still have limited knowledge of the spatiotemporal variability of critical biogeochemical drivers within salt marshes. Sea-level rise will continue to force change on salt marsh functioning, highlighting the urgency of filling this knowledge gap. Our study was conducted in a central California estuary experiencing extensive marsh drowning and relative sea-level rise, making it a model system for such an investigation. Here we instrumented three marsh positions subjected to different degrees of tidal inundation (6.7%, 8.9%, and 11.2% of the time for the upper, middle, and lower marsh positions, respectively), providing locations with varied biogeochemical characteristics and hydrological interactions at the site. We continuously monitored redox potential (Eh) at depths of 0.1, 0.3, and 0.5 m, subsurface water levels (WL), and temperature at 0.7 m depth at each marsh position. To understand how drivers of subsurface biogeochemical processes fluctuate across tidal cycles, we used wavelet analyses to explain the interactions between Eh and WL. We found that tidal forcing significantly affects key drivers of biogeochemical processes by imparting controls on Eh variability, likely driving subsurface hydro-biogeochemistry of the salt marsh. Wavelet coherence

showed that the Eh-WL relationship is non-linear, and their lead-lag relationship is variable. We found that precipitation events perturb Eh at depth over timescales of hours, even though WL show relatively minimal change during events. This work highlights the importance of high-frequency in situ measurements, such as Eh, to help explain factors that govern subsurface biogeochemistry and hydrological processes in salt marshes.

1.2 Introduction

Coastal wetlands are dynamic hydrologic systems where terrestrial groundwater, terrestrial surface water, and seawater mix. These systems play an important role in global biogeochemical cycles, promoting both carbon storage and nitrogen removal, in part due to the saturated conditions resulting from frequent inundation (Valiela and Cole, 2002; Giblin *et al.*, 2013; Reading *et al.*, 2017). Despite the importance of the dynamic hydrology in marshes, the bi-directional hydrologic interaction between terrestrial and marine sources is poorly understood.

Currently, one of the biggest impediments to developing robust water quality knowledge in coastal wetlands is an incomplete understanding of short-time dynamics and a lack of sampling at timescales over which nutrients are removed, retained, and transported. A first step towards improving this understanding is to determine the time scales at which surface-subsurface hydrologic interactions occur in salt marshes, as hydrologic forcing is likely an important driver of nutrient cycling and overall biogeochemistry (Guimond *et al.*, 2020b; Guimond and Tamborski, 2021). Documenting the current temporal variability of these interactions and associated nutrient

concentrations will further aid in predicting future conditions in these dynamic coastal systems under a changing climate (Crotty *et al.*, 2020; Buffington *et al.*, 2021).

Available nutrients and other biogeochemical parameters in salt marshes are usually limited to synoptic, irregular sampling, or long-term but coarse resolution such as monthly time series (Reading *et al.*, 2017). Further, hydrologic forcing like storms and tidal inundation, which drive biogeochemical parameters, are short-lived, episodic events that may be missed by coarse resolution sampling. Although recent efforts have focused on measuring nutrient concentrations at high temporal resolution using sensors (Birgand *et al.*, 2016; Messer *et al.*, 2019; Liu *et al.*, 2020a), these remain uncommon due to the difficulty and high costs associated with collecting these datasets. A promising solution to studying rapid temporal hydrological and biogeochemical variations in salt marshes is to use continuous *in situ* redox potential (Eh) measurements. Eh describes the energetic favorability of a reaction and indicates the dominant geochemical conditions or potential for carbon loss via oxidation. For example, high Eh values are indicative of aerobic or oxygenated conditions. *In situ* Eh measurements are comparatively easy and cheap to collect (Wallace *et al.*, 2019; Guimond *et al.*, 2020a), and using several probes can help capture the extensive spatial variability in salt marsh systems with respect to surface-subsurface hydrologic interactions.

Eh variability in salt marshes has been linked to sediment characteristics, temperature, and hydrologic forcing (Vorenhout *et al.*, 2004), but hydrology has been shown to be the most significant control on Eh as it is related to oxygen availability (Ensign *et al.*, 2008). This is because surface waters (or waters in contact with the atmosphere) have relatively high dissolved oxygen (DO) levels compared to subsurface

water. DO is an important indicator of water pollution as it is critical for aerobic respiration (Boyd, 2000). Low DO levels are commonly found in wetlands as they are subjected to frequent submersion and contain abundant decomposing organic material (Hammer and Bastian, 1989; Steinmuller and Chambers, 2019; Orduña-Gaytán *et al.*, 2022). Further, previous work has shown that Eh can be an indicator of hydrological processes. Eh has been used to represent localized advective oxygen transport in forested wetlands as high Eh represents oxygen-rich flow paths (Lahiri and Davidson, 2020). Three-dimensional monitoring of Eh showed that high Eh conditions persist along high-permeability preferential flow paths where oxygenated surface water can easily flow in a shallow riparian aquifer (Wallace and Soltanian, 2021). Additionally, tidal inundation in coastal environments were observed to have a strong relationship with denitrification rates and consequently Eh variations (Ensign *et al.*, 2008). Therefore, combining high-resolution *in situ* Eh measurements with inundation extent can be used to evaluate the frequency at which biogeochemical processes occur and the timescale at which porewater and subsurface water interact in these salt marsh systems.

Because biogeochemical processes in salt marsh porewater are complex, nonlinear, and rapid, changes to measured Eh can simultaneously signal the influence of multiple drivers, such as water level. Wavelet analysis has been shown to be useful for carrying out this timescale analysis of water chemistry parameters (Kumar and Foufoula-Georgiou, 1997; Arora *et al.*, 2016). Wavelet transform is used to decompose a time series signal into time and frequency domains simultaneously (Foufoula-Georgiou and Kumar, 1994; Torrence and Compo, 1998). Because of this capability of time-frequency localization, wavelet analyses can determine discontinuities, seasonal trends, and long-

term patterns in the time series (Daubechies, 1992). For example, wavelet analysis has been used with diverse hydrologic parameters to study runoff generation in response to timing and magnitude of precipitation (Kantelhardt *et al.*, 2003; Partal, 2012). Wavelet transforms of temperature were also used to identify hotspots of submarine groundwater discharge (Henderson *et al.*, 2008). Moreover, this method has been used to understand redox dynamics and solute concentrations in a diversity of settings, from a municipal landfill site to a uranium-contaminated Department of Energy field site (Martínez and Gilabert, 2009; Arora *et al.*, 2013, 2016). In coastal environments, wavelet transform has been applied to periodic water quality measurements to assess the area's environmental health over several years (Venkatesh *et al.*, 2021). In addition, wavelets were used on continuous Eh data in a tidal river to assess hydrologic forcing on biogeochemistry over different timescales (Wallace *et al.*, 2019).

Given this technique's strengths and applicability, we use wavelet transform of continuous Eh and shallow subsurface water level measurements. To advance understanding of the spatiotemporal variability of hydrological and biogeochemical processes in coastal systems, we address the following questions:

1- Is there spatiotemporal variability at intra/intertidal scales in salt marsh subsurface hydrology and biogeochemistry?

2- What is the role of seasonal climatic factors, such as precipitation, for salt marsh biogeochemistry?

3- What are the drivers of redox conditions and their role in subsurface hydrology?

1.3 Methods

1.3.1 Site Description

This study was conducted at the Elkhorn Slough National Estuarine Research Reserve in Monterey, California (Figure 1.1A). The Mediterranean climate of Elkhorn Slough has pronounced wet/dry seasonal dynamics, which provide an ideal setting to understand the diel and seasonal variations in climatic forcing that impact subsurface inundation and biogeochemical conditions. During this study (Feb 2020-March 2021), air temperature varied between 0.3 ºC and 35.4 ºC, while water temperature ranged between 10.7 ºC and 19.1 ºC. Water levels were also variable, ranging between 0.57 m above the ground surface (during high tides, 2.17 m amsl) and 0.24 m below the ground surface (1.35 m amsl), reflecting the daily tidal inundations. Water levels during the study period had a mean, median, and standard deviation of 1.58 m amsl, 1.58 m amsl, and 0.09 m amsl, respectively. Total precipitation over the study period totaled 396.8 mm.

Our work focused on a 25 m experimental transect in an emergent wetland (Figure 1.1A, black star). The site was delineated into upper, middle, and lower marsh positions through elevation surveys and inundation extents, with an elevation difference of 0.24 m over a 24 m profile (Figure 1.1D). The elevations above mean sea level of each marsh position are 1.79 m, 1.65 m, and 1.55 m for the upper, middle, and lower marsh, respectively. These elevations are inundated 6.7 %, 8.9 %, and 11.2 % of the time, respectively, based on water level data collected at the site between February 2019 and February 2021. These wetland positions coincide with previous delineations of salt marshes across the Elkhorn Slough estuary based on vegetation coverage by elevation (Woolfolk and Labadie, 2012), and thus, are representative of the estuary. Native

pickleweed (*Salicornia pacifica*) dominates the marsh area (Van Dyke and Wasson, 2005), underlain by partially decomposed organic soils. For this study, we focus on temporal variations in Eh from these three locations that have distinct inundation regimes, vegetation activity/coverage, and micro-topography and that are representative of common/dominant landscape positions found across emergent wetlands at Elkhorn Slough.

We analyzed soil bulk density at depth in each marsh position at 0.05 m intervals (Figure 1.1B). The density measurements showed an increase in density from the surface down to 30 cm depth, where the bulk density was highest (Figure 1D). From 30 cm depth down to 50 cm, the bulk density of the soil decreased to values similar to the surface. Bulk density decreased from the upper marsh to the lower marsh position (Figure 1.1D).

We developed a network of co-located observation wells at each marsh position to study water fluctuations across the site (Figure 1.1D). We installed the wells to a depth of 0.7 m by pushing the PVC pipe directly into the ground to minimize gaps around the pipe, which could cause artificial water movement vertically along the well's annulus. The wells were screened from 0.05 m below the surface to the bottom of the well and water level and temperature were recorded with Solinst pressure transducer loggers (Ontario, Canada) at 5-minute intervals. Air pressure was also measured in the transect at 5-minute intervals to barometrically correct the water pressure measurements. For simplicity, the water level and temperature were averaged at hourly intervals.

We installed Eh probes (Paleo Terra, Amsterdam, Netherlands) next to each observation well (~1 m apart) to capture the range of Eh fluctuations over tidal and seasonal cycles and use them to indicate the possible dominant biogeochemical processes occurring at different time scales. The Eh probes consist of fiberglass-epoxy tubes embedded with an array of 3 platinum electrodes and a reference electrode filled with a potassium chloride solution used as a standard for the measurements (Figure 1.1C). Eh was measured at 0.1, 03, and 0.5 m depths below the ground surface (Figure 1.1D). Measurements were recorded at 1 min intervals between March 1st, 2020 and February 26th, 2021. We calculated the variance over the course of the study period for the Eh time series to control for measurement drifts. Similar to other data, these time series were also averaged to hourly intervals. Eh values were not corrected for pH. In addition, we installed a deep piezometer at 3.5 m below the surface in an upland location (in the same profile but ~8 m from the salt marsh, Figure 1.1B), with no influence from the daily tides. The piezometer was completed with a 0.15 m screen at the bottom. We continuously measured water level in this piezometer at 5 minute intervals to monitor fluctuations in the regional terrestrial groundwater level and evaluate the potential for fresh subsurface water to move laterally towards the salt marsh.

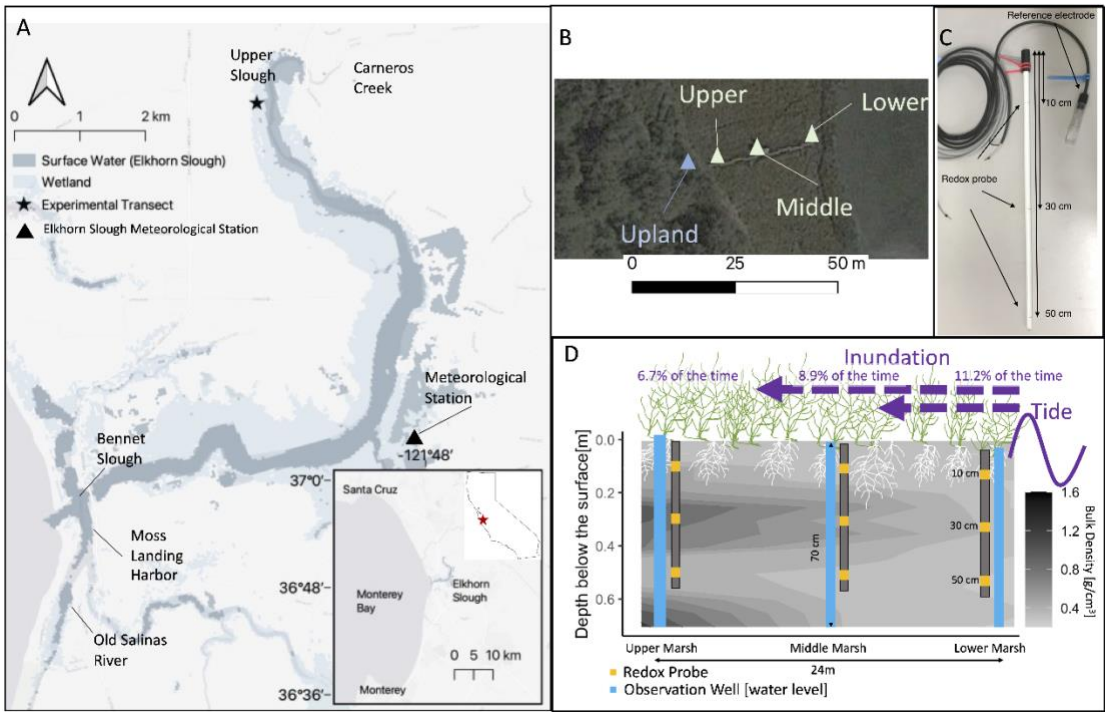

Figure 1.1 A) Map of Elkhorn Slough with the extent of wetlands outlined in light blue. The black star marks the location of the study transect. B) Map view of the experimental transect showing the location of the upland monitoring piezometer in relation to the salt marsh transect. C) Labeled diagram of the redox probe and reference electrode used for this project. D) Illustration of the experimental transect showing the spatial distribution of the redox (Eh) probes and observation wells with a contour plot overlay of sediment bulk density across the salt marsh. The darker the colors in the contour plot, the greater the bulk density (highest around 30 cm at all three marsh positions).

1.3.2 Ancillary Data

Eh is related to the concentration of different redox pairs in the soil, and oxygen is the first acceptor that plays a critical role in Eh variability (Vorenhout *et al.*, 2004). Although oxygen is introduced into the soil through diffusion and radial oxygen loss in the rhizosphere (Adema and Grootjans, 2003)(Koop-Jakobsen and Wenzhöfer, 2015). Thus, we expected that tidal processes (described above) and weather conditions would

be the dominant drivers of Eh in the soil. To account for weather-driven oxygen inputs, we included hourly meteorological data, obtained from the Elkhorn Slough Meteorological Station (Figure 1.1A) in our study. The station is managed and maintained by the National Estuarine Research Reserve System (NERR, 2021). Our analyses used relative humidity, barometric pressure, precipitation, wind speed, total photosynthetically active radiation, and air temperature. These parameters associated with weather conditions have been observed to explain Eh variability in non-tidal inundated systems, mainly a paddy field (Minamikawa and Sakai, 2007) and also in waterlogged peats (Haavisto, 1974).

To further study the role of vegetation on Eh, we included hourly potential evapotranspiration (*ET*). *ET* was obtained from the California Irrigation Management Information System (CIMIS), which is maintained by the California Department of Water Resources (DWR). *ET* is estimated using the Penman-Monteith equation (Allen *et al.*, 1998). DWR manages a station within 5 km of our experimental transect (Station 129; 36.902779, -121.74193). CIMIS produces estimates of reference *ET* based on hydroclimatic data measured at their stations.

Monthly vegetation surveys were conducted across the experimental transect between October 2020 and September 2021. We used these surveys as a proxy to explore the potential controls of plant productivity on Eh. As mentioned above, pickleweed is the predominant marsh vegetation along our transect. Measurements of pickleweed canopy height, percent live cover, and percent total cover were made over two replicate 0.5 m by 0.5 m plots at each marsh position (n=6).

Considering that animal burrows directly affect salt marsh production, hydrology, and biogeochemistry (Crotty *et al.*, 2020; Guimond *et al.*, 2020a), we used monthly surveys of crab activity between October 2013 and August 2018 in Elkhorn Slough (Beheshti *et al.*, 2021) as a proxy for crab activity in our study. The crab activity study was conducted across the whole estuary and not limited to our transect. Further, crab counts were performed monthly. Therefore, these data were considered as a proxy for seasonal crab activity. *Pachygrapsus crassipes* is the dominant marsh crab in Elkhorn Slough (Beheshti *et al.*, 2022), with burrow densities often over 200 per m^2 in lower marsh positions (Beheshti *et al.*, 2022). Additionally, burrowing by *P. crassipes* has been shown to have a significant negative effect on bulk density and belowground biomass (Beheshti *et al.*, 2022). Evidence from a concurrent study showed that in the marsh interior, burrowing by P. crassipes hastens marsh recovery, likely due to improved drainage that ameliorate stressors associated with ponding, such as anoxia or sulfide toxicity (Beheshti et al. 2022). Total catch per unit effort (i.e., four pit-fall traps surveyed per 2 m by 1 m plot of marsh) were used to evaluate seasonal changes in crab activity and study their relationship with seasonal changes in Eh. Trapping data was conducted along the marsh edge of tidal creeks (n=5) that span from the mid to upper reaches of the estuary (Beheshti *et al.*, 2022).

1.4 Methodology

Redox reactions often show significant spatiotemporal variability (Vorenhout *et al.*, 2004, 2011; Guimond *et al.*, 2020a). High frequency Eh measurements can explain factors that govern subsurface biogeochemistry and hydrological processes in salt

marshes. The use of principal component analysis, correlations, or other statistical techniques to examine biogeochemical data sets cannot always recognize the processes driving this variability as they lack the ability to incorporate temporal changes (Nezlin *et al.*, 2009).

In coastal systems affected by sea-level rise, there is a growing need to constrain biogeochemical processes to predict future scenarios (Ward et al., 2020). Continuous wavelet transform (CWT) is a promising tool for timescale analysis of water quality and hydrodynamics. CWT has been used to explain variabilities in water quality in coastal estuaries (Venkatesh et al., 2021). However, Venkatesh et al. (2021) used monthly samples of water quality, which allowed them to explain long-term variabilities, such as processes driving annual changes. The short-term variability of hydrological and biogeochemical processes, at time-scales over which nutrients are transformed, has been less studied. Recently, (Regier et al., 2021) used wavelet coherence on sub-hourly water level and salinity measurements to understand hydrologic connectivity between tidal creeks and floodplains in coastal systems. They found temporal variation in the lateral and vertical connectivity between the two, with neap tides controlling lateral connectivity, particularly during the dry season, and vertical connectivity dominated during spring tides. Our study uses a similar high-frequency measurement. However, in addition to improving our understanding of the hydrologic functioning of the shallow subsurface in the salt marsh, we linked the hydrologic processes to short-term variability in Eh. Here we explain variability in Eh, a key driver of biogeochemical processes, at time scales that can resolve the effects of tidal forcing in salt marsh subsurface hydrology and geochemistry. This application of CWT is significant as it can help identify potential

control points, hot spots, and hot moments in marsh nutrient transformations. Therefore, the aim of the wavelet analyses was to 1) extract the complex linkages among biogeochemical drivers (e.g., Eh) and other environmental factors (e.g., subsurface hydrology); and 2) identify the temporal scales at which they exert dominant control using CWT, which has been found to be a powerful analytical tool (Alexander *et al.*, 2020).

1.4.1 Wavelet Analysis

As suggested above, we used wavelet analysis to analyze the measured Eh patterns and identify dominant scales of variability across the three studied marsh positions. In particular, we used multilevel decomposition to understand the hydrologic processes dictating patterns of biogeochemical drivers at different timescales.

1.4.1.1 Time-frequency processing

Wavelet transform is one of the most commonly used time-frequency analysis techniques for studying multiscale, nonstationary processes over spatial and temporal scales (Addison, 2005; Beecham and Chowdhury, 2010). CWT is obtained by decomposing the data *D(t)* with a wavelet function $\psi(t)$ and creating wavelet coefficients *W* that designate the relationship among the wavelet function and the data:

$$W_D(a,b) = \int_{-\infty}^{\infty} \Psi_{a,b}^{*}(t) D(t) dt \quad (1.1)$$

where *t* is time, * is the complex conjugate of the wavelet function, illustrated by:

$$\Psi_{a,b}(t) = \frac{1}{\sqrt{a}} \Psi\left(\frac{t-b}{a}\right), a > 0, -\infty < b < \infty \quad (1.2)$$

where *a* is the scale parameter that determines the dilation or contraction, and *b* is the shift parameter that dictates the location of the wavelet. The flexibility of the wavelet to be stretched and translated in both time and frequency domains helps identify patterns across different time scales (Kumar and Foufoula-Georgiou, 1997). The wavelet must satisfy three central properties:

1- zero mean, $\int_{-\infty}^{\infty} \Psi(t)dt = 0$;

2- unit energy, $\int_{-\infty}^{\infty} \Psi^2(t)dt = 1$;

3- conservation of energy during transformation (Daubechies, 1992).

Several wavelet functions have been described in the literature. Here, we used the Morlet wavelet to derive the dominant frequencies from the Eh time series data. The Morlet wavelet is suitable for feature extraction because it is well localized in space and time (Grinsted *et al.*, 2004), and it has been used in similar datasets (Arora *et al.*, 2013; Wallace *et al.*, 2019; Venkatesh *et al.*, 2021). This wavelet has complex and real elements and facilitates identifying and fine-tuning the significant frequencies (Hariprasath and Mohan, 2008).

1.4.1.2 Local and Global Wavelet

The modulus of the wavelet coefficient is applied to produce a continuous-time power spectrum $p_D(a, b)$described as:

$$p_D(a, b) = W_D(a, b)W_D^*(a, b) = |W_D(a, b)|^2 \quad (1.3)$$

This wavelet power spectrum is helpful as it produces the time-series variance in the frequency and time domains (Guan *et al.*, 2011). The global wavelet can be obtained by calculating the mean of the local power spectrum along the time axis (Torrence and Compo, 1998):

$$W^2(a,b) = \frac{1}{N}\sum_{n=0}^{N-1}|W_D(a,b)|^2 \quad (1.4)$$

where N is the length of the time-series. We calculated a 95% confidence level for the global wavelet spectrum and the significance interval of the contours in the local wavelet, with a significance testing on the background spectrum. Following Torrence and Compo (1998), the distribution of the local wavelet at each time t and scale a is given as:

$$\frac{|W_D(a,b)|^2}{\sigma^2} \Rightarrow \frac{1}{2}P_k\chi_2^2 \quad (1.5)$$

In (1.5), $\chi^2$is the chi-square value obtained for the 95% confidence level, σ^2 is the variance, and P_k is the mean spectrum at the Fourier frequency k that corresponds to a. We used a red-noise background spectrum, which is obtained as (Torrence and Compo, 1998):

$$P_k = \frac{1-\alpha^2}{1+\alpha^2-2\alpha cos(2\pi k/N)} \quad (1.6)$$

where P_k is the background spectrum for red-noise, k (= 0 … $N/2$) is the frequency index, and α is an assumed lag-1 autocorrelation. A 95% significance level for the global wavelet was also calculated using a red-noise background spectrum. The

spectrum of the global wavelet can also be fitted by a chi-square distribution of the form $\frac{\chi_v^2}{v}$, where v (the degree of freedom) is calculated as (Torrence and Compo, 1998):

$$v = 2\sqrt{1 + (\frac{t_{avg}\delta t}{\gamma a})} \quad (1.7)$$

In (1.7), t_{avg} is the number of points averaged over, γ is the empirically calculated decorrelation factor for the mean power across the time axis, and δt is the sampling frequency. We used the R software (R Core Team, 2019) package Biwavelet (Gouhier *et al.*, 2021) for calculating the wavelet spectrums and the confidence intervals. We represented the edge effects of time-frequency (Guan et al., 2011) with a cone of influence, illustrated by the shaded region in the wavelet power spectrum (e.g., Figure 1.3), and omitted it from the analysis.

1.4.1.3 Multilevel Decomposition of Redox Potential

The multilevel decomposition (MLD) allows decomposition of a time series into a number of frequency bands at discrete levels of time scales. At the first step, the time series data is split into two, yielding the high-pass bandwidth (i.e., detailed components), and the low-pass bandwidth (i.e., approximate components; (Quiroz *et al.*, 2011). Each low-pass bandwidth can continue to be decomposed to achieve the next level of hierarchy. This methodology, therefore, allows removing the noise (detailed components) and recovering the data's smoothed trend (approximate components) for each level. The decomposition levels are based upon the sampling frequency and the total length of the time series (Mallat, 1999). The detailed and approximation components are determined by iteratively using a high-pass filter and an associated low-

pass filter, which requires satisfying orthonormality (Labat *et al.*, 2004). A wavelet function $\psi(t)$ composes the high-pass filter in the wavelet transform, and its scaling function $\phi(t)$ determines the low-pass filter. The detailed (D_m) and approximation (A_m) components at a given decomposition level m can be calculated as:

$$D_m(t) = \sum_{k=-\infty}^{\infty} W(m,k)\psi_{m,k}(t) \quad (1.8)$$

$$A_m(t) = \sum_{k=-\infty}^{\infty} S(m,k)\phi_{m,k}(t) \quad (1.9)$$

where S is the scaling coefficient and k is a discrete location index. We used the Daubechies 5 (Db5) wavelet and scaling function, which meets the orthogonality requirement. The approximation and detailed coefficients follow powers of two (i.e., dyadic sampling) to capture the natural frequencies of the Eh data set at 2, 4, 8, 16, and 32-hour scales, respectively. Although frequencies of interest (e.g., tidal frequencies) would be observed at ~12 and ~24-hour scales, these dyadic decomposition levels offer an opportunity to investigate the intertidal cycles seen in the salt marsh. We studied the 16 h approximation component variability and its relationship with other environmental parameters available for this study (see section 2.2). Specifically, we zoomed in around the largest precipitation event of the studied period to estimate the effects of precipitation as a driver of Eh. We used the Wavelet Toolbox from MatLab (The MathWorks, 2021) to obtain the MLD.

1.4.2 Mutual Information

In order to identify the key factors causing temporal variability in the Eh data, we chose to employ mutual information. The mutual information of two random variables

quantifies how much information is obtained about one variable by observing the other variable. Unlike the correlation coefficient, mutual information is not limited to linear dependence (Brunel *et al.*, 2010; Zhang *et al.*, 2012). Mutual information is more comprehensive and defines how different the joint distribution of the two variables (*X*, *Y*) is from the product of the marginal distributions of *X* and *Y* (Shannon and Weaver, 1949):

$$I(X;Y) = D_{KL}(P_{(X,Y)}||P_X \otimes P_Y) \quad (1.10)$$

where *X* and *Y* are random variables (e.g., Eh, water level) with values in the $X \times Y$ space, marginal distributions P_X and P_Y, and join distribution $P_{(X,Y)}$. D_{KL} is the Kullback-Leibler divergence (i.e., reactive entropy, (Cover and Thomas, 2006)). In our study, we used mutual information analysis between Eh and *ET,* subsurface water level in each marsh position, subsurface water temperature in each marsh position, terrestrial groundwater level, precipitation, and the rest of environmental parameters described in section 2.2

In mutual information, the null hypothesis is that $I(X; Y)=0$ (i.e., the two signals are independent). To test the statistical significance of the analysis, we used an equal variance t-test, which is valid for large samples from non-normal distributions and can be used when both data sets consist of the same number of samples and it has been used to test the statistical significance of mutual information analysis (Sarkar and Pandey, 2020). We used a one-tailed test with significance level $\alpha = 0.0001$, which corresponds to a confidence level of ~99.9%.

Further, we normalized *I(X;Y)* to scale the results between 0 (no mutual information) and 1 (perfect correlation). The normalization uses the entropy *H(X)* of each individual signal, and can be calculated as (Kvålseth, 2017; Zbili and Rama, 2021):

$$NMI(X;Y) = \frac{I(X;Y)}{\sqrt{H(X)*H(Y)}} \quad (1.11)$$

And *H(X)* of the discrete random variable *X* is calculated from its probability (*P(x)*) and surprise (*logP(x)*) as:

$$H(X) = -\sum_{i=1}^{n} P(x_i) log P(x_i) \quad (1.12)$$

1.5 Results

1.5.1 Redox Potential Patterns in the Spatiotemporal Domain

There was considerable spatial and temporal variability in Eh across marsh positions and with depth at our salt marsh transect (Figure 1.2). Furthermore, anaerobic conditions (Eh < 250 mV; (Søndergaard, 2009)) dominated the area over the study period across all marsh positions. Eh increased significantly with elevation, with median values of -421 mV, -404 mV, and -377 mV at the lower, middle, and upper marsh positions, respectively (Kruskal-Wallis test: H=9699.3, df = 2, $p < 0.001$). Additionally, median Eh values varied significantly between 10 (median = -387 mV), 30 (median = -424 mV), and 50 cm depths (median = -407 mV) (Kruskal-Wallis test: H=19639, df = 2, $p < 0.001$).

Median Eh was highest at 10 cm and lowest at 30 cm, and this is consistent across the entire measurement period (Figure 1.2). At 10 cm, especially during the wet season (i.e., November-January), the oxygen delivery and consumption processes are readily seen in the Eh profiles (Figure 1.2). During this period, we observed the highest range of Eh values. At all marsh positions, Eh is relatively lower at 30 cm than at 50 cm, except for the middle marsh, where the Eh measurements at 50 cm were consistently lower, suggesting that Eh doesn't continuously decrease with depth but rather is likely related to soil properties, such as bulk density (Figure 1.2). Further, throughout the monitoring period, measurements at the 50 cm depth remained somewhat spatially and temporally constant (~ -400 mV), highlighting the lower Eh variability at depth in salt marsh sediments.

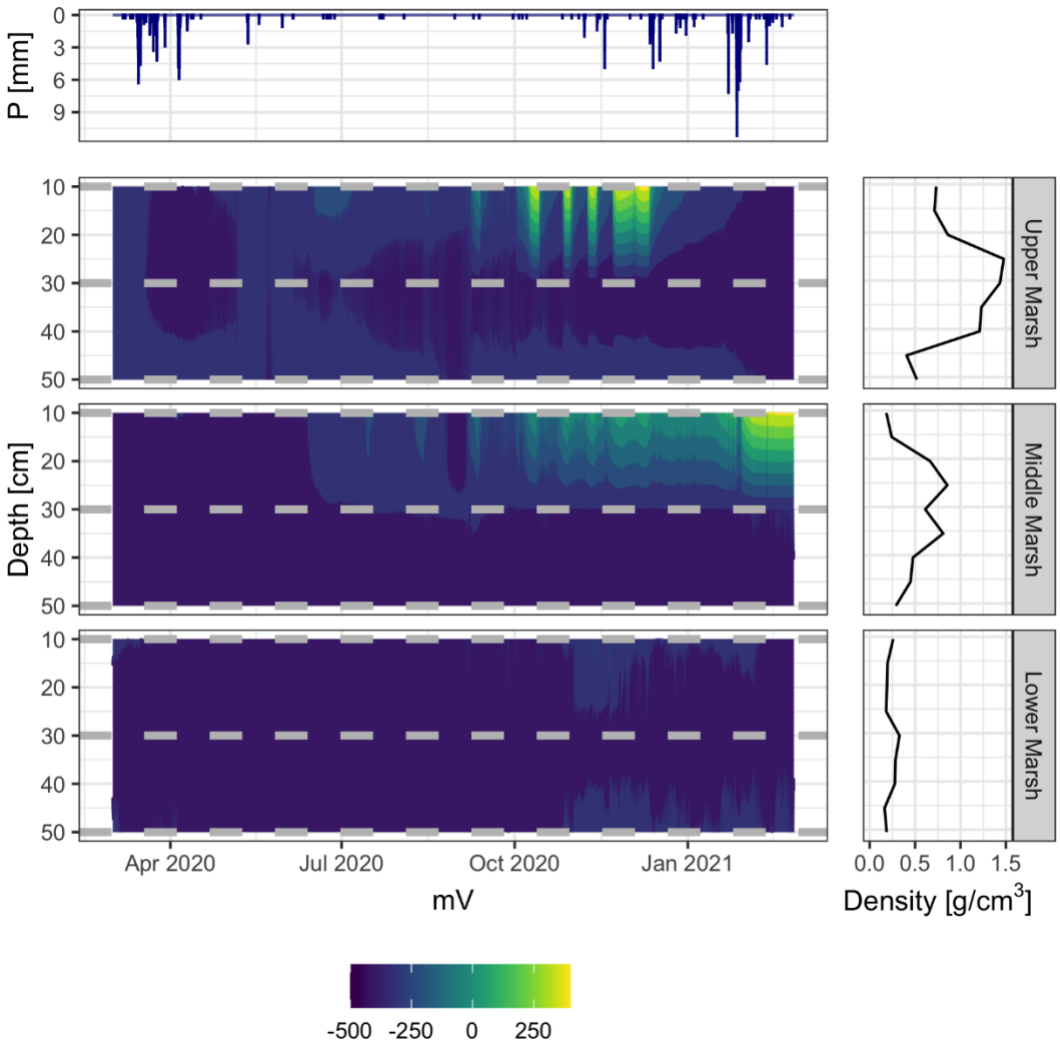

Figure 1.2 Redox potential (Eh) contour graphs across the experimental transect. The grey, dashed lines at 10, 30 and 50 cm indicate the Eh probe's depth, the values in between are linearly interpolated. Soil bulk density at each marsh position is shown to the right of each contour plot. Precipitation time series for the studied period is shown above the Eh profile to illustrate the timing of storm events.

1.5.2 Redox Potential Patterns in the Time-frequency Domain

We studied the temporal variability in Eh as a result of tidal fluctuations using the Morlet wavelet (Figure 1.3). Based on the Morlet wavelet, all marsh positions and depths studied show dominant powers at periods of 12 h and 24 h (areas marked with black polygons in the CWT, or with powers above the red dashed line in the global wavelet spectrum, which mark the 95% confidence level, Figure 1.3). The significant powers at the 12 and 24 h periods coincide with the sub-daily and daily tidal frequencies (Taniguchi, 2000), suggesting a relationship between the water level in the salt marsh (i.e., inundation extents) and Eh measurements.

At 10 cm depth, significant powers at specific tidal frequencies (12 and 24 h periods in Figure 1.3, Table 1.1) are seasonal; significant powers start in August 2020 and stop during the winter months. The significant powers start earlier in the upper and middle marsh than at the lower marsh position. In addition to significant powers at (sub)daily tidal cycles, the CWT of the 10 cm probes showed significant powers at larger periods of ~708 h (29.5 days) and ~355 h (14.8 days), corresponding with the lunar cycles (Figure 1.3; (Taniguchi, 2000)). However, significant powers at these frequencies are not observed at other depths.

At 30 cm, Eh measurements showed different patterns in the CWT across marsh positions. In the upper marsh position, the CWT shows significant powers at 12 and 24 h periods continuously from April through October 2020. The middle marsh position showed significant powers for a limited time (predominantly in summer, Figure 1.3, Table 1.1), and only the ~24 h period is significant in the global wavelet. In the lower marsh position, Eh displayed significant powers at tidal frequencies (~12 and ~24 h

periods) throughout the studied period (Figure 1.3). No lunar cycle frequencies are observed at this depth.

Table 1.1. Summary of periods (frequencies) at which significant powers in the Eh wavelet occur.

		Significant Periods	
Depth (cm)	***Lower Marsh***	***Middle Marsh***	***Upper Marsh***
10	1:64 h & > 512 h	12h and 24h (tidal frequencies)	12h and 24h (tidal frequencies), 355h and 708h (lunar cycle)
30	12h and 24h (tidal frequencies)	24h (daily cycle)	12h and 24h (tidal frequencies)
50	12h and 24h (tidal frequencies), 355h and 708h (lunar cycle)	12h and 24h (tidal frequencies), 355h and 708h (lunar cycle)	12h and 24h (tidal frequencies)

The CWT of Eh at 50 cm displayed temporal and spatial variability. In the upper marsh, Eh measurements show significant powers at tidal frequencies only during some days in May, July and August 2020 (Figure 1.3). However, in the middle marsh position, significant powers at tidal frequencies show a gap between July and August 2020. During that period, the middle marsh showed significant powers at frequencies associated with the lunar cycle (Figure 1.3, Table 1.1). The lower marsh position also showed a gap in the significant powers of tidal frequencies, however the gap started in June and ended in October 2020.

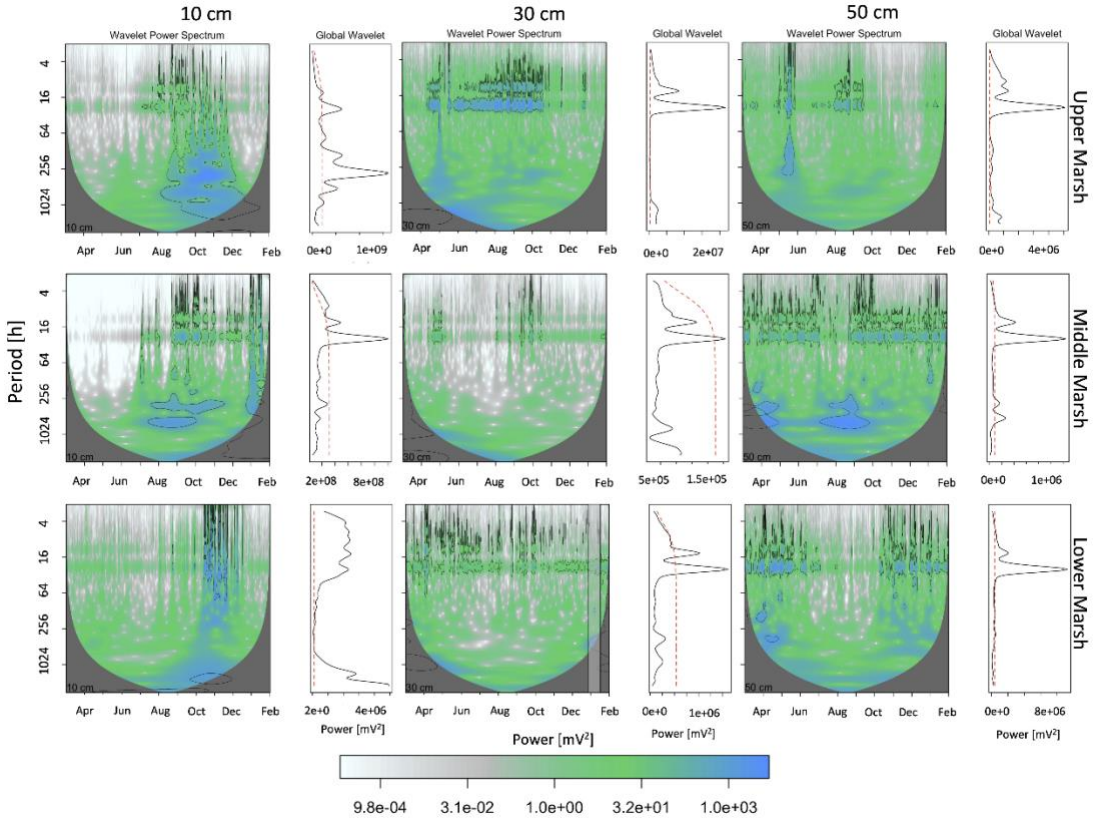

Figure 1.3 Continuous wavelet spectrum and global wavelet spectrum of Eh time series between March 2020 and February 2021. In the wavelet spectrum, the shaded regions signify the cone of influence. The color bar signifies the strength of power in the wavelet spectrum. Areas surrounded by the black polygons display significant powers (within 95% significance level). In the global wavelet spectrum, the red-dashed line is the 95% significance level using a red-noise background spectrum. The shaded area in the 30 cm depth of the lower marsh (bottom center panel) marks the time of a precipitation event studied in detail in Figure 5.

1.5.3 Controlling Processes

Based on the mutual information analysis, regional terrestrial groundwater level, subsurface water temperature and subsurface water level in the salt marsh share the most information with Eh, with normalized mutual information (NMI) of 0.99, 0.98, and 0.97, respectively (Figure 1.4). These parameters are followed by air temperature and total PAR, with NMI of 0.71 and 0.63, respectively (Figure 1.4). Precipitation and Eh share

low mutual information, with NMI of 0.03 (i.e., these two time series are somewhat independent). Here, we illustrate the results from the mutual information analysis only for the lower marsh position, but other marsh positions had similar results.

The temporal variability of the 16 h approximation coefficients was graphically compared with the most significant parameters from the mutual information analysis to identify and temporally separate the processes affecting Eh's dominant frequencies (Figure 1.5). Here, we zoom-in to show data between January 20th and February 10th, 2021, corresponding to dates around one of the few precipitation events of the 2021 water year in the area (Figure 1.5). The precipitation event totaled 147.6 mm in 3 days with a maximum intensity of 11.2 mm/h. During this focal period, Eh and ET were out of phase (Figure 1.5A). ET ranged between 0 and 0.8 mm/h, with a mean, median, and standard deviation of 0.13 mm/h, 0.1 mm/h, and 0.2 mm/d, respectively. The maximum daily Eh value occurred at times of minimum ET (at night). Subsurface water temperature displayed a relatively low temporal variability, contrasting with air temperature values for the site, as would be expected (Figure 1.5B).

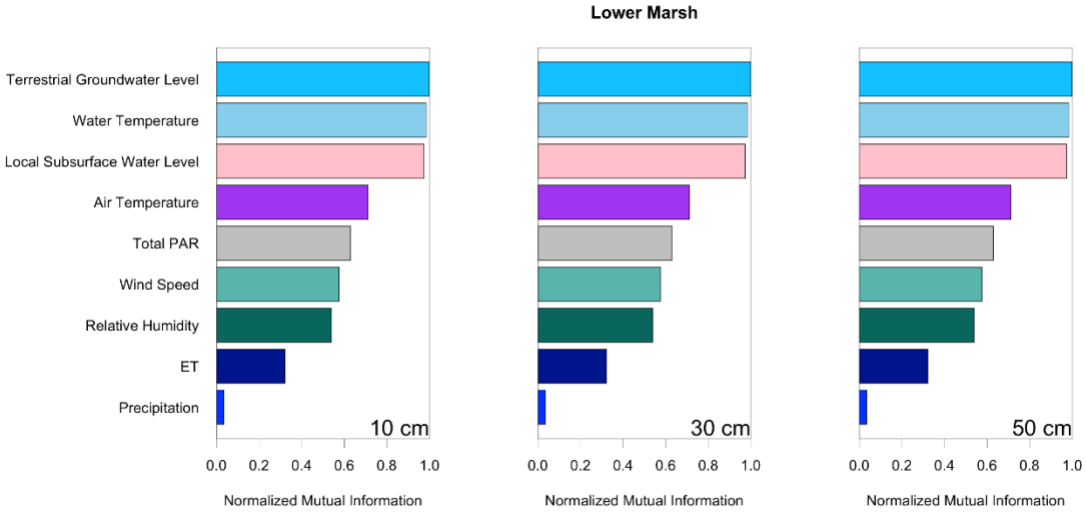

Figure 1.4 Mutual information between Eh time series and other hydroclimatic parameters used to explore Eh's temporal variability. All the relationships between Eh and the parameters shown in the figure are statistically significant (p-value <0.0001). The mutual information values are normalized by the Entropy of each individual signal.

During the period shown in Figure 1.5, the lead-lag relationship between subsurface water level and Eh is observed to be variable. For example, the maxima in water level and Eh are in phase in the first two days, but the two variables are out of phase for the remaining period. The regional terrestrial groundwater level varied (i.e., increased) rapidly in response to precipitation events (Figure 1.5B). Over the whole study period, the water table fluctuated between 1.77 m amsl (in the dry summer and fall season) and 2.78 m amsl (in the wet winter season), with a mean, median, and a standard deviation of 2.23 m amsl, 2.19 m amsl, and 0.30 m amsl, respectively. The regional terrestrial groundwater level is generally higher than the subsurface water level in the salt marsh. The regional terrestrial groundwater level is only lower than the subsurface water level during king tides in very dry periods.

Note that the detailed components (d1, d3, d3, d4, and d5) represent the "noise" in data at each scale and were therefore removed from the analysis. This can be further confirmed from Figure 1.5C where the detailed components are damped during the precipitation event, and amplified otherwise.

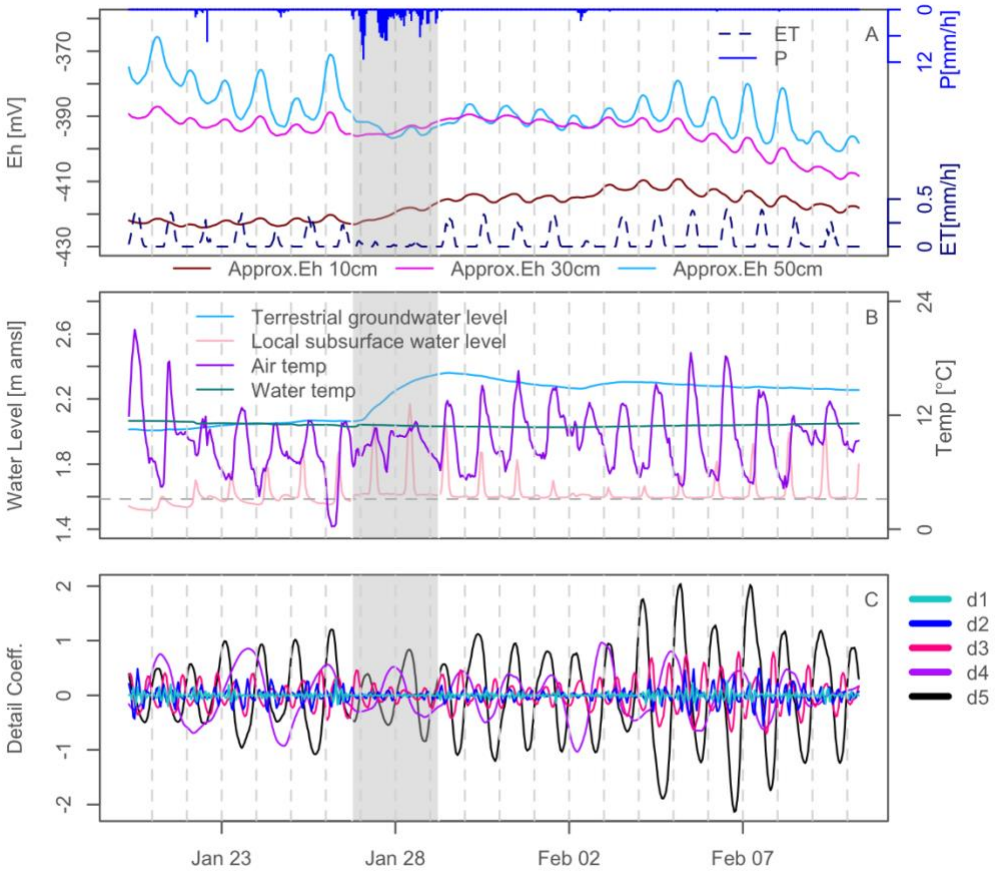

Figure 1.5 Multilevel decomposition of Eh for the 10 cm, 30 cm, and 50 cm depths in the lower marsh position between January 20th and February 10th, 2021 (marked in Figure 3 by a shaded rectangle). A) shows the Eh approximate coefficients at 16 h, hourly precipitation (P), and hourly evapotranspiration (ET). B) shows local subsurface water level, air temperature, water temperature, and regional terrestrial groundwater level. C) shows the detailed components of Eh at dyadic scales of 2 (d1), 4 (d2), 8 (d3), 16(d4), and 32 (d5). The shaded region marks a precipitation event that occurred in the area in late January. The dashed gray line in B) marks the elevation (amsl) of the salt marsh. The vertical dashed gray lines mark the beginning of every new day (midnight).

1.5.4 Wavelet Coherence

Overall, the results of Eh's mutual information and spectral analysis suggest that water level (i.e., tidal inundation) is a critical control in the temporal variability of Eh. In order to further describe the relationship between water level and Eh in the frequency space, wavelet coherence was performed. Here we show the power (modulus) and the phase (angle) for the wavelet coherence between water level and Eh at 30 cm in the lower marsh (Figure 1.6). The wavelet coherence for all other water levels and Eh comparisons showed similar behavior.

Eh and subsurface water levels were significantly coherent at ~12 h and ~24 h periods across most of the studied period (power > 0.8 mV^2 in Figure 1.6). The frequency of high powers (blue color in Figure 1.6) at tidal periods suggests a quasi-periodic relationship between Eh and subsurface water level. We also observed significant coherence at lunar cycles (14.8 and 29.5 days) over some periods, although more sporadic than the significant powers at tidal periods.

The phase plot (Figure 1.6) showed that the lead-lag behavior of the Eh and subsurface water level signals was not consistent throughout the studied period. The colors (blue) highlight when the two signals are in phase. We observed that Eh and water levels were in phase during lunar cycles and sporadically at tidal frequencies (shown by a phase of 0 radians, Figure 1.6). During other periods, we observed that the signals were anti-phase (shown by phases of -3 and +3 radians, Figure 1.6) at tidal periods. The arrows indicate that the subsurface water level leads Eh at lunar cycles and only at times

for tidal periods. Nevertheless, the wavelet coherence showed a direct relationship between these two variables at tidal frequencies (12h and 24h), suggesting a relative change in the Eh time series across tidal cycles.

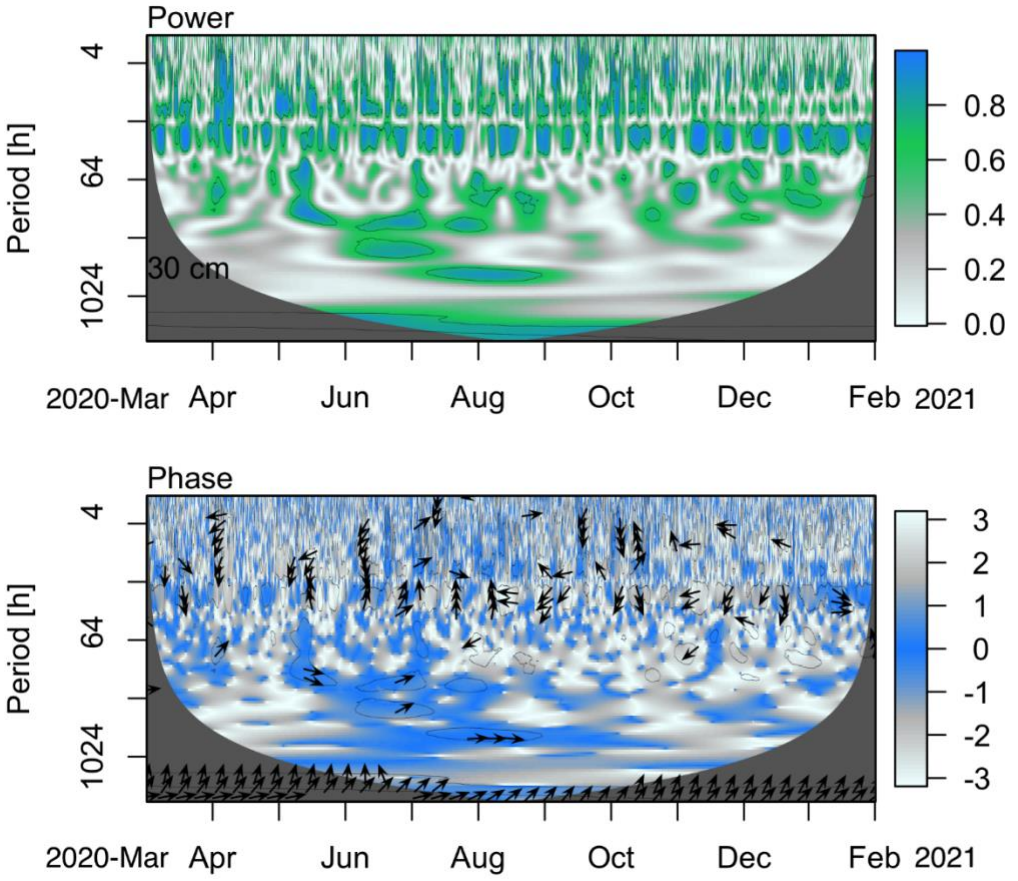

Figure 1.6 Cross wavelet analysis of subsurface water level and Eh signals at the 30 cm depth in the lower marsh position. The figure shows the modulus (power) and phase (angle in radians) of the wavelet cross-spectrum in the top and bottom panels, respectively. The power plot indicates higher coherences with blue and green colors while low coherence is illustrated by gray colors. In the phase shift, the 0-radian value indicates that the two time series are in phase while +3 radians and -3 radians indicate anti-phase (Note that the color scale actually goes from $-\pi$ to $+\pi$). Arrows pointing towards the right indicate that the time series are in phase, arrows pointing to the left indicate that the two time series are anti-phase, arrows pointing downward explain that the subsurface water level is leading, and arrows pointing upward indicate that the subsurface water level is lagging.

1.6 Discussion

1.6.1 Intertidal Processes: Implications for the Local Hydrology

Tidal signals were observed in the Eh time series across all depths, suggesting that water level fluctuations influence Eh values in the salt marsh sediment. This was confirmed by CWT analysis that showed that Eh changed at tidal frequencies (even at depth; Figure 1.3), implying that tidal surface water interacts with porewater during high tide periods, allowing for some degree of exchange in water chemistry at these frequencies (12 and 24 h).

One potential mechanism that may explain rapid water movement through the salt marsh is filling of pores during high tides and evapotranspirative loss during low tides (i.e., water removed from the salt marsh sediment via ET). However, if this were the only mechanism acting in the Eh, we would likely observe strong seasonality in Eh, highlighted during the summer growing season, when ET is higher, which we did not see (e.g., Figure 1.3). Pickleweed, the predominant plant in the salt marsh, can have a rooting depth of over 0.5 m (Meinzer, 1927)

A second potential mechanism that may explain rapid water movement through the subsurface involves animal burrows. Animal burrows are abundant in these environments (S7) and favor porewater-tidal water exchange (Tait *et al.*, 2016; Taillardat *et al.*, 2019). Tidal water circulation through burrows was the 'engine' of water and solute exchange in a mangrove-dominated marsh (Stieglitz *et al.*, 2013). Stieglitz *et al.* (2013)

used Radon and Radium isotopes to calculate water balance fluxes, determining that water flushed through animal burrows accounted for 20% of the total annual river discharge in a watershed in the Great Barrier Reef, northeastern Australia.

Our observations also agree with Breier *et al.* (2009), who used Radium isotopes to explain the subsurface hydrology in the Elkhorn Slough estuary. They suggested a relatively fast turnover between inundation and drainage of tidal zones of subsurface water, though their model could not reproduce intertidal changes. Considering that the compressibility of water is very low (Fine and Millero, 1973; Osif, 1988), and because the salt marsh is saturated most of the time, more water cannot be added to the soil without removing some water (Wong *et al.*, 2009). This condition indicates a relatively high hydraulic conductivity and relatively fast circulation of porewater through the salt marsh platform. The exchange of this more oxygenated surface tidal water with porewater would lead to tidal variations in the Eh time series, highlighting the Eh-subsurface water level relationship. This process is complex and non-linear, with Eh and subsurface water levels displaying periodic changes in their lead-lag relationship (Figure 1.6).

1.6.2 Seasonal Processes: Climatic Forcing Effects on Salt Marsh Hydrology and Biogeochemistry

The effect of precipitation in the salt marsh's subsurface water level was evident during our study. Although the tides primarily drive subsurface water level, the salt marsh drains between high and low tides (i.e., the water level is below the salt marsh surface, gray dashed line in Figure 1.5B, before the focal rain event). However, the salt

marsh platform stays saturated after precipitation events, even during low tides, possibly due to the hydrologic forcing of the elevated terrestrial groundwater level. This observation suggests that precipitation water, and the corresponding increase in the terrestrial groundwater level (Figure 1.5 B), play a role in maintaining the subsurface water level elevated in the salt marsh. This implies that high antecedent moisture conditions, interpreted as periods of higher terrestrial groundwater levels, reduce the aeration of the salt marsh platform's top centimeters, unlike periods in which the salt marsh drains. This process has important implications for carbon retention as marsh draining might enhance carbon loss from the marsh sediments due to increased carbon oxidation (Guimond *et al.*, 2020a). On the other hand, aeration of salt marsh sediments enhance pollutant removal rates as oxygenation can increase biogeochemical processes, including decomposition of excess nutrients (Nivala *et al.*, 2020).

Seasonally, the influence of different water sources (e.g., precipitation, tidal surface water) and antecedent moisture conditions on Eh varied, and the use of MLD helped detect these changes (Figure 1.5). Using the approximation component, we identified changes in the Eh behavior during precipitation events. During rainless periods, we observed the effects of tidal forcings on the Eh approximated coefficient (Figure 1.5A). However, the tidal frequency is muted during precipitation events, and the Eh signal becomes relatively flat (Figure 1.5A). We observed this phenomenon at all depths and marsh positions studied. This process shows that precipitation water, which has a different chemical signature from tidal water, exchanges with the marsh porewater relatively fast after the onset of precipitation, and this is registered in the Eh measurements (Figure 1.5A). The effect of precipitation in the Eh record might be

explained by increased lateral flow of fresh terrestrial groundwater from increased terrestrial groundwater levels during precipitation events (Figure 1.5). Although the study design does not test the specific mechanism of precipitation effects on Eh, the lateral flow of fresh groundwater across shallow subsurface marsh zones could also be driven by differences in density between fresh groundwater over saline marsh water. Additionally, direct, vertical infiltration of precipitation water into the salt marsh could be a significant factor. However, at the time scale used in this analysis (one year of hourly data), the mutual information cannot detect information that does not occur frequently, such as precipitation. More extended time series and coarser frequencies might show the effects of precipitation on Eh.

Seasonal changes in the terrestrial groundwater level and subsurface temperature variations at all marsh positions also drive subsurface Eh, as suggested by the mutual information analysis (Figure 1.4). The lateral flow of groundwater and its effect on subsurface water levels in salt marshes have been considered in the scientific literature. For example, Menció *et al.* (2017) used major ions, nutrients and water stable isotopes to study the hydrogeological dynamics of a salt marsh, also in a Mediterranean climate in Catalonia, Spain. They found that groundwater contributions to the salt marsh were significant, and played an important role in controlling water salinity. Xie *et al.* (2019) studied the importance of precipitation on salt marsh vegetation. They showed that post-dry season precipitation enhanced seedling establishment by influencing the suitability of abiotic factors for species niches. At the same time, they found that plant–soil–rainfall interactions were nonlinear and likely controlled by tidal inundation. These studies highlight the important role of fresh groundwater-saline tidal water exchanges for salt

marsh ecosystems. Our analysis shows that these interactions are present in our field site and that they influence Eh conditions in the subsurface.

Notably, the mutual information analysis showed that the terrestrial groundwater level and Eh are closely related. This relationship is likely due to similar factors affecting both signals. For example, tidal forcing, which is more evident in the Eh time series, but can impart slight variations in the terrestrial groundwater in coastal ecosystems (Turner *et al.*, 1997; Abarca *et al.*, 2013).

1.6.3 Redox conditions, drivers, and subsurface hydrology

In our study, anoxic conditions dominated the transect with subtle Eh variations across most marsh positions. The redox conditions suggest that denitrification rates in the subsurface are substrate limited, with rapid consumption of nitrate occurring when nitrate is available. Previous studies at Elkhorn Slough have found that anthropogenic nitrate inputs are removed by denitrification in salt marsh sediments (Wankel *et al.*, 2009, 2011). In systems such as Elkhorn Slough that receive high loads of anthropogenic inorganic nitrogen (Chapin *et al.*, 2004), this reinforces the idea that salt marshes are important modulators of water quality. Furthermore, despite strong variability in atmospheric forcing (e.g., precipitation), we observed relatively subtle seasonal fluctuations in Eh, suggesting that the capacity of the marsh to rapidly remove nutrients delivered from surface water is consistent throughout the year and may exert an impact on surface water quality year-round.

Sediment bulk density likely plays an essential role in controlling Eh variability in the sediment profile. Our analysis showed an overall decrease in mean Eh at each marsh position with increased soil density. However, the relationship between Eh and bulk density varied between marsh positions, perhaps due to several parameters simultaneously influencing Eh (e.g., hydrology, climate, biotic processes). The most significant ranges in Eh values were observed closest to the sediment-water interface, and also, above the higher density, less permeable layer observed at the 30 cm depths across marsh positions (Figure 1.1D). This high-density layer likely reduces vertical oxygen transport during tidal inundations (Haberer *et al.*, 2014), resulting in episodic steep vertical redox gradients (Figure 1.2).

Marsh elevation is also a likely driver of spatial variability in Eh due to difference in inundation extent across the marsh platform. Although the differences in inundation extent across the marsh positions are relatively small (S1), we found that the less inundated upper and middle marshes were less reducing overall as is evidenced by the higher average Eh values (Figure 1.2). This illustrates the importance of tidal inundation, including the duration of the inundation event, for salt marsh biogeochemistry. Specifically, tidal forcing can drive whether nitrate is removed or retained by regulating oxygen and substrate delivery to sediments (Zheng *et al.*, 2016). The elevational differences in Eh measured in our study could potentially impact marsh function by influencing the dominant microbial metabolic pathways (Falkowski *et al.*, 2008). Oxygen penetration into anoxic sediments promotes nitrification at relatively short timescales (Petersen *et al.*, 1994; Hamersley and Howes, 2005) as an electron acceptor stimulating denitrification. However, if sediments are more consistently reduced, such as at the low

marsh position, sulfide accumulation can inhibit nitrification-denitrification coupling and instead promote nitrogen retention through dissimilatory nitrate reduction to ammonium (DNRA) (Joye and Hollibaugh, 1995; Murphy *et al.*, 2020). While we did not measure biogeochemical transformations in this study, our finding that Eh differs between marsh elevations is particularly significant given that sea level rise will result in more frequent inundation of the upper marsh, potentially transforming its functionality to mirror the current lower marsh.

Overall, tidal inundation of the transect seems to be the dominant control on subsurface Eh across the salt marsh. Oscillatory tidewater and porewater interact within the marsh sediment, likely transporting oxygen and other electron acceptors to depth. Advective transport distances across tidal cycles are likely small, though this may depend on season. However, the continuing influence of oscillatory tides could heighten solute dispersion, causing a shallow vertical redox gradient that shifts somewhat over each tidal cycle (Wallace *et al.*, 2019). The corresponding oscillations in Eh vertical gradients across positions have implications for the timing of nutrient removal and fluxes to coastal environments in salt marshes. Cyclic inundation and draining of porewater due to tidal forcing (or tidal pumping) can attenuate excess nutrients and have important water quality implications.

1.7 Conclusion and Implications

Biogeochemical parameters such as nutrients are commonly measured at monthly frequencies in coastal estuaries, but significant nutrient processing can occur rapidly at much shorter time scales (e.g., precipitation events, tidal cycles). This study investigated

the variability of Eh, a critical driver of biogeochemical processes, at time scales that can explain intertidal and intra-tidal variations. Further, because Eh is linked to moisture conditions, we studied the local subsurface hydrology of a salt marsh using continuous, high-frequency water level measurements. Our work shows that the subsurface hydrology is likely dynamic with the potential for tidal surface water to exchange with subsurface water at intra-tidal time scales (12 and 24 h periods). This observation highlights the necessity to measure analytes of interest at higher frequencies to explain the critical biogeochemical processes dominating coastal ecosystems.

Moreover, our analysis shows that precipitation water mutes the tidal signal observed in the Eh time series, indicating that precipitation disturbs subsurface Eh. This result implies a relatively fast exchange of precipitation water with porewater in the salt marsh. We hypothesize that the presence of crab burrows, which are abundant in these types of environments, allows for rapid porewater-surface water exchange at sub-hourly intervals. However, temporal changes in the lead-lag relationship between Eh and subsurface water level suggest that the relationship between these parameters is not linear, and instead influenced by many interlinked processes, such as terrestrial water levels, subsurface water temperature in the salt marsh, plant activity, etc.

Continuous wavelet transforms revealed that salt marsh subsurface Eh varies significantly at frequencies corresponding to lunar cycles (14.8 and 29.5 days). During periods of higher tides, the surface water-porewater exchange seems to be accentuated. A future research question would focus on studying the biogeochemical impacts of the lunar cycles on coastal systems.

Continuous measurements of Eh at high resolution over long periods enable understanding the variability and instantaneous effects of hydrologic forcing (e.g., precipitation events, tidal flooding) in the porewater chemistry of the salt marsh platform. Furthermore, high-resolution measurements permit signal analysis in the frequency domain. By implementing techniques like those shown here in continuous Eh data sets, subsurface conditions can be further studied by analyzing specific frequencies that explain the temporal variability of a time series. For example, wavelet analysis can aid in understanding subsurface hydrologic fluctuations as it can show the effects of the tides in the subsurface or highlight the changes in the time series frequency when other water sources are present (e.g., precipitation water). Further, wavelet analysis can help understand reactive transport of Eh-sensitive solutes (e.g., nitrate), particularly in dynamic environments such as coastal estuaries.

As global climate shifts, factors including sea-level rise will induce changes in marsh position functioning and the services they provide. We used a relatively simple and robust methodology for evaluating key marsh processes. The methods presented here can assist in interpreting coastal processes, which can help with the urgency to predict future scenarios under sea-level rise conditions. Further, the application of these techniques has transformative influences on our knowledge of coupled hydrological and biogeochemical processes in marsh ecosystems.

1.6 Acknowledgement

This project was made in collaboration with Dr. Bhavna Arora. We would like to express our deepest gratitude to her for the many hours that she spent working with us

in the topic. The authors sincerely thank Dan Sampson from the University of California Santa Cruz for his valuable help programming and installing the electronic devices used in this study. We would also like to thank Andria Greene and Loren Tolley-Man for field assistance. We also thank John Haskins and the rest of the Elkhorn Slough National Estuarine Research Reserve for all their help and assistance throughout this study. EG was partially funded by a Cota-Robles fellowship through the University of California Santa Cruz, and by a Margaret A. Davidson fellowship (NA20NOS4200122). We acknowledge support from the DOE SBR NITRATES Project, funded by the U.S. Department of Energy, Office of Science, Office of Biological and Environmental Research, award number: DE-SC0021044. We acknowledge support from a California SeaGrant under California Natural Resources Agency Award Number C0303100.

Chapter 2 -Seasonality and Tidal Events Variations Drive Nitrate Dynamics in a Salt Marsh System

2.1 Abstract

Salt marshes can remove terrestrially derived nutrients *en route* to coasts. While these systems play a critical role in improving water quality that influences ecological processes, we still have a limited understanding of the spatiotemporal variability of biogeochemically reactive solutes and processes within salt marshes. We implemented a high-frequency sampling system to monitor sub-hourly nitrate (NO_3^-) concentrations in salt marsh porewater at Elkhorn Slough in coastal California, USA. We instrumented three marsh positions along an elevation gradient that resulted in different extents of tidal inundation, which we hypothesized would lead to varied biogeochemical characteristics and hydrological interactions. At each marsh position, we continuously monitored NO_3^- concentrations at depths of 10, 30, and 50 cm with subsurface water levels measured from 70 cm wells over seven deployments of ~10 days. We quantified tidal event hysteresis between NO_3^- and water level to understand how NO_3^- concentrations fluctuate across tidal cycles. Marked seasonal wet/dry periods common to Mediterranean climates caused significant NO_3^--water level hysteresis changes. In dry periods, hysteresis was generally clockwise, indicating a limited, proximal NO_3^- source that is not replenished over the event, the contribution of a dilute, distal source later in the tidal cycle, or nitrate consumption over the tidal event. This contrasts with wet periods hysteresis, where generally counterclockwise hysteresis suggests water

contributions with higher NO_3^- concentrations from potentially distal sources or in situ nitrogen processing. These findings suggest that multi-scale hydrologic control NO_3^- dynamics may influence ecological processes in coastal environments.

2.2 Introduction

Salt marsh systems act as buffers at the terrestrial-marine interface, whereby terrestrially derived nutrients may be retained or processed in salt marshes, potentially reducing the impacts of these pollutants on coastal environments (Reading *et al.*, 2017; Kumar *et al.*, 2019). These processes are critical as excess nutrients, especially nitrate (NO_3^-), discharged to coastal estuaries can drive eutrophication and hypoxia (Peterson *et al.*, 2016), which may worsen with expected shifts in climatic patterns (Sinha *et al.*, 2017). Despite the importance of the biogeochemical reactivity of salt marshes, we have a limited understanding of the spatiotemporal variability of critical biogeochemically reactive solutes and processes. Specifically, there is a knowledge gap in the short-term dynamics of NO_3^- in subsurface water at timescales over which NO_3^- can be transported, retained, and removed.

Hydrology, including the bidirectional water inputs from both land and sea into the marsh, such as tidal water, subsurface water, and terrestrial groundwater, is a potential driver of nutrient delivery and cycling in salt marsh porewater (Krause *et al.*, 2020). For example, water fluxes across the sediment-water interface control the exchange of nutrients, such as NO_3^-, from diffusive fluxes from tidally driven surface water into salt marsh porewater (Santos *et al.*, 2012; Wang *et al.*, 2022). However, the NO_3^- concentrations in salt marsh porewater at intra-tidal timescales and their

relationship with subsurface water levels are not entirely understood (Caetano *et al.*, 2012). Available datasets of NO_3^- and other biogeochemical parameters in salt marshes are usually limited to short-term synoptic sampling campaigns or infrequent long-term sampling, often with limited spatial resolution. Therefore, we have historically understudied short-term and fine-scale porewater NO_3^- dynamics over more than a few tidal cycles in these ecosystems. For example, impacts of short-lived, episodic events such as storms and tidal inundation can drive biogeochemical parameters (Grande *et al.*, 2022) but may be missed by coarse resolution sampling.

Quantifying the dynamic relationship between tidal inundation and NO_3^- in salt marshes can improve our understanding of dominant NO_3^- transport pathways, as well as biogeochemical sources and retention processes. This relationship has been studied through synoptic sampling of tidal events and analyzing the variations of NO_3^- and water level with time (Caetano *et al.*, 2012; Wang *et al.*, 2022). Previous work has found that the biogeochemical behavior of salt marshes can change as a function of tidal inundation, with shifts between retaining and producing NO_3^- during low neap and spring tides, respectively (Caetano *et al.*, 2012). However, these inferences have been based on a limited number of tidal events and in a single season. Thus, we lack understanding of whether and how salt marshes transition between being a NO_3^- source and a NO_3^- sink. In riverine environments, solute concentration-discharge (i.e., c-Q) relationships have been observed to have hysteretic behavior and have been used to infer changing solute sources and transport processes (Chanat *et al.*, 2002; Arora *et al.*, 2020). Hysteresis occurs when the c-Q relationship is different on the rising limb of a storm hydrograph versus the falling limb (Chanat *et al.*, 2002; Aguilera and Melack, 2018). A clockwise relationship

(NO_3^- concentrations are lower on the falling limb versus the rising limb) is thought to be the result of a limited NO_3^- supply close to the measurement location (Zuecco *et al.*, 2016). A counterclockwise hysteresis pattern occurs when the NO_3^- concentrations are higher on the falling limb versus the rising limb. This nonlinear relationship may be observed when the NO_3^- sources have a longer transport time (Bieroza and Heathwaite, 2015). For this study, we propose to apply this analysis approach commonly used in riverine systems to better understand NO_3^- dynamics in a salt marsh. When applied to a salt marsh, hysteresis may occur when the NO_3^--water level relationship differs on the rising limb of the high tide versus the falling limb as the tide retreats.

We propose that hysteresis relationships can indicate the general sources and sinks of NO_3^- during tidal events, for example, if NO_3^- is tidally sourced or if it is produced or consumed in the salt marsh. Several processes can increase or decrease NO_3^- concentrations in salt marshes over tidal cycles. Notably, salt marshes can produce NO_3^- via nitrification, the biological oxidation of ammonia (NH_3) or ammonium (NH_4^+) to NO_3^- (Devol, 2015). In coastal estuaries, surface NH_4^+ concentration can be elevated, favoring nitrification (Hicks *et al.*, 2019). Further, processes such as denitrification, the reduction of NO_3^- to gaseous forms of nitrogen under anoxic conditions (Almaraz *et al.*, 2020), which is common in salt marsh systems (Addy *et al.*, 2005), can result in a decrease in NO_3^- concentrations in salt marsh porewater over tidal cycles. The NO_3^--water level relationships could serve as a valuable tool to improve understanding of transport and processing dynamics in coastal areas. We hypothesize that in shallow subsurface water within the salt marsh, a clockwise loop indicates that the incoming tide is likely a source

of NO_3^-. That is, as the tide floods the transect, we would observe higher pore water NO_3^- concentrations in the rising versus the falling limb. Conversely, a counterclockwise loop with higher concentrations on the falling limb may indicate that the salt marsh could be a source of NO_3^- during ebbing tides or low tidal periods.

In situ water quality sensors have given us access to high-frequency measurements in many environmental systems. However, their cost prohibits the installation of many needed to obtain high-resolution also in space. (Birgand *et al.*, 2016)) have provided a solution by creating a multiplexed pumping system (MUX, MultiplexÔ llc) which sequentially pumps water from up to 12 sources to one high-frequency sensor. Coupled with a field-deployable spectrophotometer, they have shown that it is possible to obtain high-frequency measurements of NO_3^- across space or on a replicated manner for lab experiments (Birgand *et al.*, 2016). In particular, they used this tool to show that velocity of water flowing over wetland sediment has a major impact on sediment denitrification, likely because of enhanced exchange between the two (Birgand *et al.*, 2016). This setup was applied for subsurface sampling in an agricultural drained soil, coupling a spectro::lyser (S::CAN) to the MUX (MultiplexÔ, llc) from a network of shallow groundwater wells to evaluate the spatiotemporal variability of nitrate at sub-hourly timescales for three depths and three distances to the drain (Liu *et al.*, 2020). These techniques offer exciting opportunities for understanding NO_3^- dynamics in salt marshes, where intertidal variations could cause relatively rapid changes in marsh porewater biogeochemistry (Grande *et al.*, 2022).

To advance our understanding of nutrient dynamics in salt marshes, we implemented the novel MUX system coupled with a field-based spectrophotometer to monitor sub-hourly porewater NO_3^- concentration at multiple points and depths of a marsh soil (Birgand *et al.*, 2016). Specifically, we used the high spatiotemporal resolution nitrate data to study multi-scale hydrologic controls on marsh porewater NO_3^- concentration by exploring (1) how tidal dynamics impact short-term variations in porewater NO_3^-; (2) how seasonality (i.e., wet versus dry seasons) modulates the impact of tidal cycles on NO_3^- dynamics; and (3) how NO_3^- potential sources and transport processes drive NO_3^- in salt marsh subsurface water.

2.3 Study Area and Measurements

2.3.1 Study Site Description

This study was conducted at Elkhorn Slough in Monterey Bay, California (Figure 2.2.1A), which is part of the National Estuarine Research Reserve System (NERR). The principal source of freshwater to Elkhorn Slough are the Old Salinas River, a perennial stream that discharges at the mouth of the slough, and Carneros Creek, an ephemeral stream that only flows during the wet winter months (Caffrey and Broenkow, 2002). Tides in the estuary are mixed semidiurnal with a mean range of 1.7 m, a spring tidal range of 2.5 m, and a neap tidal range of 0.9 m. The principal transport mechanism for water in Elkhorn Slough occurs via tidal exchange (Caffrey and Broenkow, 2002). Monterey Bay seawater (Figure 2.1A) reaches up to 6 km inland during high tides, and

over 50% of the total water volume of the slough is flushed during each tidal cycle (Malzone, 1999).

Agricultural development in the watershed around Elkhorn Slough has increased in recent decades, leading to elevated nutrient concentrations, especially nitrogen species, in surface waters (Van Dop *et al.*, 2019). The Old Salinas River and Moro-Cojo Slough drain intensely farmed areas and discharge at the southern end of Moss Landing Harbor (Caffrey *et al.*, 2002). These NO_3^--rich waters result in significant sources of NO_3^- at the mouth of Elkhorn Slough that is transported into the slough with the tides (Hicks *et al.*, 2019). The high NO_3^- concentration observed at Moss Landing Harbor (Figure 2.1A) result in rapid consumption via denitrification (Almaraz *et al.*, 2020), and photosynthetic uptake as the water mixes inside the estuary (Chapin *et al.*, 2004). Further, dissimilatory NO_3^- reduction to ammonium (DNRA), the anaerobic respiration by chemoorganoheterotroph microbes using NO_3^- as an electron acceptor for respiration and reducing NO_3^- to NH_4^+, results in elevated surface water NH_4^+ concentration in the upper sections of the Slough (Caffrey *et al.*, 2002; Jeppesen *et al.*, 2018), where the field site for the present study is located (black star in Figure 2.1A). Studies have also linked problematic surface water nutrient concentrations in Elkhorn Slough to climatic drivers, such as precipitation (Hicks *et al.*, 2019), with more significant NO_3^- and NH_4^+ concentration observed during rainy winter and spring months due to runoff from agricultural fields. Further, Elkhorn Slough has been designated as a moderately eutrophic estuary and high eutrophic expression close to the study site (Hughes *et al.*, 2011).

The average precipitation at Elkhorn Slough is 627 mm/year (based on 2001-2020 record collected by the NERR ~4.5 km from the study site), with ~ 90% of the precipitation falling between November and April as rain (Chapin *et al.*, 2004). Air temperature averages 11.1 °C in the winter and 15.4 °C in the summer (Caffrey, 2002). The Mediterranean climate results in marked wet/dry seasonal dynamics (Figure 2.2), which provide the conditions to resolve seasonal variations in climatic forcing that impact subsurface saturation and biogeochemical conditions. In this area, the wet periods occur during the dormant winter season, while the dry periods occur during the summer growing season. Pickleweed, *Salicornia pacifica*, is the dominant marsh plant (Van Dyke and Wasson, 2005), and the dominant grazer and bioturbator is the lined shore crab, *Pachygrapsus crassipes* (Beheshti *et al.*, 2022).

To explain the temporal variations in NO_3^- concentrations, we used surface water data available through the ESNERR. The ESNERR, in partnership with the National Oceanographic and Atmospheric Administration maintains a tidal gauge at the mouth of the slough (Figure 2.1A). In addition to surface water level (tidal elevation), surface water salinity, pH, dissolved oxygen, and turbidity are available.

2.3.2 Experimental Transect

For this study, we instrumented a 25 m experimental transect in an emergent tidal wetland with an elevation range of 0.24 m (Figure 2.1). We delineated the transect into upper, middle, and lower marsh positions through elevation surveys and inundation extents (Figure 2.1B). The elevations above mean sea level of the upper, middle, and lower marsh are 1.79 m, 1.65 m, and 1.55 m, respectively. These elevations are tidally

inundated 6.7%, 8.9 %, and 11.2 % of the time, respectively, based on subsurface water level data collected at the site between February 2019 and November 2021. This wetland elevation categorization coincides with previous delineations of salt marsh zones across the Elkhorn Slough estuary based on vegetation coverage and elevation (Woolfolk and Labadie, 2012), and are thus broadly representative.

Sediment bulk density varies with elevation and depth at the site. Bulk density increases from the surface to 30 cm, then from 30 to 50 cm bulk density resembles that of the surface (Figure 2.2.1C). Sediment bulk density decreased from the upper marsh to the lower marsh positions, with mean values of 0.92 g/cm^3 and 0.22 g/cm^3, respectively.

We installed and maintained a network of observation wells at each marsh position to measure subsurface water level variations (Figure 2.1C). We installed the wells to a depth of 70 cm below the surface by pushing drive-point PVC pipes directly into the ground to minimize gaps around the pipe, which could cause water movement vertically along the well's annulus. We screened the wells from 5 cm below the ground surface to the total depth. We recorded water level and temperature in these wells with Solinst pressure transducer loggers (Ontario, Canada) at 5-minute intervals. We also measured air pressure at the transect at 5-minute intervals to barometrically correct the pressure transducer measurements to allow calculation of water level. We coupled these wells with high frequency measurements of porewater NO_3^- concentration using an *in-situ* sensor system described in the next section.

We installed a deep piezometer to 3.5 m below the ground surface, with 15-cm screen at the base, in an upland location ~5 m uphill from upper marsh, which is not

tidally inundated (Figure 2.2.1B). We used the same Solinst set up to measure groundwater levels at 5-minute intervals to quantify variations and evaluate the potential for fresh subsurface water to move laterally towards the salt marsh.

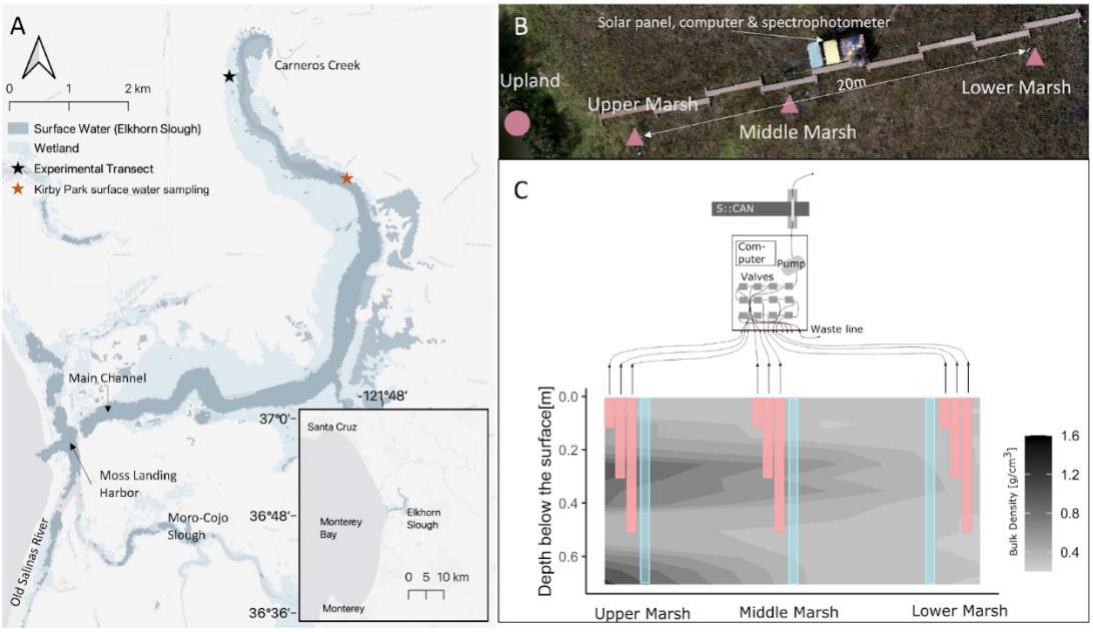

Figure 2.1 (A) Map of Elkhorn Slough with the extent of wetlands outlined in light blue. The black star marks the location of the study transect. The orange star marks the location of the Kirby Park, where the ESNERR collects monthly estuarine surface water samples that are analyzed for NO_3^- and NH_4^+ concentrations. (B) Map view of the experimental transect showing the location of the upland monitoring piezometer in relation to the salt marsh transect. (C) Illustration of the experimental transect showing the spatial distribution of the sampling cups (pink bars) and observation wells (blue bars) with a contour plot overlay of sediment bulk density across the salt marsh. The darker the colors in the contour plot, the greater the bulk density. The elevation (m amsl; not shown in the figure) of the salt marsh positions are: 1.79 m, 1.65 m, and 1.55 m for the upper, middle, and lower marsh, respectively.

2.3.3 Water Quality Measurements

To measure high frequency variations in porewater NO_3^- concentration, we coupled a multisource pump system with a field-based spectrophotometer (S::CAN Spectro::lyser ^{TM}) (Birgand *et al.*, 2016; Liu *et al.*, 2020). We connected the MUX to nine

sampling cups installed to depths of 10, 30, and 50 cm at each marsh position (Figure 2.1C). We designed the sampling cups to be similar to those described in Liu *et al.*, (2020a). The sampling cups are a "closed" chamber with an approximate volume of 150 mL (volume varied considering the depth of the sampling cup), which held enough water to rinse the optical path and allow sufficient water for an accurate measurement (Birgand *et al.*, 2016). For each cup, we used a 6-8 cm length of 5 cm internal diameter (I.D.) screened PVC pipe capped at the bottom end with a PVC cap and an epoxy resin plug at its top end. We installed tubing (0.5 cm I.D.) from the bottom of the sampling cup through the sealed epoxy layer to connect the sampling cup to the MUX. We installed 51 micron in-line filters at the connection of the tubing with the MUX to reduce large particles from clogging the system, and reduce fouling potential in the MUX and the optical probe. For the sampling cups, we used an additional vent of equal internal diameter to prevent a vacuum forming during pumping, provide hydrostatic equilibrium with the surrounding water Table 2.in the cup, and provide an escape for air as water entered the cup. When installed, we placed washed sand around the sampling cups to avoid flow restriction towards the cups. Given the low permeability of the native sediment, we placed compacted native sediment above the sand layer to avoid sampling water from above the sampling cup depth.

The MUX pumped porewater from the sampling cups to a 4 mL quartz flow-through cuvette with a 10 mm pathlength (Starna-cell®, model 46-Q-10) attached to the optical probe (Figure 2.1C). We set the temporal resolution of NO_3^- concentration measurements to ~50 minutes for each measuring cycle. In each measuring cycle, we measured the empty cuvette (e.g., took an air absorbance measurement of the empty

cuvette) to monitor any potential optic fouling of the cuvette over time (Etheridge *et al.*, 2014). We also flushed the cuvette with deionized water to remove chemical fouling once per measuring cycle. Lastly, we pumped and purged a cleaning solution (12 mg/L oxalic acid) to minimize the cuvette's chemical fouling during each sampling event. The MUX has logging capabilities and we stored the time stamp, the corresponding valve number, and 216 absorbance measurement values for each optical probe measurement (200 nm to 737.5 nm, 2.5 nm resolution).

We deployed the optical sensor coupled with the MUX in a series of ~10 day deployment periods between January and October 2021 (Figure 2.2). Data gaps during deployments represent sampling cup or instrument malfunctions resulting in different amounts of data for some marsh positions or depths.

For this study, we also used available surface water quality data through the Elkhorn Slough National Estuarine Research Reserve (ESNERR). The most reliable, closest sampling station to the research site is Kirby Park (Figure 2.1A), where monthly surface water NO_3^- and NH_4^+ concentration data are available for the study period (January-October 2021).

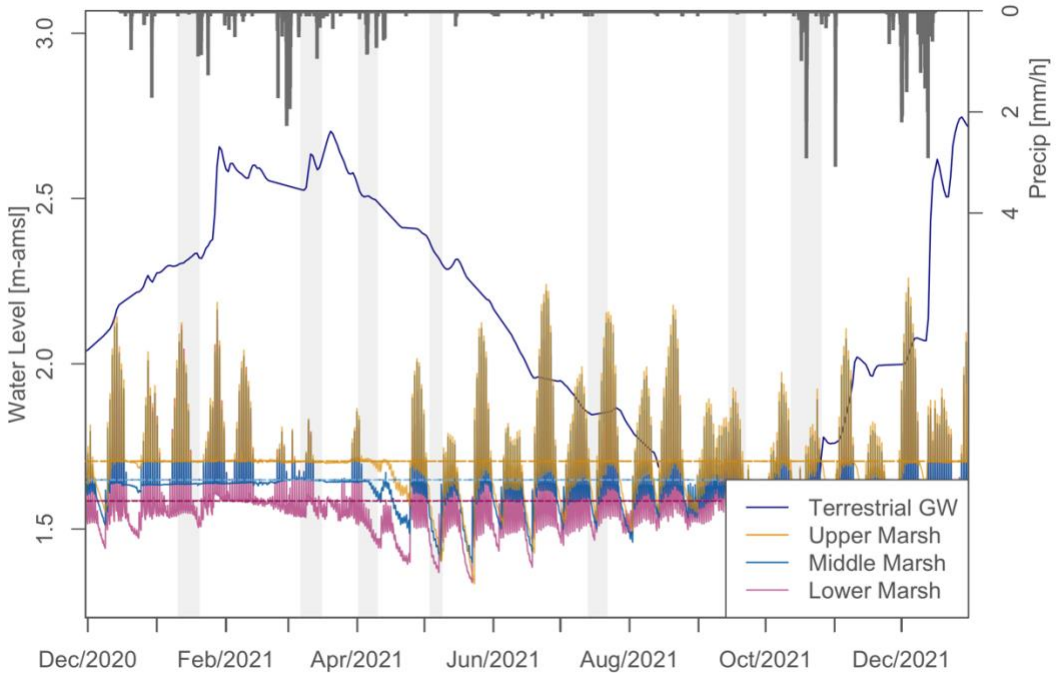

Figure 2.2 Water level time series illustrating the seasonal variations of the terrestrial groundwater level (dark blue) as measured from the upland study location. The Mediterranean climate of the study area, with marked seasonality in precipitation (gray hanging bars), results in a drop of 1.34 m in the terrestrial groundwater level between the rainy and the dry seasons. The figure also illustrates the subsurface water level time series in the upper (yellow), middle (light blue), and lower (pink) marsh positions. The horizontal dashed lines represent the salt marsh elevation at each marsh position (by color). Notice the inverted hyetograph for this time-period. The shaded regions mark the instrumentation deployment periods.

2.4 Methodology

2.4.1 In situ Nitrate Measurements and Data Preparation

We created and employed a site-specific calibration model to estimate NO_3^- concentrations using the spectral data from the optical probe. Across all deployment periods, we collected a total of 91 grab samples as water flowed through the cuvette

paired with the optical probe measurement. We analyzed these samples for NO_3^- concentration using a Lachat Quickchem 8500 auto-analyzer at the Marine Analytical Lab at the University of California, Santa Cruz, following the EPA 353.2 method (O'Dell, 1996). These samples comprised our calibration library, which we used in combination with the absorbance spectra from the optical probe to estimate NO_3^- using Partial Least Square Regression (PLSR; (Etheridge *et al.*, 2014), through the pls package in R (Liland *et al.*, 2021). This calibration model was then applied to the entire time series of absorbance spectra. More than 99% of the variance in laboratory measured NO_3^- concentration was explained by the sensor data. The Nash–Sutcliffe efficiency of the model was 0.88 and the root mean square error of the prediction was 0.09 mg/L. We generated NO_3^- concentration times series for each instrument deployment period using the calibration model. We filled short data gaps (<4 h) using cubic spline interpolation and produced a continuous time series to analyze tidal events.

To better capture the dimension and direction of NO_3^--subsurface water level relationship (i.e., hysteresis loops), we used a locally estimated scatterplot smoothing (LOESS) with a smoothing parameter (α) of 0.1 to smooth the nitrate concentration time series. We used a minimal α value so that the regression function conformed to the data closely.

2.4.2 Tidal Events Delineations

For each deployment period, we delineated individual tidal events, which we defined as the periods when the water level in the observation wells increased and then decreased as a function of individual tidal cycles (Figure 2.3). We only delineated tidal

events that inundated the top of the salt marsh. Thus, we did not identify any tidal event during the May deployment. Differences in elevation across the salt marsh, where higher elevation sites were inundated less frequently, resulted in different numbers of tidal events at each marsh position. Furthermore, instrument failure during some deployments resulted in differences in the number of tidal events studied for individual depths and marsh positions. We delineated 158 tidal events, including 58 at the lower marsh, 43 at the middle marsh, and 57 at the upper marsh position (Figure 2.7).

The study period included instrument deployments over the wet season (January to May 2021) and the dry season (July to October 2021). During this time, we delineated 158 tidal events, from which 65% occurred in the wet season and 35% in the dry season.

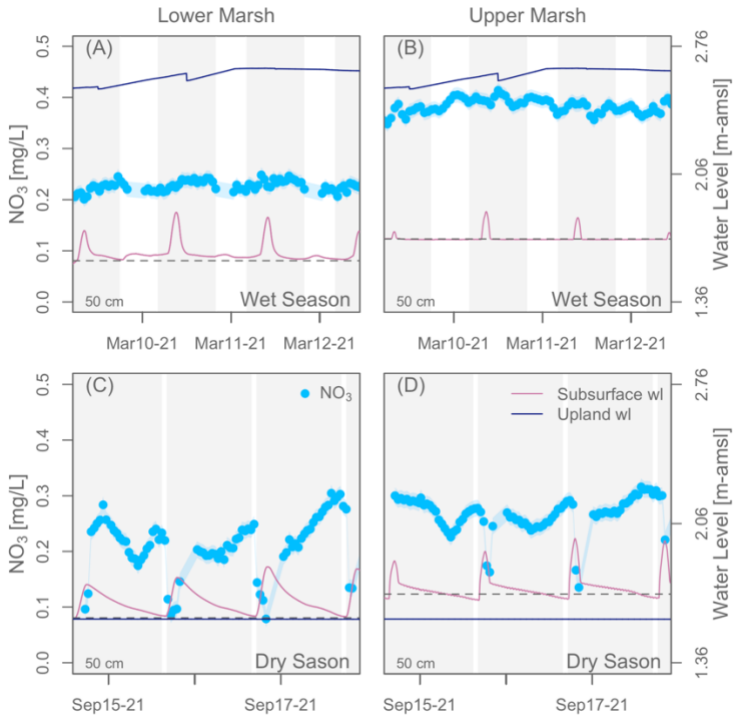

Figure 2.3 Sub-hourly NO_3^- concentrations from ~4 days during two deployment periods (March 9-12 and September 14-18 2021) from the 50 cm depth at the lower (A and C) and upper (B and D) marsh positions. The shaded regions represent the time

intervals that were delineated for individual tidal events. The horizontal dashed lines mark the elevation above mean sea level (amsl) of the salt marsh platform. The subsurface water level measured in observation wells at each marsh position is shown in pink, and captures the local tidal cycle response. The terrestrial groundwater level measured at an upland position (navy blue curve) is shown to highlight the "wetness" of the system as well as the elevation of the terrestrial groundwater with respect to the salt marsh's elevation (e.g., high during the wet season and low during the dry season). The light blue envelope on the NO_3^- time series represents the uncertainty of the measurement at 95% confidence level of a linear regression between lab-measurements and the optical probe predictions.

2.4.3 Analyses of Hysteresis Indices

We used hysteresis indices to quantify temporal porewater NO_3^- concentration-subsurface water level relationships for each tidal event across marsh positions (Lloyd *et al.*, 2016). We used the subsurface water level measured in the observation wells at individual marsh positions (Figure 2.1C). The hysteresis index has been widely used, and there is a robust description of this analysis in the literature (Andrea *et al.*, 2006; Vaughan *et al.*, 2017; Liu *et al.*, 2021). In brief, the hysteresis index (*HI*) is based on normalized water level and NO_3^- concentration as:

$$h_{i-norm} = \frac{h_i - h_{min}}{h_{max} - h_{min}} \quad (1)$$

$$C_{i-norm} = \frac{C_i - C_{min}}{C_{max} - Q_{min}} \quad (2)$$

Where h_i and C_i are the water level and NO_3^- concentration values at time step i, h_{max} and h_{min} are the maximum and minimum water levels in the tidal event, and C_{max} and C_{min} are the maximum and minimum NO_3^- concentration in the tidal event. We

normalized NO_3^- and water levels between 0 and 1 to facilitate the comparison of indices across tidal events because this ensures all events are evaluated on the same scale (Lloyd *et al.*, 2016).

Further, we calculated the hysteresis index for each water level interval (HI_j) as:

$$HI_j = C_{j-rising} - C_{j-falling} \quad (3)$$

Where $C_{j-rising}$ and $C_{j-falling}$ are calculated by estimating C_{i-norm} at 1% intervals of h_{i-norm} on the rising and falling limbs through linear regression of two adjacent values C_{i-norm} (Vaughan *et al.*, 2017; Kincaid *et al.*, 2020). We calculated the mean HI_j value for each tidal event to determine an event-specific hysteresis index (Figure 2.4). The *HI* values range between −1 and 1. Negative values indicate counterclockwise hysteresis and positive values indicate clockwise hysteresis. The magnitude of *HI* is the normalized difference between the rising and falling limbs of a flooding high tide (Figure 2.4). *HI* close to zero represents less hysteresis (i.e., *HI*'s magnitude influences the size of the loop).

We also calculated Flushing Index values for each tidal event (*FI*, Figure 2.4C). The *FI* is computed as the slope of the line between the normalized subsurface water level value at the peak tidal event (i.e., the maximum normalized subsurface water level value) and the normalized subsurface water level value at the beginning of the tidal event (Vaughan *et al.*, 2017). Values of this index range between −1 and 1 (Figure 2.4C). Negative values indicate a decrease in NO_3^- concentrations on the rising limb whereas positive values indicate an increase in NO_3^- on the rising limb. The distance from zero

indicates the magnitude of the difference in NO_3^- concentration at the start of the tidal event versus the peak of the tidal event. A positive *FI* could suggest that the salt marsh is a source of NO_3^- or that tidal water "flushes" the salt marsh subsurface with high NO_3^-, and we observe it as an increase in NO_3^- on the rising limb of the event. A negative *FI* would imply that the tidal water is a source of NO_3^-, that is consumed in the salt marsh over the tidal event, resulting in a decrease in NO_3^- from the beginning of the high tide towards the maximum water level. A negative *FI* can also result from dilution processes if the incoming tidal water dilutes the salt marsh subsurface from the beginning to the peak of the tidal event.

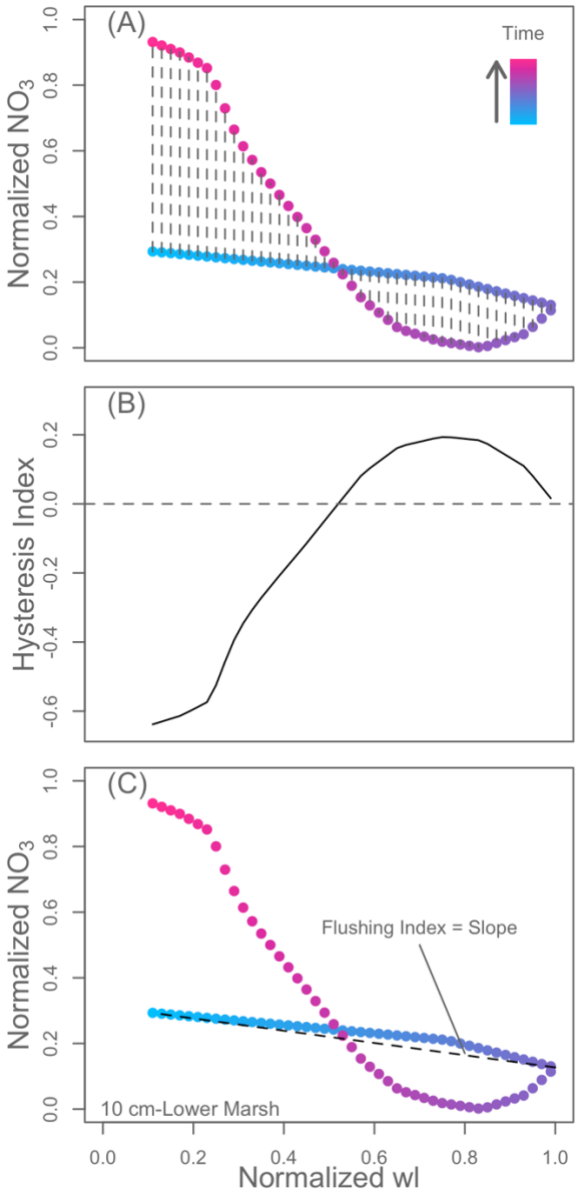

Figure 2.4 Plot of normalized NO_3^- concentrations and normalized water level (A), hysteresis index (B), and flushing index (C) for a tidal event at the lower marsh position (10 cm depth) on September 19th, 2021. We calculated hysteresis index HIj (vertical dashed lines in A) by subtracting the normalized NO_3^- on the falling limb from that of the rising limb for each 1 % of the normalized water level (as illustrated by the dotted lines on A). The event hysteresis (HI) is the mean HIj. The flushing index (FI) is the slope of the line that intersects the normalized NO_3^- concentration at the beginning and the point of peak water level for each tidal event (C). In this example HI = -0.091 and FI = -0.19.

2.4.4 Statistical Tests

We analyzed the normality of all of the data distributions using histograms, Q-Q plots, and Shapiro-Wilk tests (Shapiro and Wilk, 1965) using the "shapiro.test" function in base R (R Core Team, 2021). We tested if the variations in porewater NO_3^- concentration differed significantly among marsh positions and depths using Levene's test (Schultz, 1985). We used a significance level (α) of 0.05 for statistical significance. This test is suiTable 2.for normally and non-normally distributed data. In these analyses, we used the Brown-Forsythe variant of the test, which uses deviations from the median because our data are non-parametric (Gastwirth *et al.*, 2009). We used the "leveneTest" function from the "car" package in R (Fox and Weisberg, 2019).

We used the Kruskal-Wallis test (Breslow, 1970) to analyze if the hysteresis indices (*HI* and *FI*) are identical for the wet and dry seasons and to evaluate differences in porewater NO_3^- concentration across depth and marsh positions. The Kruskal-Wallis test is a non-parametric method that tests the null hypothesis of identical populations. We used a level (α) of 0.05 for statistical significance. We used the "kruskal.test" function in base R (R Core Team, 2021) for this analysis. All significant results were further analyzed with pairwise Mann-Whitney U test (Rosner and Grove, 1999) to correct the significance level for multiple comparisons.

2.5 Results

2.5.1 Precipitation, seasonal groundwater level and salt marsh subsurface water level fluctuations

Water year 2020 was extremely dry, with 281 mm of total precipitation, which was 346 mm below the long-term annual average for the area. Over the study period, we observed a difference of 1.34 m between the peak terrestrial groundwater level (2.75 m-amsl) in the wettest period (December 2020) and the lowest level (1.39 m-amsl) in the driest period (September 2021).

The terrestrial water level responds to precipitation events with relative increases during precipitation periods (Figure 2.2). Marsh subsurface water levels are subject to daily, biweekly, and seasonal tidal cycle inundation dynamics (due to the position of the moon/earth), resulting in multiple water level fluctuation frequencies (Grande *et al.*, 2022). Subsurface water levels at the lower marsh position are consistently lower than at the upper and middle marsh positions during low tides, draining below the marsh elevation in each tidal cycle. However, the subsurface water level in the upper and middle marshes did not drop below the marsh elevation during the wet dormant season (e.g., January to March 2021; Figure 2.2). This indicates that the marsh does not drain substantially between daily tidal cycles during this period. As the system transitioned into the dry season, we observed that the terrestrial groundwater levels decreased, and the salt marsh subsurface water levels dropped below the salt marsh surface between tidal inundation periods (e.g., April to October 2021; Figure 2.2).

2.5.2 Effect of salt marsh position and depth on porewater nitrate concentrations

NO_3^- concentration in salt marsh porewater ranged between 0 and ~1 mg/L over the study period, with a mean and a standard deviation of 0.17 mg/L and 0.12 mg/L, respectively. Overall, we found differences in NO_3^- concentrations across the different marsh positions and different depths, but these differences were complex and did not follow simple trends with marsh elevation. Temporal variations in NO_3^- concentration differed between marsh positions (Brown-Forsythe test: $F(2) = 680.41$, $p < 0.0001$; Table 2.1; Figure 2.5A), with the upper marsh position showing the greatest temporal variability (Interquartile range, IQR = 0.22 mg/L). Overall, the middle marsh had higher porewater NO_3^- concentrations (median = 0.19 mg/L) than the lower (median = 0.14 mg/L) and upper marsh positions (median = 0.14 mg/L; Kruskal-Wallis test: $H = 479.14$, $df = 2$, $p < 0.0001$; Table 2.1, Figure 2.5A).

Temporal variations in NO_3^- concentration also differed between depths (Brown-Forsythe test: $F(2) = 211.95$, $p < 0.0001$; Figure 2.5B), with the 50 cm depth showing the greatest temporal variability (IQR = 0.17 mg/L). The NO_3^- concentration at 50 cm depth were significantly higher (median = 0.19 mg/L) than at 10 cm (median = 0.15 cm) and 30 cm depths (median = 0.13 mg/L; Kruskal-Wallis test: $H = 659.33$, $df = 2$, $p < 0.0001$; Table 2.1, Figure 2.5B).

The effect of depth on NO_3^- concentration varied between individual marsh positions, with the highest concentrations occurring at different depths in each position.

At the lower marsh position, median NO_3^- concentration was highest at 30 cm depth (median = 0.157 mg/L; Kruskal-Wallis test: H= 21.21, df = 2, $p < 0.0001$), and there was no difference between the 10 cm (median = 0.134 mg/L) and 50 cm depths (median = 0.133 mg/L; Kruskal-Wallis test: H= 0.67, df = 1, p = 0.4) (Figure 2.5D). In contrast, in the middle marsh, the median NO_3^- concentration was lowest at the 50 cm depth (median = 0.15 mg/L; Kruskal-Wallis test: H= 197.17, df = 2, $p < 0.0001$). There was no difference between the 10 cm (median = 0.21 mg/L) and 30 cm depths (median = 0.23 mg/L; Kruskal-Wallis test: H= 3.17, df = 1, p = 0.075; Figure 2.5E). Finally, at the upper marsh, median NO_3^- concentrations varied between all depths, with the highest concentrations occurring at the 50 cm depth (median = 0.27 mg/L) and the lowest at the 30 cm depths (median = 0.06 mg/L; Kruskal-Wallis test: H= 1823.4, df = 2, $p < 0.0001$; Figure 2.5F).

Table 2.1 Summary statistics for the different marsh positions and depths of the experimental transect. SD is the standard deviation and IQR is the interquartile range (i.e., the range between the 25th and 75th quartiles).

Marsh Position	**Mean [mg/L]**	**Median [mg/L]**	**SD [mg/L]**	**IQR [mg/L]**
Lower	0.152	0.140	0.096	0.135
Middle	0.186	0.187	0.118	0.151
Upper	0.184	0.135	0.149	0.216
Depth [cm]				
10	0.166	0.151	0.115	0.152

30	0.152	0.130	0.112	0.153
50	0.196	0.188	0.133	0.175

2.5.2.1 Seasonal Effects in Nitrate Concentrations

Although the effect of marsh position and depth on NO_3^- concentrations was complex, we found clearer and more consistent differences in porewater NO_3^- concentrations between wet and dry periods. There were higher NO_3^- concentrations during wet periods (median = 0.21 mg/L) than during dry periods (median = 0.10 mg/L; Kruskal-Wallis test: H = 1328.5, df = 1, $p < 0.0001$) across all marsh positions and depths (Figure 2.5G-H). We also found an effect of wet/dry seasons on porewater NO_3^- concentrations among depths across the salt marsh, with higher NO_3^- concentration in the wet season (Table 2.2).

Table 2.2 Summary statistics of seasonal salt marsh porewater NO_3^- concentrations. Wet season NO_3^- concentrations are significantly higher in all the marsh positions and depths of this study. All tests in the Table 2.have 1 degree of freedom and p-value < 0.0001.

Marsh Position	**Median dry season NO_3 [mg/L]**	**Median wet season NO_3 [mg/L]**	**Kruskal-Wallis test: H**
Lower	0.08	0.19	507.6
Middle	0.11	0.24	499.4
Upper	0.10	0.17	104.4

Depth [cm]			
10	0.11	0.20	144.5
30	0.10	0.18	183.7
50	0.09	0.24	1198.6

However, the effect of wet/dry season on depth varied between individual marsh positions. At the lower and middle marsh positions, NO_3^- concentrations were higher at all depths during the wet season (Table 2.3). In contrast, at the upper marsh position, NO_3^- concentrations were lower at the 10 cm and 30 cm depths during the wet season relative to the dry season. At the 50 cm depth, NO_3^- concentrations were higher during the wet season relative to the dry season (Table 2.3).

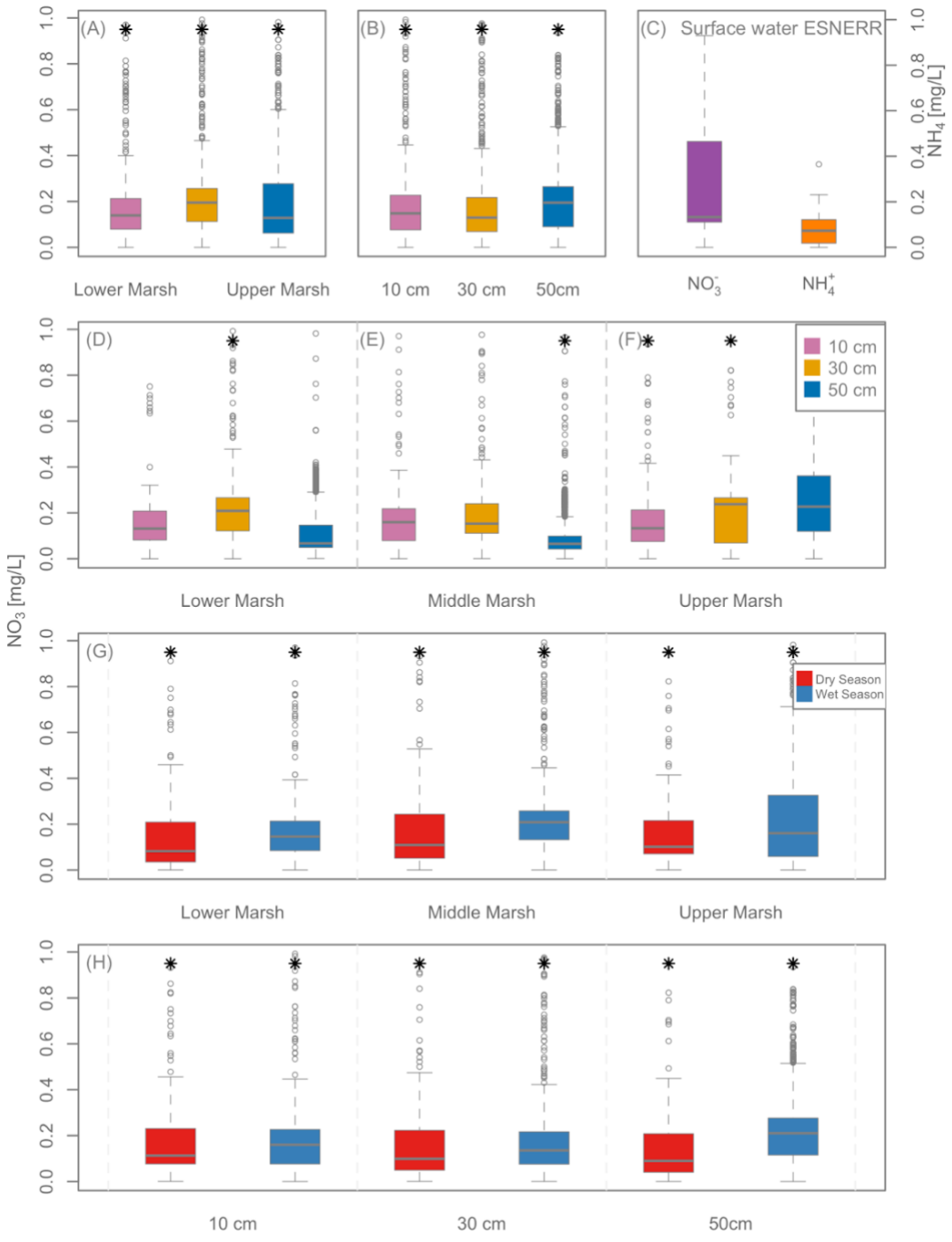

Figure 2.5 (A) NO_3^- concentrations across the three marsh positions considering all depths. (B) Marsh porewater NO3- concentration at 10, 30, and 50 cm depths for all marsh positions. (C) Plot of NO3- and NH4+ concentrations from surface water in the ESNERR for the 2021 calendar year. (D), (E), and (F) NO3- concentrations across depths for each marsh position. (G) NO3- concentration across the three marsh

positions separated by dry (red) and wet seasons (blue). (H) NO3- concentration across the three depths separated by dry (red) and wet seasons (blue). One sample in (C) exceeded the 1 mg/L limit of the y axis with a concentration of 2.9 mg/L and was collected in February 2021. Asterisks on top of the plot designate significant differences (p-value < 0.05). All plot ordinates are on the same scale.

2.5.3 Nitrate and Ammonium in Estuarine Surface Water

During the study period, January 2021 to November 2021, surface water NO_3^- concentrations varied between 0 mg/L in summer (August 2021) and 2.9 mg/L in the winter (February 2021). Over the study, surface water NO_3^- had a mean, a median, a standard deviation, and an interquartile range (IQR) of 0.5 mg/L, 0.83 mg/L, 0.13 mg/L, and 0.35 mg/L, respectively (Figure 2.5C).

During our study, surface water NH_4^+ concentrations varied between 0 mg/L in summer (August 2021) and 0.36 mg/L in the winter (February 2021). Over the study period, surface water NH_4^+ had a mean, a median, a standard deviation, and an IQR of 0.1 mg/L, 0.07 mg/L, 0.11 mg/L, and 0.1 mg/L, respectively (Figure 2.5C).

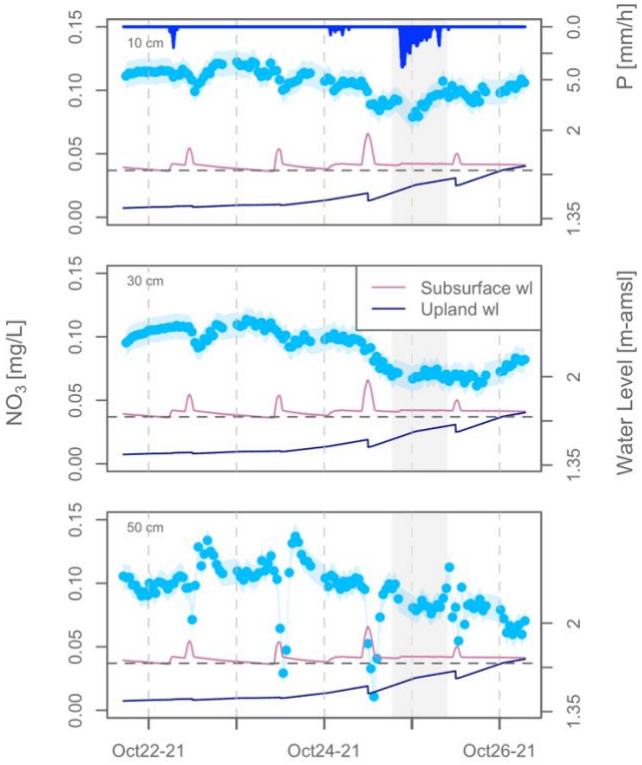

Figure 2.6 Upper marsh porewaterNO_3^- time series during part of the October 2021 deployment for 10 cm (A), 30 cm (B), and 50 cm (C) depths. The shaded region highlights a focal precipitation event observed during this period (notice the inverted hyetograph on top), which disturbed the tidal effect in the NO_3^- time series. The pink line is the subsurface water level, and the dark blue is the terrestrial groundwater level. The figure illustrates how minima in NO_3^- lag the high tides at the 10 cm and 30 cm depths, and a gradual increase in NO_3^- concentrations in the low tide. However, we observe a much faster increase in NO_3^- concentration following the high tide at the 50 cm depth. The horizontal dashed line marks the elevation of the salt marsh at this position (1.7 m-amsl).

2.5.4 Hysteresis Index

Tidal event *HI* values were influenced by season (Figure 2.7 C; Kruskal-Wallis test: H= 31.43, df = 1, $p < 0.0001$) rather than marsh position (Kruskal-Wallis test: H= 2.328, df = 2, p = 0.3) or depth (Kruskal-Wallis test: H= 3.74, df = 2, p = 0.15). Median *HI* was predominantly negative (counterclockwise) during the wet season (median = -

0.13), contrasting with a predominantly positive *HI* during the dry season (median = 0.15; clockwise). However, this seasonal effect did not persist across all marsh positions and depths.

Table 2.3 Summary statistics of seasonal effects on NO_3^- concentrations by depth in each marsh position. All tests in the Table 2.have 1 degree of freedom and p-value < 0.0001.

Marsh Position	Depth [cm]	Median dry season NO_3 [mg/L]	Median wet season NO_3 [mg/L]	Kruskal-Wallis test: H
Lower	10	0.13	0.19	83.1
Lower	30	0.09	0.19	110.4
Lower	50	0.04	0.20	339.4
Middle	10	0.12	0.24	184.0
Middle	30	0.12	0.22	155.4
Middle	50	0.07	0.25	144.4
Upper	10	0.11	0.06	158.5
Upper	30	0.10	0.05	470.1
Upper	50	0.10	0.34	144.4

The effect of seasonality on hysteresis patterns was evident across depths in the upper marsh position, with significant differences between wet and dry periods at all depths (Table 2.4). Predominantly positive *HI* in the dry season contrasted with predominantly negative *HI* in the wet season. There was no effect of season at any depth in the middle marsh position (Table 2.4), but in the lower marsh, *HI* was negative during the wet season and positive during the dry season for the 10 cm and 50 am depths with significant differences among wet and dry periods (Table 2.4). Conversely, the *HI* in the 30 cm depth of the lower marsh was not significantly different among the dry and wet seasons (Table 2.4).

Table 2.4 Summary statistics of seasonal effects on hysteresis index (HI) and flushing index (FI) by depth in each marsh position. Significant differences in wet/dry seasons are marked by bolded p-values in the table. All tests in the Table 2.have 1 degree of freedom.

Marsh Position	**Depth [cm]**	**median dry season *HI***	**median wet season *HI***	**Kruskal-Wallis test: H**	**p-value**
Lower	10	0.14	-0.03	6.4	**0.01**
Lower	30	0.36	0.16	0.5	0.5
Lower	50	0.06	-0.2	4.4	**0.04**
Middle	10	0.16	0.37	3.8	0.05
Middle	30	0.06	-0.16	2.7	0.1
Middle	50	0.10	0.27	1.4	0.2

Upper	10	0.21	-0.28	10.8	**0.001**
Upper	30	0.18	0.01	7.4	**0.006**
Upper	50	0.13	-0.06	4.5	**0.03**
		median dry season *FI*	**median wet season *FI***	**Kruskal-Wallis test: H**	**p-value**
Lower	10	-0.17	0.04	6.4	0.07
Lower	30	-0.22	-0.13	0.1	0.7
Lower	50	-0.21	0.46	4.9	**0.03**
Middle	10	-0.19	-0.74	6.2	**0.01**
Middle	30	-0.04	0.37	3.3	0.07
Middle	50	-0.17	-0.42	0.4	0.5
Upper	10	-0.22	-0.26	13.0	**0.001**
Upper	30	-0.19	0.06	9.0	**0.003**
Upper	50	-0.18	0.33	9.3	**0.002**

Dispersion in *HI* differed significantly between wet and dry periods for the middle marsh (Brown-Forsythe test: $F(1) = 6.5$, $p = 0.015$) with the wet season displaying a larger scattering than the dry season (Figure 2.7). We did not find significant

differences in the scattering between wet and dry seasons for the upper (Brown-Forsythe test: $F(1) = 0.1$, $p = 0.7$) or lower marsh positions (Brown-Forsythe test: $F(1) = 1$, $p = 0.3$). Furthermore, we did not find any clear evidence that precipitation or tidal cycle influenced the scattering of the data. In addition, we did not find any relationship between *HI* and available data through the ESNERR for estuarine water salinity, pH, dissolved oxygen, temperature, or turbidity that could explain the larger scattering in the wet season.

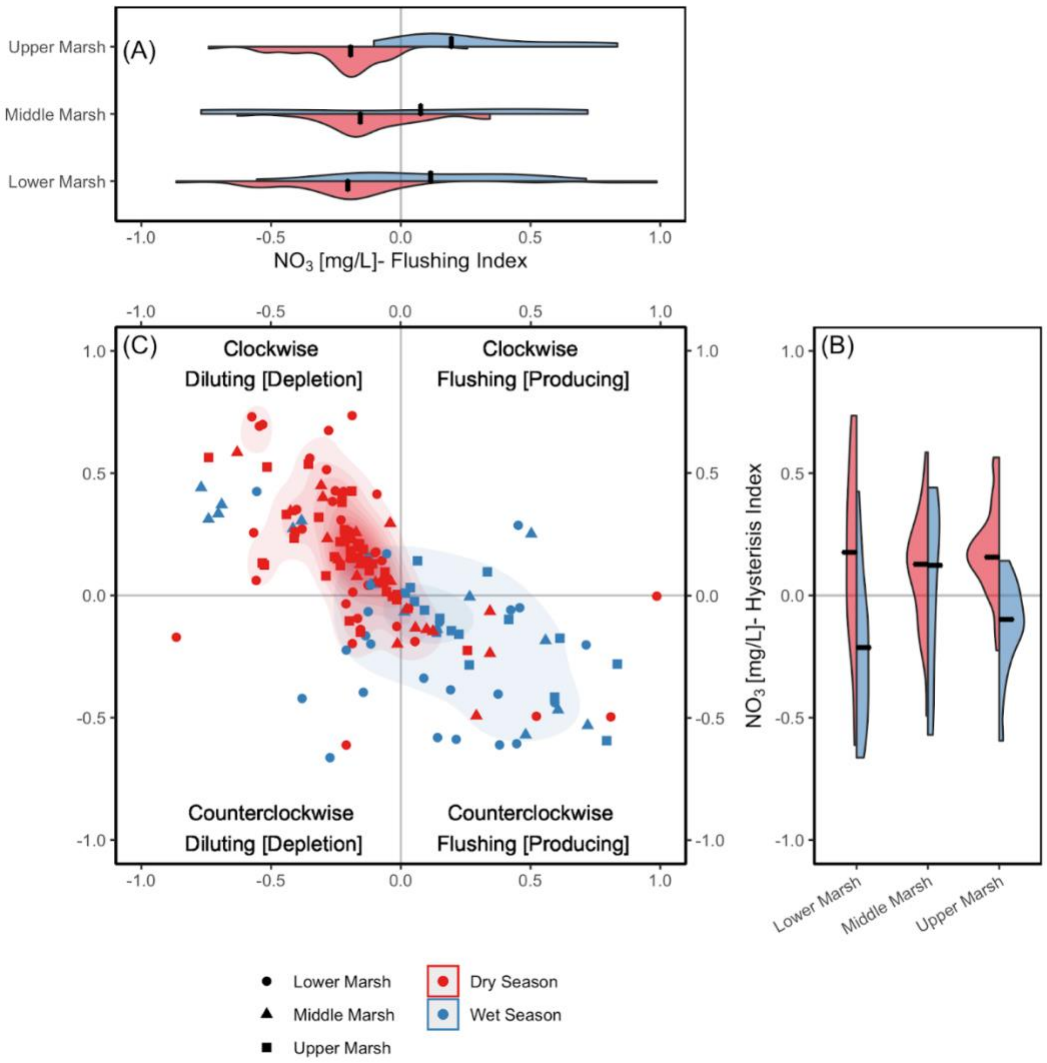

Figure 2.7 Split violin plots of the (A) tidal event flushing index and (B) hysteresis index for the lower, middle, and upper marsh positions, separated by dry (red) and wet (blue) seasons. The split violin plots show the distribution of hysteresis index values across all tidal events. The black line in each violin plot marks the median of the distribution. (C) The hysteresis index versus flushing index for the 158 tidal events for the lower (circles; 58 events), middle (triangles; 43 events), and upper marsh (squares; 57 events) positions. Separating the hysteresis indices by dry (red) and wet (blue) seasons results in significant differences between these metrics.

2.5.4.2 Flushing Index

Like *HI*, *FI* was strongly affected by wet/dry seasonality. *FI* was predominantly positive during the wet season (median *FI* = 0.14) and predominantly negative during the dry season (median *FI*= -0.19; Kruskal-Wallis test: H= 29.4, df = 1, $p < 0.0001$; Figure 2.7A). The median *FI* was negative for the three marsh positions, with median *FI* values of -0.13, -0.15, and -0.14 for the lower, middle, and upper marsh positions, respectively, and there were no significant differences among the marsh positions (Kruskal-Wallis test: H= 0.007, df = 2, p = 1). Similarly, we did not find significant differences between the 10, 30, and 50 cm depths, with median *FI* values of -0.13, -0.11, and -0.16, respectively (Kruskal-Wallis test: H= 1.02, df = 2, p = 0.6).

The effect of seasonality on *FI* was evident in individual salt marsh positions. In the lower marsh, predominantly negative *FI*s during the dry season (median = -0.20) contrast with positive *FI*s during the wet season (median = 0.11; Kruskal-Wallis test: H= 10.68, df = 1, p = 0.001). However, in the middle marsh, we did not find significant differences between the dry (median *FI* = -0.16) and wet seasons (median *FI* = 0.08; Kruskal-Wallis test: H= 0.27, df = 1, p = 0.6). In the upper marsh, we found significant differences in *FI* between dry (median *FI* = -0.19) and wet periods (median *FI* = 0.19; Kruskal-Wallis test: H= 31.74, df = 1, $p < 0.0001$). Further, seasonality resulted in predominantly negative *FI* in dry periods and positive *FI* in wet periods for each depth across the salt marsh.

The wet/dry seasonality effect on *FI* patterns was evident across depth for each individual marsh position (Table 2.4). In the upper marsh position, wet and dry season *FI*s were significant at all (Table 2.4). In the middle marsh, the effect of seasonality was significant between wet and dry periods for the 10 cm, but not for the 30 or 50 cm

depths (Table 2.4). The lower marsh position had significant differences between wet and dry periods for the 50 cm depth, but not for the 10 or 30 cm depths (Table 2.4).

Dispersion in *FI* differed significantly between wet and dry periods for the middle (Brown-Forsythe test: $F(1) = 29.4$, $p < 0.001$) and upper marsh positions (Brown-Forsythe test: $F(1) = 4.5$, $p < 0.05$) with the wet season displaying a larger scattering than the dry season (Figure 2.7). We did not find significant scattering for the lower marsh (Brown-Forsythe test: $F(1) = 0.76$, $p = 0.4$). Moreover, we did not find any clear evidence that precipitation or tidal cycle influenced the scattering of the data. In addition, we did not find any relationship between *FI* and available data through the ESNERR for estuarine water salinity, pH, dissolved oxygen, temperature, or turbidity that could explain the larger scattering in the wet season.

2.6 Discussion

We combined high-frequency NO_3^- concentration and water level time series to calculate NO_3^--subsurface water level hysteresis indices to evaluate the effects of tidal forcings on marsh porewater biogeochemistry over short (diel) timescales, and ultimately understand how precipitation seasonality modulates these short-term relationships. This hysteresis index approach has been widely used in riverine systems (i.e., c-Q plots; (Aguilera and Melack, 2018)), but we adapted it to a coastal setting to provide new insight into how seasonality modulates the role of tidal events in driving porewater NO_3^- dynamics along a salt marsh tidal inundation gradient. We explored how these hydrologic drivers interact to produce seasonal patterns in subsurface chemistry that might influence nutrient export to coastal waters. This analysis can help us understand the potential

impacts of climate change, especially predicted extreme changes in precipitation patterns in the western United States (Swain *et al.*, 2018), that might lead to significant shifts in the porewater NO_3^- concentration dynamics and marsh source/sink status.

2.6.1 Seasonal shifts in hysteresis indices

Multi-scale temporal (intra-tidal and seasonal) hydrologic fluxes drive salt marsh porewater NO_3^- dynamics. While diel tidal forcings dominate NO_3^- fluctuations over short periods (Figure 2.6), the seasonal wet/dry regimes control shifts in the directionality of hysteresis between nitrate and subsurface water level. Observed *HI* and *FI* values had opposite signs as a function of season (Figure 2.7). During the dry season, most tidal events had positive *HI* (clockwise) and negative *FI* (depletion, Figure 2.7). During the wet season, we observed negative *HI* (counterclockwise) and positive *FI* (production; NO_3^- Figure 2.7).

For the wet season, the hysteresis results imply limited transport of proximal NO_3^- sources early in the tidal event cycle, followed by enrichment from distal and NO_3^--rich sources or in situ production of NO_3^-. In the present study, we observed that the porewater NO_3^- concentration increased after the peak of the tidal event during the wet season. This could result from the oxidation (nitrification) of NH_4^+ stored in the pores, and/or from a rise in the groundwater Table 2.(Figure 2.2), if the groundwater has elevated NO_3^-. In watershed hydrology, where these indices were developed, negative *HI*s and positive *FI*s have been described in golf courses and agricultural areas and were attributed to a rising water Table 2.during precipitation events, mobilizing NO_3^- from

fertilizer applications stored in upper soil horizons (Oeurng *et al.*, 2010; Aguilera and Melack, 2018; Grande *et al.*, 2019). Our data suggests that similar mechanisms may be mobilizing nitrate in coastal wetlands.

The negative hysteresis index values in the wet season suggest that the NO_3^- source, which we hypothesize is dominated by tidally driven estuarine surface water, is progressively removed (i.e., depleted) as it exchanges with the marsh platform (Figure 2.8). This finding aligns with previous work showing that salt marsh systems can remove NO_3^-, thereby reducing the impacts of excess nutrients on nearshore waters (Hamersley and Howes, 2005; Bulseco *et al.*, 2019; Bowen *et al.*, 2020). Further, previous work in salt marshes has highlighted that NO_3^- is imported from estuarine surface water into marsh porewater during spring and neap tides (Wang *et al.*, 2022).

While different marsh positions experience different inundation extents, the predominant hysteresis index values indicate that all marsh positions share a similar NO_3^--subsurface water level relationship. Overall, tidally driven Elkhorn Slough surface water was the dominant nutrient source to the subsurface (Figure 2.8). This finding is remarkable, considering that different marsh positions have distinct hydrologic pathways and differing influences of terrestrial groundwater inputs (Robinson *et al.*, 2018). We hypothesized that NO_3^- sources could range from mostly estuarine surface water in the lower marsh to a mix of tidally driven estuarine surface water, terrestrial groundwater, and surface runoff in the upper marsh.

Although the hysteresis indices were not significantly different between marsh positions, we observed differences in the importance of the wet versus dry season in

explaining hysteresis indices across different depths. The results for the upper and lower marsh are consistent with the general patterns observed across the salt marsh as a result of seasonality (Figure 2.7C). In the middle marsh, seasonal patterns did not differ in hysteresis indices among depths. The hysteresis indices in the middle marsh had a large variability across the range of *HI* and *FI* (Figure 2.7C), with little apparent differences in hysteresis in this marsh position when comparing depths and seasons (Table 2.4).

Variability in the hysteresis and flushing indices was more pronounced in wet periods than in dry periods (Figure 2.7). However, we did not find any relationship between *HI* and *FI* and the timing of precipitation events, terrestrial water level elevation, tidal elevation, surface water temperature, surface water pH, surface water salinity or surface water turbidity. This finding suggests that the variability in *HI* and *FI* during the wet season is likely driven by other processes, such as other NO_3^- delivery mechanisms, that can be delayed in time with respect to, for example, precipitation events, and that our analysis is unable to constrain.

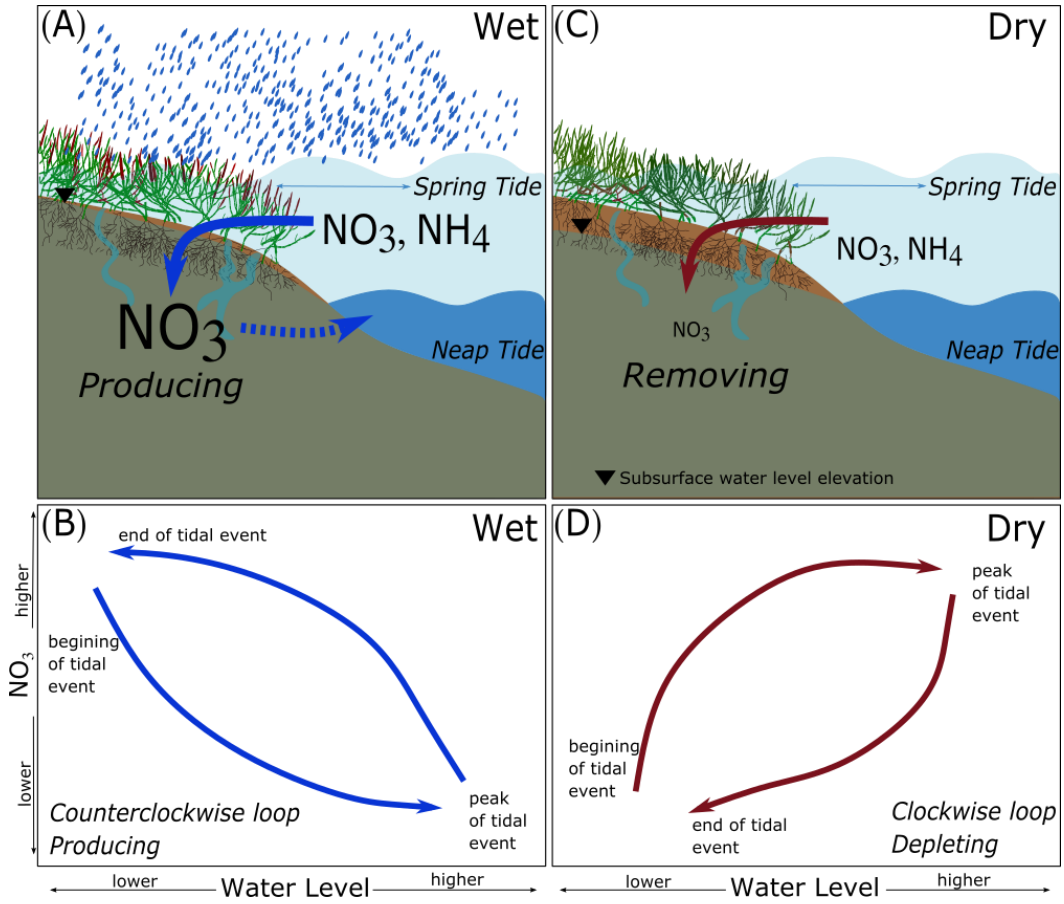

Figure 2.8 Conceptual model of multi-scale hydrologic drivers (tidal and seasonal) in the salt marsh highlighting the shifts in the biochemical behavior of the salt marsh between wet (A-B) and dry (C-D) seasons. Counterclockwise loops and producing patterns in the wet season indicate that the salt marsh is a NO_3^- source. Clockwise loops and depleting patterns in the dry season show that in this season, the salt marsh is a NO_3^- sink. Notice that surface water nutrient concentrations (NO_3^-, NH_4^+) are higher during the wet season.

2.6.2 Seasonal effects on porewater nitrate dynamics

Porewater NO_3^- concentrations were predominantly higher during the wet season across depths and marsh positions (Figures 3 and 5D-E). As a result of agricultural runoff into the estuary, significantly higher NO_3^- concentrations are common in surface water during the wet season (Van Dop *et al.*, 2019) and can be an important

source of NO_3^- to salt marsh porewater. This contrasts with the dry season, where we observed lower porewater NO_3^- concentrations for all depths in the lower and middle marsh positions. That said, NO_3^- concentrations were higher during dry periods for the 10 and 30 cm depths in the upper marsh. We suggest that the seasonal wet/dry effect in the upper marsh could result from in situ NO_3^- production (nitrification) during dry periods. Considering that the upper marsh is inundated less frequently, and that the dry season occurs in synchrony with the growing season, there is a higher potential for soil aeration that can result in nitrification (Koop-Jakobsen and Giblin, 2010).

The amplitude of NO_3^- fluctuations at intra-tidal scales varied between seasons. During the wet season, the tidal fluctuations of the NO_3^- time series were less evident (i.e., the distinct NO_3^- peaks at tidal frequencies were damped; Figure 2.3 A-B). When the terrestrial groundwater level was below the marsh surface in the dry season, we observed a stronger tidal signal in the NO_3^- record (Figure 2.3 C-D). We expected to find the opposite pattern (more significant fluctuations in pore water NO_3^- over wet season tidal cycles) because of higher NO_3^- concentrations in wet season surface water (Van Dop *et al.*, 2019) and because NO_3^- is often limiting in marsh environments (Bledsoe *et al.*, 2020).

Precipitation events had short-term effects on observed the salt marsh porewater NO_3^- concentration (e.g., Figure 2.6). For example, in the October deployment, we found that the tidal effect appeared more muted in the NO_3^- time series during precipitation periods NO_3^-across all depths and marsh positions (shaded region in Figure 2.6), suggesting that precipitation water exchanged with salt marsh porewater

diluting the NO_3^- concentration. This result agrees with previous observations of multilevel decomposition of continuous redox potential measurements across this salt marsh transect during a precipitation event that showed how precipitation water changed redox potential at depth (Grande *et al.*, 2022). These interactions seem to occur at relatively short timescales because we see a relatively instantaneous dilution pattern during the storm event in theNO_3^- time series.

2.6.3 Intra-tidal and spatial effects on marsh nitrate concentration

While seasonality was the key driver of NO_3^- concentrations across the marsh, we observed within-marsh variation across tidal events, positions, and depths (Figures 3 and 5).Tidal events influenced porewater NO_3^- concentrations on hourly timescales across the study period, with distinct NO_3^- spikes (both positive and negative) at tidal frequencies across depths and marsh positions (e.g., Figures 3 and 6). These findings are consistent with previous measurements of high-frequency (1-minute resolution) redox potential and subsurface water level that suggested a relatively fast exchange of tidal water with porewater that influenced biogeochemical processes at intra-tidal timescales (Grande *et al.*, 2022). We observed a tidal "signature" consisting of a characteristic increase and subsequent decrease in porewater NO_3^- during inundation (Figure 2.6). One possibility is NO_3^- in tidal surface water infiltrates into the marsh subsurface and is subsequently consumed by dissimilatory nitrate reduction processes NO_3^- such as denitrification or DNRA (Giblin *et al.*, 2013; Devol, 2015). Alternatively, Elkhorn Slough

surface water has relatively elevated NH_4^+ concentration (Hicks *et al.*, 2019), which in combination with dissolved oxygen in tidal waters, can lead to nitrification in the marsh subsurface (i.e., the salt marsh can be a source of NO_3^-). Similarly, we observed small-scale within-marsh variation across positions and depths. Microbial processes such as dissimilatory nitrate reduction or nitrification are tightly coupled to plant activity, oxygen concentrations, and substrate availability (Koop-Jakobsen and Wenzhöfer, 2015). Although our study does not address the direct mechanisms causing variation in NO_3^- concentrations, our in situ high-frequency sensor measurements indicate that within-marsh processing exerts influence on net marsh NO_3^- export within the broader context of seasonal hydrologic drivers. Further, our findings highlight the importance of short-term and small-scale drivers of NO_3^- dynamics that might not be captured with point or synoptic measurements.

2.6.4 Implications for Salt Marsh Biochemistry

The analysis presented here illustrates the potential benefit of continuous high-spatiotemporal resolution water quality data in combination with methods to quantify tidal event hysteresis in salt marsh environments. Salt marshes are under pressure from chronic sea level rise and increasing human activity around coastal environments (Krause *et al.*, 2020). Although biogeochemical cycling of NO_3^- and other nitrogen species on coastal wetlands have been studied extensively (Bowen *et al.*, 2020), NO_3^- processing at intra-tidal time scales across different depths is not often considered.

The hysteresis indices used in this study indicate that the salt marsh has different dominant transport and biogeochemical processing behavior in wet and dry seasonal periods (Figure 2.7). Overall, the salt marsh is most retentive during the dry season, and depletion and consumption patterns dominate during these periods, whereas the salt marsh is least retentive during the wet season when NO_3^- producing dominates. This is particularly evident in the lower and upper marsh positions, where the salt marsh shifts between predominantly removing NO_3^- in dry periods and producing NO_3^- in wet periods.

These marked differences in the overall NO_3^- processing in the salt marsh as a function of seasonality may become more evident with changing patterns in precipitation (Donat *et al.*, 2016). Climate change in California is projected to cause less frequent, but more intense precipitation events (Swain *et al.*, 2018), already affecting salt marsh functionality (Russo *et al.*, 2013). Fewer, but more extreme precipitation events will likely result in relatively higher pulses of NO_3^- into the estuary during runoff events because NO_3^- will probably accumulate in the soil during rainless periods and get flushed during storm events. Predicted higher NO_3^- loads to Elkhorn Slough will test the potential of the salt marsh to remove pollutants and improve water quality in coastal systems.

2.7 Conclusion

This study identified the role of multi-scale (intra-tidal and seasonal) hydrologic drivers on controlling porewater NO_3^- concentrations in a Mediterranean-climate salt

marsh system, where water quality is a concern. High spatiotemporal resolution hydrologic and biogeochemical field measurements identified hysteresis in the transport and processing of nutrients in salt marsh environments. NO_3^- Hysteresis metrics were connected to spatial differences within the salt marsh and used to evaluate how this hysteretic relationship change over time (e.g., seasons). Overall, the knowledge obtained from this analysis of NO_3^- hysteretic responses to tidal events is valuable in providing insight into solute-subsurface water level patterns that occur due to inherent properties such as soil properties, marsh positions. The seasonal changes in NO_3^- dynamics over sub-hourly timescales highlight the significance of both long-term and high frequency continuous monitoring.

As global climate shifts, factors including sea-level rise will induce changes in marsh position functioning and ecological services. We used a relatively simple and robust methodology for evaluating key marsh biogeochemical processes. The methods presented here can assist in interpreting coastal processes, which can help with the urgency to predict future scenarios under sea-level rise conditions. Further, applying these techniques has potential transformative influence on our knowledge of coupled hydrological and biogeochemical processes in marsh ecosystems.

Future work should consider longer deployment and monitoring periods, particularly during the wet season, because the majority of the tidal events captured by this study corresponded to dry periods, and ideally across a range of wet, normal, and dry climate periods. More extended studies will help to resolve the role of varied hydrologic inputs, including runoff from agricultural activities and storm events. Further, similar studies in other coastal systems, including other salt marshes in different climatic regions,

are needed to put these findings into a comprehensive context. By integrating sites with varying degrees of tidal inundation and tidal patterns (e.g., diurnal and semidiurnal), we could better isolate tidal inundation from other salt marsh biochemical processes.

Future work should incorporate these high spatiotemporal field measurements of NO_3^- concentrations with additional monitoring data of salinity and isotopic fingerprints to understand mixing between terrestrial groundwater and inundation. We will also incorporate these field measurements with redox conditions to understand biogeochemistry, and biological surveys to understand the role of vegetation. An essential remaining step in the field is to implement these hydro-bio-geo-chemical processes into reactive transport modeling to develop practical mechanistic understanding, including explaining the interactions between flow paths, residence times, and solute kinetics in coastal systems. We think that an integrative understanding of physical and biogeochemical processes will be crucial for managing salt marshes as NO_3^- enrichment and sea-level rise continue to threaten our coasts.

2.8 Acknowledgement

This work was developed in collaboration with Dr. Erin Seybold. We would like to express our deepest gratitude to her for the many hours that we spent discussing about troubleshooting the many technical difficulties we encountered with the optical probe. The authors sincerely thank Dan Sampson from the University of California Santa Cruz for his valuable help programming and installing the electronic devices used in this study. EG was partially funded by a Cota-Robles fellowship through the

University of California Santa Cruz, and by a NOAA Margaret A. Davidson fellowship (NA20NOS4200122). We acknowledge support from the DOE SBR NITRATES Project, funded by the U.S. Department of Energy, Office of Science, Office of Biological and Environmental Research, Award Number DE-SC0021044. We acknowledge support from a California SeaGrant under California Natural Resources Agency Award Number C0303100.

Chapter 3 -Storage variability controls seasonal runoff generation in catchments at the threshold between energy and water limitation

3.1 Abstract

Annual water balance calculations may elide intra-annual variability in runoff generation, which could limit understanding of the similarities and differences between water- and energy-limited catchments. This may be especially important in comparisons between catchments close to the threshold between water- and energy-limitation. For this study, we examined runoff generation as a function of catchment storage in four watersheds, with focus on two that exist close to these thresholds, to identify how year-to-year variability in storage that results in intra-annual variations of runoff generation efficiency. Specifically, we focused on one energy-limited catchment in the humid subtropics and one water-limited catchment in a Mediterranean climate. We used measured and calculated daily water balance components to calculate variations in the relative magnitude of daily storage. We isolated precipitation events to draw connections between storage and runoff generation at intra-annual scales and compared our findings to the same metrics in two intensely energy-limited landscapes.

We observed distinct stages in daily storage across water years in watersheds at the threshold, where systems experienced wet-up, plateau, and dry-down stages. During the wet-up, precipitation was partitioned to storage and runoff ratios (*RR)* were low. In the plateau, storage was filled and precipitation was partitioned to runoff, causing high *RR*s. During the dry-down, storage decreased as precipitation was partitioned to

evapotranspiration and runoff, causing low *RR*s. The critical role of evapotranspiration during the growing season resulted in relatively higher *RR*s during the wet-up than during the dry-down for a given storage value. Thus the same storage amount was partitioned to evapotranspiration or runoff differently throughout the year, depending on the storage stage. Despite their different positions on opposite sides of the threshold, the similarity between the two focus catchments suggests a potential characteristic behavior of systems at the threshold common to both humid and semi-arid landscapes.

3.2 Introduction

Precipitation partitioning between storage (*S*) and discharge (*Q*) is non-linear, dynamic, and challenging to predict. The response characteristics of *Q* (i.e., runoff ratios, magnitudes, recession rates) remain notoriously challenging to predict (Spence, 2010; Davies and Beven, 2015). Even in the same catchment, varying *Q* responses to precipitation have been observed to depend on season or antecedent wetness conditions (Tromp-van Meerveld and McDonnell, 2006). The mechanisms mediating *Q* generation are often based on threshold-controlled processes, produced by variability in *S* capacity at the hillslope or catchment scale (Detty and McGuire, 2010), and are still incompletely understood.

Previous studies have focused on the hysteretic behavior of *S*-*Q* relationships to describe catchment response to precipitation (*P*) events (e.g., Davies and Beven (2015); Hailegeorgis *et al.* (2016)). For example, characteristic curves of *S*-*Q* relationships have been used to describe periods of "storing" (i.e., when dominant *P* partitioning processes cause the *S* increase to be much higher than the *Q* increase) and "contributing" (i.e.,

when *P* is preferentially partitioned to *Q* instead of *S*) in an arid watershed in the sub-arctic Canadian shield (Spence *et al.*, 2010). However, the dynamics of *S* at intra-annual time scales (e.g., aggregated precipitation events or monthly aggregates) remain poorly understood in many hydroclimates. As climate is often observed to serve as a first-order control on *Q* generation, Spence *et al.* (2010) suggested that more catchment comparison work across different hydroclimates is needed to identify generalizable characteristics of *S*-*Q* relationships.

The hydroclimate of a watershed refers to the influence of climate on dominant hydrological and ecohydrological processes, and it can be described as the balance between water demand and supply. Commonly, *P* is used to describe water inputs and evapotranspiration (*ET*) to describe energy inputs. Energy-limited systems are characterized as systems where actual *ET (AET)* is approximately equal to potential *ET (PET)* because there is sufficient water supply to meet the *PET* demands. Water-limited systems are characterized as systems where *AET* is limited by water availability, so *PET* is not met. Event *P* partitioning across the spectrum of water-limited and energy-limited systems displays marked differences (Jones *et al.*, 2012; Garcia and Tague, 2015). In wet, energy-limited systems, *S* may never go below threshold values needed for *Q* generation, and thus *P* can be consistently and preferentially partitioned directly to *Q*. Contrastingly, *S* is more likely to change in drier, water-limited systems during wet and dry periods. Therefore, in water-limited systems, it might be more evident that *P*'s partitioning to *Q* might vary as a function of the *S* level of the system.

The water balance of a watershed, which describes differences in the water input, output, and *S* components, can be helpful for detangling hydroclimatic classifications.

Water balance calculations are typically applied at time scales long enough (>1 yr) that residual (S) can be assumed to be negligible. This helps facilitate catchment classification in terms of long-term hydroclimatic averages (e.g., in a Budyko (1974) space for water- and energy-limited catchments) or to estimate one of its unknown components (often evapotranspiration, ET) from the other measured components (Rouholahnejad Freund and Kirchner, 2017). The wetness index, used in the Budyko (1974) space, which is described as the ratio of P relative to PET (Wagener *et al.*, 2007), is a relatively simple method to visualize the hydroclimatic spectrum. However, differences or similarities regarding the mechanisms driving P partitioning to S or Q and the S~Q relationships at intra-annual scales across watersheds on the hydroclimate spectrum are primarily unknown (Reaver *et al.*, 2022).

Overarching hydroclimatic conditions might be a primary driver of event P partitioning characteristics, but interannual variability in total P may also play a critical role. Year-to-year variability in P may cause deviations of P partitioning from expected hydroclimatic behavior. For example, Nippgen *et al.* (2016) showed that P partitioning in a series of humid catchments in the Coweeta Hydrologic Laboratory in the southeastern United States varied between water-limited and energy-limited during dry and wet years, respectively. They also found that the annual P from the previous year was as significant as the current year's annual P for explaining the annual runoff ratio (RR).

The intra-annual variability in P partitioning may not explain the differentiation between water- and energy-limited catchments, especially in catchments where the long-term hydroclimate characterizes them near the threshold between water- and energy-limitation ($P/PET = 1$). To address this knowledge gap, we used measured and

calculated daily parameters of the water budget in energy-limited and water-limited catchments to identify event, daily, and seasonal *P* partitioning behavior. Through this, we provide testable hypotheses for dominant and potentially universal controls on hydrologic partitioning through the lens of characteristic storage states. The present study extends over multiple water years and across four study catchments that span part of the hydroclimatic spectrum to understand differences and similarities in storage-driven hydrologic partitioning. Two catchments, one in the southeastern United States' humid subtropics (Calhoun Critical Zone Observatory (CZO)) and one in the semi-arid central coastal California (Tilden), fall on different sides of the water-/energy-limitation threshold, but experience year-to-year precipitation variability that causes these catchments to periodically switch between water- or energy-limited on an annual time scale. We compared results from these two catchments with two wetter, energy-limited catchments that do not switch designations, one maritime (Lower Hafren) and one tropical (Luquillo CZO). We used relative catchment storage to infer how other water balance parameters may control changes in *Q* processes at intra-annual timescales. Relative storage is an integrative variable of the water balance that incorporates current and antecedent hydrologic conditions. We chose this water balance-based approach to maximize comparability across catchments while also allowing us to identify opportunities for a more spatially distributed study.

3.3 Methods

3.3.1 Research Catchments

We primarily focused this study on two catchments located in humid and semi-arid climates. We compared the *P* partitioning from these catchments with two ancillary catchments from a maritime and a tropical climate, respectively.

The study system at Calhoun CZO is a 0.069 km^2 headwater catchment located in South Carolina, United States (U.S.; Figure 3.1). This area is part of the humid subtropical region of the Lower East Coast of the U.S. and is characterized by hot, humid summers and mild winters. Calhoun is located in an energy-limited hydroclimate, albeit near the threshold between water- and energy-limited conditions (Wlostowski *et al.*, 2021). The catchment receives an average of 1200 ± 617 mm of *P* annually (1950-2015), evenly distributed across the year (~100 mm per month; Mallard, 2020). The mean annual *ET* is 800 ± 23.4 mm and the mean annual temperature is 16.3 ± 3.2 ^{0}C (Mallard, 2020). The catchment has a total relief of 50 m, with elevations ranging from 124 to 173 m, and a median slope of 19% with a standard deviation of 13%. Soils are primarily Ultisols of the Appling, Cecil, and Madison soil series. These soils can be generally described as loamy sands overlying clay-rich argillic horizons, underlain by deeply weathered saprolite material (Richter *et al.*, 2000). Soil depths generally increase moving away from the stream channel in Calhoun. Specifically, soil depths range from <1 m in or adjacent to stream channels to 4 m on narrow ridge tops to >9 m at Calhoun's upper divide, where it connects to a broader interfluve. The underlying geology is primarily granitic gneiss, the most common bedrock in the region. This headwater catchment is primarily forested in mixed hardwoods (e.g., *Carya spp.* and *Quercus spp.*) with minimal pine stands (*Pinus spp.*). Calhoun contains a non-perennial stream network that dries

completely in the summer through early fall and flows primarily in late winter and early spring.

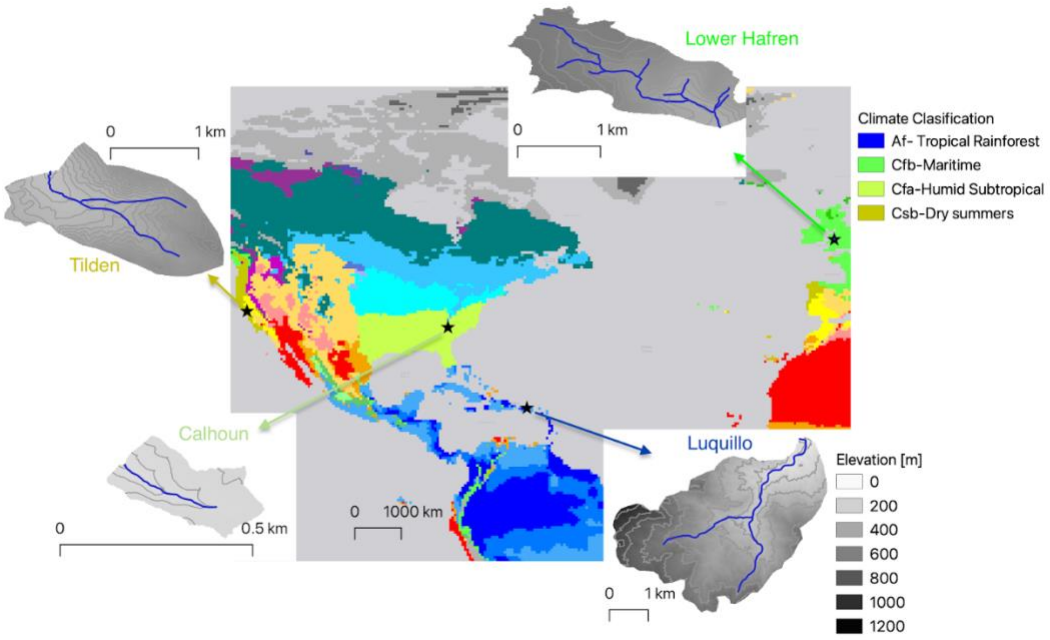

Figure 3.1 Global map with the location of each study catchment starred. The hydroclimate classification is shown in color. The climates legend only shows the four relevant climates for this study. Subset maps depict topography and catchment boundaries. Note the differences in scale between the catchments.

The Tilden watershed is a 3.4 km^2 headwater in Berkeley, California, U.S. (Figure 3.1) and is characterized by a Mediterranean water-limited hydroclimate, although near the threshold of water-energy limitation and can be energy-limited during extremely wet years. This system annually receives 930 ± 332 mm of P (2004 to 2018), with 80% of *P* occurring over the winter and spring months, a mean annual *ET* of 1030 ± 30 mm, and a mean annual temperature of 14.5 ± 7.6 °C (Grande *et al.*, 2020). Tilden has a total relief of 300 m, with elevations ranging from 282 to 580 m and a median slope of 16%

with a standard deviation of 8.5%. The headwater is characterized by well-drained clay-loams and loam soils, formed in material weathered from mafic igneous rocks, varying in thickness from 0.3 to 1 m (Contra Costa Soil Survey, 1981). The area is underlain by a syncline, whose axis delineates the stream's course (Graymer, 2000) and likely controls the direction of groundwater flow (Grande *et al.*, 2019). The Moraga Formation (Basalts from the Pliocene), which underlies the alluvium over much of the catchment, is of particular importance as a potential reservoir of groundwater. With a thickness of 10-25 m, it is considered one of the most important units for conducting groundwater flow in the study area (Zhou *et al.*, 2003). Mixed forest covers approximately 48% of the watershed, evergreen forest covers 21%, shrubs and grasslands cover 20%, and the remaining 11% is covered by developed areas, including a golf course. A peculiarity of this catchment is the presence of a periodically irrigated golf course, which is an additional source of water considered in the water balance, albeit a minor one (Grande *et al.*, 2020). A perennial stream drains the watershed.

Lower Hafren is a 3.5 km^2 experimental catchment in Wales, UK (Figure 3.1), where hydroclimatic data has been collected for decades. Lower Hafren is located in the cool-humid Cambrian Mountains. The catchment is energy-limited and receives a mean annual P of 2952 $\pm$ 426 mm (1993 to 2008), with a mean annual ET of 591 $\pm$ 56 mm and a mean annual temperature of 9.7 $\pm$ 8.3°C. Lower Hafren has a total relief of 310 m, with elevations varying from 670 to 360 m, with a median slope of 12% and a standard deviation of 15%. Stagno-podzols predominantly characterize Lower Hafren, but acidic peat, acid brown earth, and stagno-gleys occur. Lower Paleozoic slate, mudstone,

greywacke, and sandstones compose the underlying geology (Harman, 2015). Lower Hafren is dominated by coniferous plantations (*Sitka Spruce* dominant).

Luquillo is a 17.8 km^2 watershed part of the Luquillo CZO in Puerto Rico (Figure 3.1), where hydroclimatic data has been collected for decades. Luquillo is located in a tropical rainforest climate. This watershed is energy-limited and receives a mean annual *P* of 3132 ± 1093 mm (Silver and Leon, 2019), the mean annual temperature is 24.2 ± 4.1 ^{o}C, and the mean annual *ET* is 1305 ± 243 mm (Zimmerman, 2018). The catchment has a total relief of 760 m, with elevations varying from 4740 to 5500 m and a median slope of 28% with a standard deviation of 12%. Inceptisols and oxisols dominate the area, varying in thickness from 1 to 9 m, underlined by Cretaceous volcaniclastics (Buss *et al.*, 2013). Luquillo is predominantly covered by Tabonuco, Palm, and Colorado forests.

Because all the watersheds used in this study are located in the northern hemisphere, hereafter, we use seasons for the northern hemisphere. Spring extends from March to May, Summer from June to August, Fall from September to November, and Winter from December to February. Further, the water year is considered to span from October 1st to September 30th, to encompass the rainy season for regions with strong seasonality in precipitation.

3.3.2 Data Description

We employed daily data collected by the authors from Calhoun and Tilden and publicly available hydroclimatic data from Lower Hafren and Luquillo. Data from Calhoun are from the 2015 water year (total *P* in the 35th percentile) and the 2016 water

year (total *P* in the 79th percentile) and at Tilden to the 2017 water year (total *P* in the 100th percentile, the wettest year in the available record) and the 2018 water year (total *P* in the 40th percentile). Thus, we chose data from Lower Hafren (1992 water year and 2007 water year in the 40th and 92nd percentile, respectively) and Luquillo (2008 water year and 2010 water year in the 44th and 94th percentile, respectively) to capture similar precipitation percentiles across all four study catchments. Herein, we use 'Normal' and 'Wet' water years to refer to the water years in each catchment's lower and higher *P* percentile, respectively (Table 3.1).

Table 3.1 Summary of annual water budget components by water year for each study catchment. RR is runoff ratio.

Catchment	WY	WY type	P [mm]	P percentile	ET [mm]	Q[mm]	RR	ET/P
Lower Hafren	2007	Wet	3228	92nd	656	2659	0.82	0.20
Lower Hafren	1992	Normal	2651	40th	554	2001	0.75	0.20
Luquillo	2010	Wet	5331	94th	1311	3858	0.72	0.25
Luquillo	2008	Normal	3678	44th	1216	2825	0.77	0.33
Calhoun	2015	Normal	1159	35th	782	198	0.17	0.67
Calhoun	2016	Wet	1410	79th	775	554	0.39	0.55
Tilden	2017	Wet	2353	100th	1049	1054	0.45	0.45
Tilden	2018	Normal	994	40th	1005	310	0.31	1.01

The data from Calhoun were collected and maintained as described in Mallard (2020). Briefly, *P* was measured at the site with a tipping bucket rain gauge at a 0.1 mm/tip resolution. *Q* was calculated using stage measurements with redundant capacitance rods (TruTrack, ±1 mm) at five-minute intervals installed in the pool of a 90° v-notch weir built at the catchment outlet and was summed to daily. *PET* was determined from the Thornthwaite equation (Thornthwaite, 1948a) using temperature data from the site. We assumed that in energy-limited watersheds (e.g., Calhoun, Lower Hafren, and Luquillo), $AET \cong PET$.

Tilden's data was published in Grande et al. (2020). Briefly, *P* records were obtained from the open-access California Data Exchange Center (California Data Exchange Center - Query Tools) operated by the California Department of Water Resources, which has an extensive hydrologic data collection network that includes *P*, with one station within the studied catchment. *P* was measured with a tipping bucket rain gauge, and data have been available for this location since February 2004. A particularity of this catchment is the presence of a periodically irrigated golf course (Grande *et al.*, 2019, 2020). Because irrigation water is only applied in a small area of the watershed, and because this water is a small fraction compared to *P* (less than 3% over the two-year period studied here), we combined the depth of irrigation water with *P* and considered them as a single component in the water budget. The stream stage was measured at an interval of 20 minutes with a pressure transducer (*In-Situ* Aqua Troll multi-parameter meter Denver, Colorado, US), deployed in the same location since 2015 and maintained by the East Bay Regional Park District (EBRPD). *Q* was calculated from stage using a rating curve constructed by EBRPD staff. A correction factor was applied to flagged measurements of *Q*, as described in Grande *et al.* (2020). *ET* data were provided by Formation Environmental LLC (CalETa), which developed, with support from the California Department of Water Resources, a data set for mapping daily *AET* through satellite observations (Paul *et al.*, 2017).

The data used from Lower Hafren was previously used by Harman (2015), and over three decades of daily hydroclimatic data are available. *P* was measured at two weather stations within the watershed boundary and then averaged to obtain a single mean daily value. *Q* was calculated from stage measured in 90° v-notch weir installed at

the watershed's outlet. *PET* was calculated from hourly automatic weather stations using the FAO Penman-Monteith equation (Allen *et al.*, 1998). Hydroclimatic data from Luquillo is available through the Luquillo CZO database. *P* and *Q* datasets are available from Silver and Leon (2019), collected from stations managed by the U.S. Geological Survey and the U.S. Forest Service, and meteorological data are available from Zimmerman (2018). For Luquillo, we calculated *PET* from the Thornthwaite equation (Thornthwaite, 1948b) using temperature data from Zimmerman (2018).

3.3.3 Data Analysis

3.3.3.1 Catchment Storage

Catchment storage was defined as an aggregated metric, combining various reservoirs (e.g., soil, regolith, bedrock). The daily catchment water budget was evaluated as:

$$\Delta S = P - Q - ET \tag{3.1}$$

Where ΔS is daily change in catchment S (mm/d), P is daily precipitation (mm/d), Q is daily runoff (mm/d), and ET is daily evapotranspiration (mm/d). Relative storage (mm) for each day (t) was estimated as:

$$S = \int_{t_0}^{t} (P - Q - ET)dt \tag{3.2}$$

Relative S was calculated from the water fluxes described in the above sections for two water years at each study site, an Normal water year and a wet water year (Table 3.1). In equation 2, t_0 is the first day of the water year (October 1st), and $S_0 = 0$ at t_0. In

the two watersheds at the threshold of water-energy limitation, October 1st corresponds to the driest part of the year. Thus, we assumed that *S* was at a minimum at the start of the water year. We calculated antecedent *S* as the value of *S* on the first day of a *P* event. Further, we examined the relative water balance for individual *P* events (section 2.3.2), and relative *S* (mm/d) was recalculated for each event, starting at a relative value of zero (S_0=0).

3.3.3.2 Precipitation Event Delineation and Characterization

Hydrologic partitioning studies are often conducted over individual precipitation events. However, delineating precipitation events is not consistent throughout the scientific literature. Precipitation events may refer to specific periods during which *P* falls in a catchment. For example, Singh *et al.* (2018) classified precipitation events as periods with at least 30 min of rainfall with total rainfall greater than 20 mm, and events were separated by at least 3 hours with no rainfall. Rinderer *et al.* (2016) defined precipitation events based on a *P* threshold of 5 mm, the average *P* for days when rainfall occurred, and events were separated by at least 2 hours without measured *P*.

Rainfall events have also been delineated from the hydrograph times series. Some studies have used a threshold value of *Q* (Rose and Peters, 2001), a percentage threshold in response to groundwater height change (Meerveld *et al.*, 2015), and baseflow separation to delineate events (Merz *et al.*, 2006; Blume *et al.*, 2007). Detty and McGuire (2010) used an inclusive approach where they defined events as the interval from the

start of *P* to the end of quickflow, defined as the portion of the hydrograph composed of stormflow contributions from rapid surface runoff or interflow. McCarter *et al.* (2020) used a similar approach where they selected precipitation events from the onset of *P* to the time when *Q* had receded to near or pre-event conditions, and changes in *Q* were < 0.1 mm/day for two consecutive days. Lastly, studies such as that of McGlynn and McDonnell (2003a, 2003b) zoomed in on a single or a few events with no rigorous definition stated.

Here, we defined precipitation events from the onset of $P \geq 1$ mm/day to when *Q* had receded to 120% of pre-event conditions or when another event started (marked by a positive slope in the hydrograph) before *Q* receded back to the 120% threshold. Considering that the precipitation regimes vary across the studied catchments, and since our approach requires us to extract periods across the entire water year for comparison, we used this inclusive approach of using both *P* and *Q* to delineate precipitation events. We identified 301 events across the study period, with 89, 54, 84, and 74 events from Calhoun, Tilden, Luquillo, and Lower Hafren, respectively (shaded regions in Figure 3.2).

We calculated the runoff ratio (*RR*) by dividing event flow by total rainfall. Event-flow was calculated using a baseflow separation algorithm (Sujono *et al.*, 2004) in the EcoHydRology R package (Fuka *et al.*, 2018). For analyses comparing precipitation events across sites, we used average event values (e.g., *Q* or *P* in mm/d) of each water balance parameter because the lengths of the precipitation events were highly variable.

3.4 Results

3.4.1 Annual Hydrologic Budget

The normal water year at Calhoun totaled 1159 mm of *P*, representing ~41 mm less than the mean annual *P* (Figure 3.2). *ET* and *Q* removed 782 mm and 198 mm during the water year, respectively. The annual *RR* during the Normal water year was 0.17 and *ET*/*P* was 0.67 (Table 3.1). The wet water year began with Hurricane Joaquin in late September 2015 (NOAA, 2015), bringing approximately 300 mm of rainfall over one week, representing 20% of the total *P* in the water year (1410 mm, Figure 3.2). This resulted in a "wetter" water year with a higher *Q* of 554 mm and a corresponding higher runoff ratio than the normal water year (0.39). In contrast, *ET* was 775 mm, only 7 mm lower than the previous, somewhat drier water year. During the wet water year, *ET*/*P* was 0.55.

The normal water year at Tilden received 994 mm of *P*, 64 mm higher than the mean annual value for the catchment. Annual *ET* for the normal water year was 1005 mm, annual *Q* was 310 mm , the annual *RR* was 0.31, and *ET*/*P* was 1.01 (Table 3.1). The wet water year at Tilden was one of the wettest water year on record, with a total *P* of 2353 mm, doubling the 14-year annual average for the area (Figure 3.2). *ET* removed 782 mm of water from the catchment during this period, the annual *RR* was 0.45, and *ET*/*P* was 0.45. Although there were noteworthy differences in *P* between the two water years presented here, *ET* was not substantially different between the two water years, implying that higher *P* values do not necessarily produce higher *ET*. On the other hand, *Q* is three times higher in the wet water years than in the

normal water years. Moreover, in Tilden we found a shift between water-limited in the normal water years and energy-limited in the wet water years (Table 3.1).

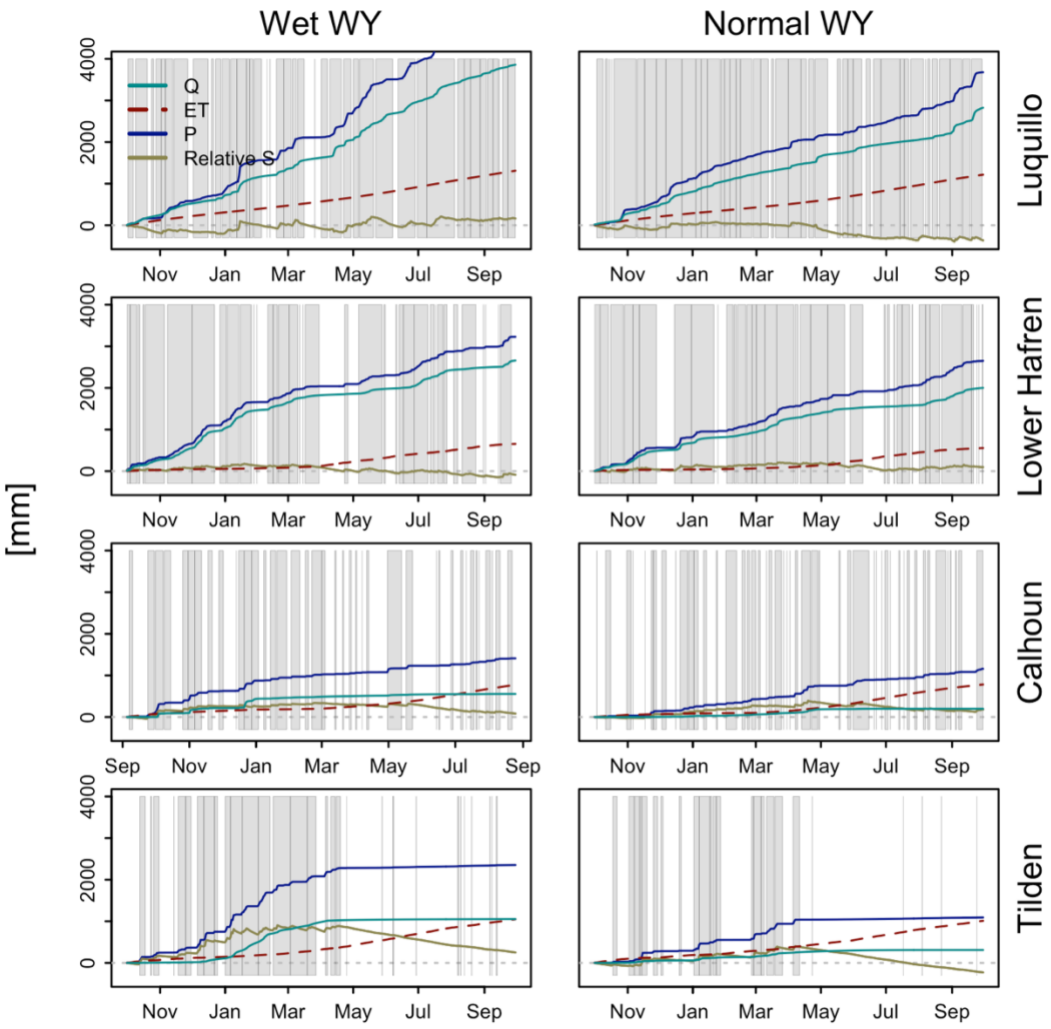

Figure 3.2 Cumulative daily values of precipitation (*P*; blue line), evapotranspiration (*ET*; green), runoff (*Q*; teal), and relative storage (*S*; red) over two full water years for the four study catchments. The shaded regions mark each of the 301 precipitation events analyzed in this study.

Lower Hafren is characterized by a relatively high annual *RR* (~0.8), with *ET* removing 605 ± 72 mm (~20% of *P*) for the two water years. Similarly, Luquillo is characterized by a relatively high *RR* of ~0.75 for the two studied water years,

and *ET* was responsible for removing 1264 ± 67 mm (~25% of the *P*) over the studied period.

Catchments across the hydroclimatic spectrum studied here show that *P* is spatiotemporally variable, ranging from 994 mm/y in the normal water year at Tilden to 3228 mm/y in the wet water year at Luquillo. However, water outputs, particularly *ET*, are not as highly variable, ranging between 591 mm/y during the normal water year at Lower Hafren and 1311 mm/y in the wet water year at Luquillo. This discrepancy between the variability in water and energy inputs is reflected in the runoff variability, where catchments that receive more *P* have more extensive *Q* (e.g., Lower Hafren, Luquillo). Furthermore, *ET*/*P* is highly variable across sites, ranging from 0.2 at Lower Hafren to 1.01 at Tilden (Table 3.1), driven by P variability (Figure 3.2).

Although *P* is only 250 mm higher (~1.2 times higher) in the wet water year at Calhoun than in the normal water year (1410 mm and 1159 mm, respectively), *Q* is 2.8 times higher. This indicates that the somewhat slight increase in *P* caused a substantial increase in *Q*. At Tilden, *Q* was 3.4 times higher in the wet water year than in the normal water year, but annual *P* was 2.3 times higher, suggesting that a significantly higher *P* is needed to achieve higher *RR*s at Tilden (Table 3.1). The catchments on the far end of the energy-limited spectrum (i.e., Luquillo and Lower Hafren) displayed somewhat negligible differences in the water budget components from year to year.

There is considerable contrast in *P* event frequency between Tilden and the other three catchments. While *P* was somewhat equally distributed over the water year at the other sites, *P* was restricted to late fall and early spring at Tilden, with 94 ± 6% of *P*

occurring between October and April. On the other hand, *ET* is seasonal in all catchments, with a marked increase in April or May. The *ET* seasonality is somewhat less pronounced in Luquillo, where high temperatures year-round and dense vegetation remove water from the catchment uniformly throughout the water year.

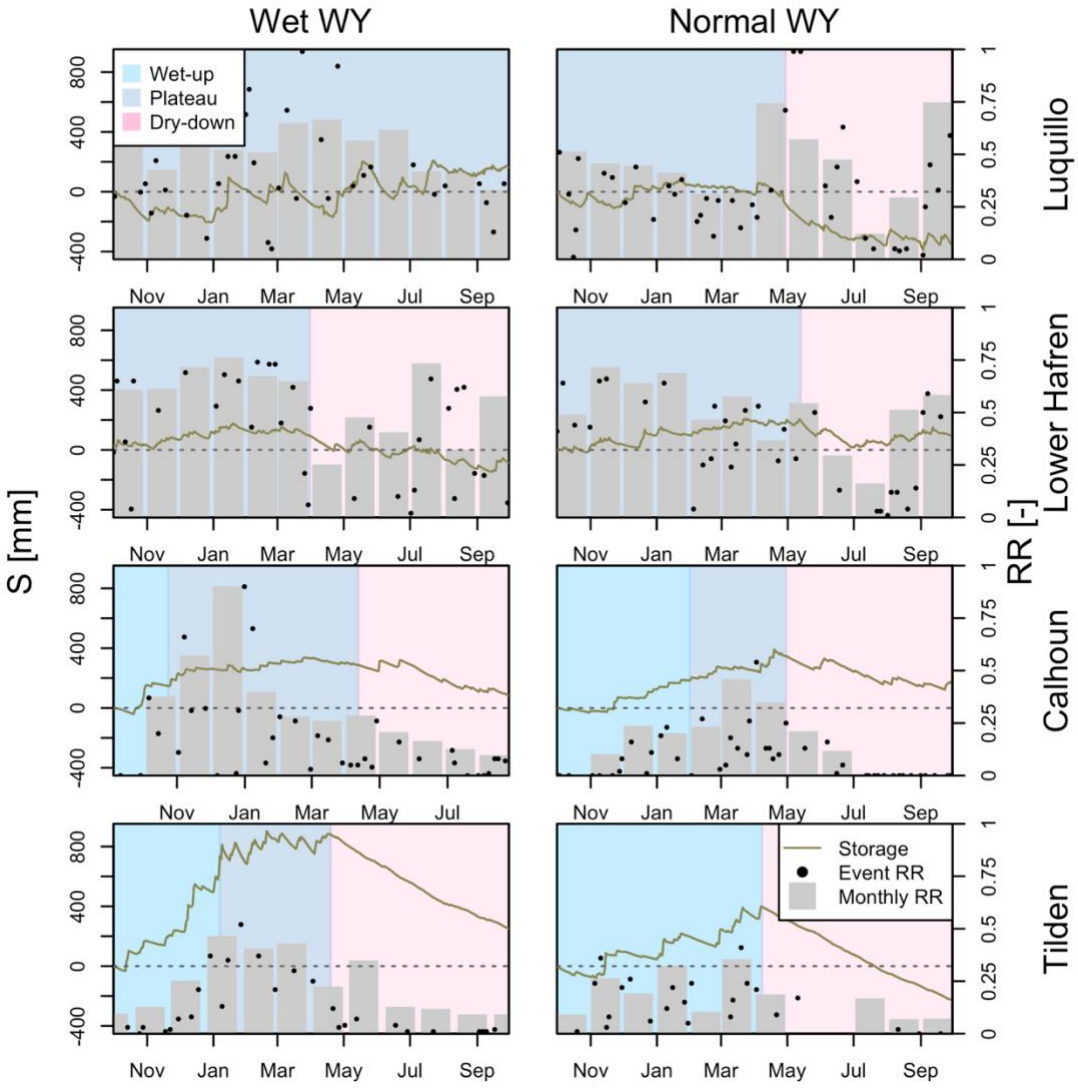

Figure 3.3 Relative catchment storage (line) delineated by the different storage stages (color boxes). Light blue demarcates the wet-up stage, dark blue represents the plateau stage, and the wet down stage is marked by the red color. The bars illustrate monthly runoff ratios (secondary vertical axis). The black points show event runoff ratios. All runoff ratios were calculated as event flow over total rainfall.

3.4.2 Precipitation Partitioning Across Variable Antecedent Storage Conditions

For the selected events in the wet water year in Calhoun (2015), *P* was 0.6 to 28.5 mm/d in summer and fall respectively (median = 6.6 mm/d). Event *ET* varied between 0.2 and 4.6 mm/in winter and summer, respectively (mean = 2.3 mm/d). Event *Q* ranged between 0 (i.e., no flow or below detection limit) and 19.4 mm/d in summer and winter, respectively (mean = 1.7 mm/d). Event *RR* was 0 to 0.9 for summer and winter, respectively (mean = 0.2).

For the selected events in the normal water year at Calhoun (2016), event *P* varied between 0.4 and 20.7 mm/d in spring summer and spring, respectively (mean = 0.4 mm/d). Event *ET* was 0.2 to 4.4 mm/d in winter and summer, respectively (mean = 2.2 mm/d). Event *Q* was 0 to 4.7 mm/d in summer and spring, respectively (mean = 0.5 mm/d). Event *RR* varied between 0 and 1 in summer and winter, respectively (mean = 0.1). In both water years from Calhoun, the event *RR*s increased from the onset of the water year and then decreased in mid-to-late spring (Figure 3.3).

At Calhoun, *P* partitioning to *S* varied between 0 (no *P* was partitioned towards storage) and 97%. These variations in *P* partitioning were seasonal, with the largest partitioning to *S* at the beginning of the water year (e.g., Figure 3.4A) and the largest partitioning towards *Q* occurring in the winter and spring (e.g., Figure 3.4B). A predominant partitioning of *P* to *ET* was observed for events in mid and late summer (e.g., Figure 3.4C).

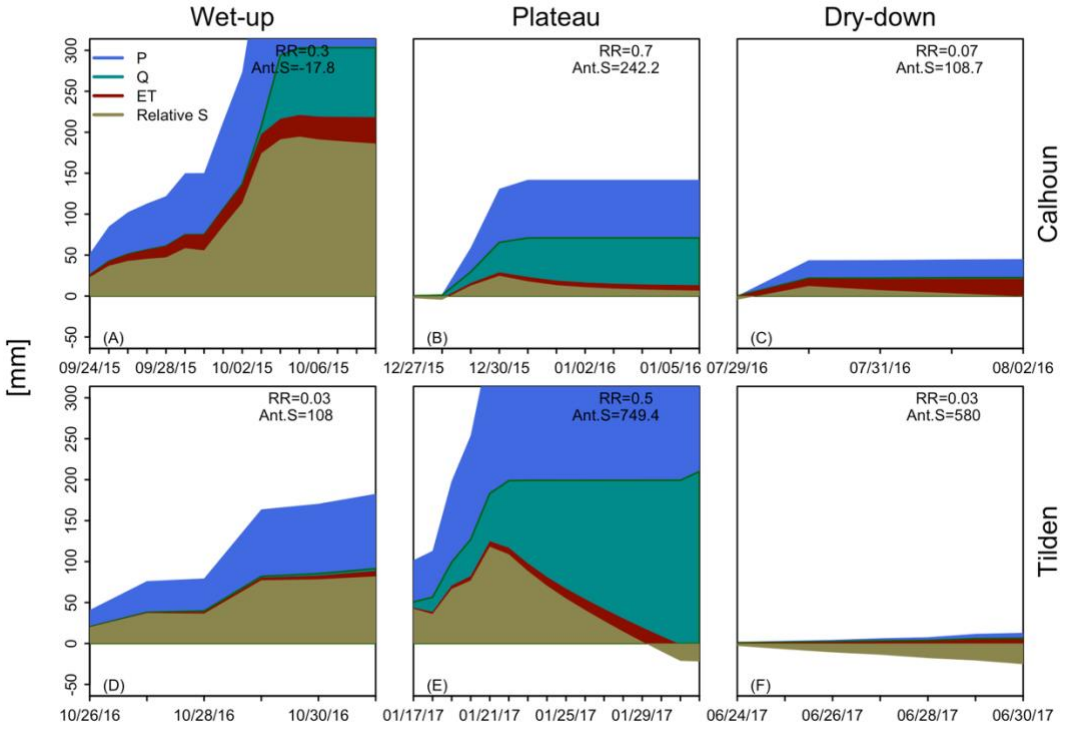

Figure 3.4 Specific precipitation events across the three catchment storage stages (wet-up, plateau, dry-down), illustrating changes in the relationship between storage and runoff. In the wet-up period, *S* increases and *RR*s are low. During the plateau, storage stays relatively constant while runoff is generated. During the dry-down, *S* and *RR* decrease. S is zero-ed out at the beginning of each event and integrated over the length of the event. The value of relative storage (*S*) for the water year on the first day of the event is listed as Ant. *S* (antecedent storage) in the upper right-hand corner of each plot.

During the wet water year at Tilden (2018), event *P* varied between 1.1 and 35.3 mm/d in summer and winter, respectively (mean = 10.7 mm/d). Event *ET* was 0.3 to 4.8 mm/d, in winter and summer, respectively (mean = 1.8 mm./day). Event *Q* was 0 to 10.2 mm/d, in summer and winter, respectively (mean = 1.8 mm/d). Event *RR* was 0 to 0.52 (mean = 0.1), with the higher values in winter.

During the normal water year (2017), event *P* was 0.3 to 25 mm/d in late spring and summer, respectively (mean = 8.4 mm). Event *ET* was 0.5 to 5.4 mm/d in winter

and summer, respectively (mean = 2 mm/d). Event *Q* ranged between 0 and 3.3 mm/d in summer and spring, respectively (mean = 1.3 mm/d). Event *RR* was 0 to 0.41 (mean = 0.14). Like in Calhoun, the event *RR*s tended to increase as the water year progressed and decreased in spring, with the onset of the growing season (Figure 3.3).

Like in Calhoun, *P* partitioning was seasonal at Tilden. Early in the water year, *P* was partitioned preferentially towards *S* (e.g., Figure 3.4D), and predominant *Q* partitioning was observed in winter and early spring (e.g., Figure 3.4E). In Tilden, *P* partitioning to *S* varied between 0 and 90%. The somewhat smaller events in Tilden during the summer indicated that *P* is partitioned to *S* but because *ET* is high during this time, it depletes *S* back down (e.g., Figure 3.4F).

At Lower Hafren, event *P* was 1.25 to 25.3 mm/d (Table 3.2), with the most substantial events occurring in late fall and winter, with large events still occurring in summer. Event *ET* varied from 0.3 to 5.4 mm/d in winter and summer, respectively. Event *Q* ranged between 0.7 and 25.4 mm/d in summer and late fall. Event *RR*s were relatively high, with a mean of 0.4 across all seasons.

In Luquillo, the largest event accumulated 45.5 mm/d of *P* during summer, and the smallest event accumulated 0.2 mm/d in the fall. During the two water years analyzed, event *ET* varied between 4.5 and 2.29 mm/d in summer and winter, respectively. Event *Q* ranged between 27.7 mm/d and 2.7 mm/d in spring and late fall respectively. The event *RRs* were relatively high, with a mean value of 0.4.

Table 3.2 Summary statistics of the precipitation events analyzed in this study. SD refers to the standard deviation.

	Calhoun	Tilden	Lower Hafren	Luquillo

Max P [mm/d]	28.5	35.3	25.3	45.5
Min P [mm/d]	0.4	0.84	1.25	0.2
Mean P [mm/d]	6.3	10	9.4	12.1
Median P [mm/d]	5.2	7.3	7.8	8.3
SD P [mm/d]	5.3	8.9	5.4	10.1
Max Q [mm/d]	19.7	16.9	21.4	27.7
Min Q [mm/d]	0.0	0.0	0.7	2.7
Mean Q [mm/d]	1.2	2.4	6.1	8.4
Median Q [mm/d]	0.4	1.0	4.8	7
SD Q [mm/d]	2.8	3.5	4.6	5.4
Max ET [mm/d]	4.6	5.4	4.4	4.5
Min ET [mm/d]	0.2	0.3	0.2	2.29
Mean ET [mm/d]	2.2	1.9	1.4	3.4
Median ET [mm/d]	1.7	1.7	1.1	3.3
SD ET [mm/d]	1.5	1.2	1.0	0.7
Max RR [-]	1	0.5	1	1
Min RR [-]	0	0	0.01	0.01
Mean RR [-]	0.1	0.1	0.4	0.4
Median RR [-]	0.1	0.1	0.4	0.3
SD RR [-]	0.2	0.1	0.25	0.25
Max length [d]	16	17	24	27
Min length [d]	1	1	1	1
Mean length [d]	4	5.1	6	8.1
Median length [d]	3	4.5	6.3	7
SD length [d]	3	4.2	6	4.8
n	89	54	74	84

3.4.3 Hysteresis in the storage dependency of runoff generation

In the catchments at the water-/energy-limitation threshold, we observed low *RR* and antecedent *S* values at the start of each water year. Relatively higher *RR* occurred at higher values of antecedent *S* as the water year progressed into the dormant winter

(Figure 3.3). However, antecedent *S* and *RR* declined during the growing season as *ET* became a more prominent water balance component. This decline occurred in watersheds across all the studied hydroclimates, except for Luquillo in the wet water year. Based on this common pattern in S across water years and sites, we categorized *S* seasonality into three different stages: wet-up, plateau, and dry-down (Figure 3.3).

Catchments on either side of the water- and energy-limited threshold display different *S*-*RR* relationships (Figure 3.5), and even catchments at the threshold exhibit different behavior. In the catchments near the water-/energy-limited threshold (Tilden and Calhoun), the *S*-*RR* relationship revealed hysteretic behavior with a clockwise direction across each water year (Figures 3.5b and d). The water-limited catchment (Tilden) displayed large variability in antecedent *S* and a relatively small range of *RR*, which drove the hysteretic loop into a wide clockwise loop. Calhoun, the energy-limited catchment, showed greater variability in *RR* compared to Tilden and a relatively small range of antecedent *S*, causing a narrower and taller hysteretic loop (Figure 3.5). In contrast, hysteretic behavior was not observed in the *S*-*RR* relationship for the strongly energy-limited watersheds (i.e., Luquillo and Lower Hafren; Figures 3.5a and c). In these systems, *P* appeared to be frequent enough to maintain an elevated catchment *S*, thus *S* was not as variable in Luquillo and Lower Hafren as in catchments near the threshold. This process leads to flashier streams in these strongly energy-limited catchments, explaining their more linear runoff response to precipitation events.

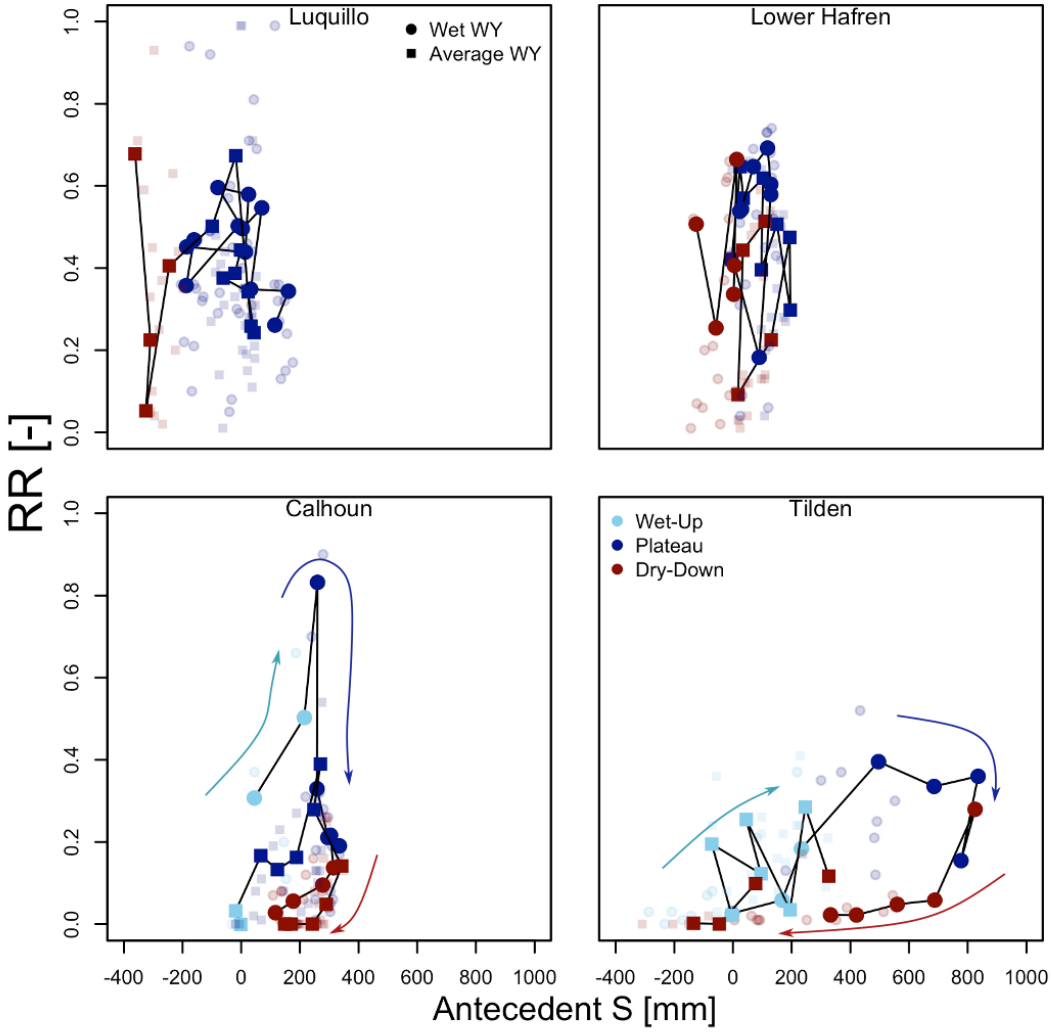

Figure 3.5 Runoff ratio (RR) vs. Antecedent Storage across the four studied watersheds. The colors indicate the different stages of catchment storage (light blue, blue, and red indicate wet-up, plateau, and dry-down, respectively). The shape of the symbol indicates the type of water year (square and circle for average and wet water years, respectively). The larger, opaque symbols represent monthly data while the smaller, transparent symbols correspond to individual events. The arrows in the Calhoun and Tilden plots highlight the clockwise hysteresis observed in these landscapes.

3.5 Discussion

While watershed hydrology and hydroclimatology research efforts in recent decades have advanced our understanding of *P* partitioning to *S* or *Q*, we have limited approaches that can generalize and quantify *P* partitioning mechanisms affected by intra-annual variations in hydroclimatic properties (e.g., temperature, precipitation). Further, we have limited comparisons of *S*-*Q* relationships at intra-annual scales in watersheds across the hydroclimatic spectrum, further limiting our ability to identify generalizable hydrologic processes. Here, we analyzed event, seasonal and annual water balances across four catchments to address this knowledge gap. Specifically, we chose catchments we expected to have the highest dependence on storage for runoff generation, such as catchments near the threshold between water and energy limitation, with seasonal, highly variable runoff. Below, we use these results to generate hypotheses for dominant controls on catchment *S* and *P* partitioning that can be investigated in future studies.

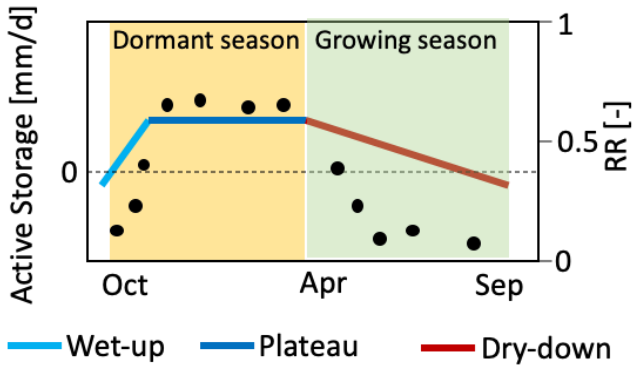

Figure 3.6. Conceptual model of stages of catchment storage. Runoff ratios are shown to be higher during the plateau, after storage is "full." Note that the timing of the dormant and growing season is for the Eastern US. The black dots represent runoff ratios.

3.5.1 Catchment Storage Drive Runoff Generation

Across the hydroclimatic spectrum considered in our study, event *RR*s exhibited a strong relationship with *S* (Figure 3.3. We used the *RR* metric to describe watershed runoff generation efficiency and observed that *S* adequately represents the underlying internal catchment functioning that drives runoff generation mechanisms (Hewlett and Hibbert, 1967). An explicit representation of the central effects of *S* occurred across the four catchments considered in this study, where higher *S* results in higher *RR* (Figure 3.4).

Intra-annual changes in *S* represent a kind of "watershed memory" (i.e., the influence of past *P* inputs) in seasonal runoff generation patterns (Aulenbach and Peters, 2018). There are few studies that explore event or monthly scale relationships between *RR*s and *S,* but these illuminate the significance of intra-annual *S* variability for runoff generation. For example, Nippgen *et al.* (2016) analyzed the lag correlation among monthly *P* and *RR*s in five watersheds in the southeastern US and determined that monthly *RR*s were most significantly correlated with the previous month's *P* and stayed strongly correlated up to a lag of six months. Others have explored *P* partitioning as a function of seasonality and catchment characteristics using theoretically derived and physically-based water balance models, suggesting that *RR* decreased with a decreasing wetness index (Yokoo *et al.*, 2008). Yokoo *et al.* (2008) also suggested that the consequences of seasonality are most significant when the seasonal variabilities of *P* and *ET* are out of phase, such as in Mediterranean climates (e.g., Tilden) and in arid systems. Other modeling approaches have used precipitation partitioning at monthly scales based on the Budyko framework (Wang *et al.*, 2011). Wang *et al.* (2011) showed that analyzing the water balance at monthly scales, accounting for *S* variability, has the potential for

understanding monthly, seasonal, and annual runoff generation. The work presented in the literature and our results highlight the role of watershed *S* in moderating *P* partitioning at intra-annual timescales that resulted in different runoff responses across the studied water years (Figure 3.3). Furthermore, our findings seem to be transferable across several regions in the hydroclimatic spectrum (Figure 3.3).

3.5.2 Conceptual Model of how Dominant Catchment States Drive Precipitation Partitioning

Here, we present a conceptual model that characterizes differences and similarities in storage-driven hydrologic partitioning, informed by observations of *P* partitioning in four catchments that span part of the hydroclimatic spectrum of water- to energy-limitation. We summarized the seasonality in *S* over a water year, focusing on catchments near the threshold of water/energy-limited hydroclimates, where storage is depleted and recharged each water year (Figure 3.6). Based on daily water balance observations and the general shape of catchment storage, we divided *S* into three dominant stages across a given water year: wet-up, plateau, and dry-down. From the three *S* stages, we identified the wet-up and the dry-down as transitional stages toward or from the plateau, respectively (Figure 3.3).

Wet-up

The onset of the wet-up stage occurs at the beginning of the water year when *S* is at a minimum, and continues until *S* fills up. Because *S* starts low, *P* is mostly partitioned towards *S* (e.g., Zehe *et al.*, 2005; Tromp-van Meerveld and McDonnell, 2006). That is, *S*

"fills up" during this wet-up, and minimum contributions to *Q* are observed (Figures 3 and 4). Because most of the wet-up stage coincides with the dormant season, *ET* is relatively low (Hay and Irmak, 2009; Evers *et al.*, 2021) and changes to catchment *S* are predominantly influenced by *P* inputs and *Q* outputs.

Plateau

Once *S* peaks, we transition to the plateau stage in the wet dormant season (Figure 3.6). During the plateau, we observe that *P* is predominantly partitioned to *Q* because, at this point, *S* capacity has likely been reached (Camporese *et al.*, 2019). This is analogous to a full bucket (Dralle *et al.*, 2018), which represents saturation of catchment *S*, and creates the conditions for the most dynamic period of runoff generation, with faster and higher magnitude stream responses to *P* inputs, as evidenced by relatively larger *RR*s (Figure 3.3). The runoff responses during the plateau suggest hydrological connectivity that favors water transfer as *Q* towards the catchment outlet (Soulsby *et al.*, 2015).

The plateau stage contrasts with the beginning and end of the wet-up and dry-down, respectively, where watershed storage is likely near the wilting point. The plateau stage is likely more common or sustained for longer in energy-limited catchments (Figure 3.3). This may be because *P* is frequent and significant enough to exceed water demands, allowing *S* to fill up (e.g., wet water year in Luquillo, Figure 3.3). In water-limited catchments (e.g., Tilden), we observed that during normal water years, no plateau is accomplished. However, a plateau stage can occur during wet water years (Figure 3.3). This suggests that the plateau stage is driven by *P* magnitudes, where individual

catchments likely have a *S* threshold that must be reached to hit the plateau stage. This difference in behavior in wet and normal water years during the plateau provides future research opportunities, such as incorporating additional catchments near the water-/energy-limitation threshold and including more extended time series in these threshold landscapes. Through such analysis, we could test the hypothesis of a threshold-based plateau. We can improve our understanding of intra-annual S variability in systems near the threshold that transition between water- and energy-limited during dry and wet water years, respectively.

Dry-down

With the onset of the growing season and an increase in ET demand, we transition from the plateau to the dry-down stage of catchment *S* (Figure 3.6). During this time, *S* decreases as *Q* and *ET* continuously remove water from the system, faster than incoming *P* (Figure 3.4). These observations are supported by others; Meerveld *et al.* (2015) observed low *S* and stream responses in periods of high *ET* for a catchment in the subtropical southeastern US. In a continental-scale study across the contiguous US and Puerto Rico, Rossi *et al.* (2016) described how high *ET* could lower the soil moisture before *P* occurs, decreasing the relative role of antecedent *S* on runoff generation. While we see the dry-down stage in watersheds across the water-to-energy limitation gradient (Figure 3.3), we anticipate that different hydrologic budget components drive *S* dynamics during this stage in different hydroclimates. In energy-limited landscapes, the dry-down stage is likely controlled by seasonality in *ET* (Maeda *et al.*, 2017; Gnann *et al.*, 2020), as these systems are often recognized to have limited seasonality in *P* (i.e., *P* continues to occur throughout the growing season). However, in water-limited landscapes, the dry-

down is likely controlled by seasonality in both *P* and *ET* (Cramer and Hoffman, 2015; Feng *et al.*, 2019). For example, in catchments with Mediterranean climates, such as Tilden, the water balance during the dry-down is dominated by *ET* and *Q*, as *P* events are uncommon during this stage. The asynchrony between *P* and *ET* (Feng *et al.*, 2019) in these types of landscapes leads to a more marked dry-down stage, which differs from the above-described controlling mechanisms for energy-limited landscapes. The dry-down stage ends once the system transitions into the wet up stage.

This conceptual framework for categorizing S behavior in catchments is consistent with other studies. For example, Fovet *et al.* (2015) used hysteresis analysis of daily *S* and *Q* in a maritime watershed in northwest France and described four distinctive periods in which the *S*-*Q* relationship highlighted different hydrologic processes. First, they noticed that P was partitioned towards S at the end of the dry periods. Second, Fovet *et al.* (2015) observed a wetting period, which resulted in *S* saturation in the riparian aquifer, allowing for more *S* supply to *Q* while hillslope *S* continued to be filled. This was followed by a period in which hillslope *S* was filled and started contributing to *Q*. Lastly, they described a period in which *P* declined, riparian *S* decreased, and Q was sustained by hillslope *S*. Interestingly, Fovet *et al.* (2015) did not consider the role of *ET* in their characterization of the different periods. The *S*-*Q* relationship presented by Fovet *et al.* (2015) was also proposed by Spence *et al.* (2010) for a large watershed in the Canadian shield. Both studies showed the critical role of *S* for runoff generation and highlighted the importance of intra-annual variability, which we found when disaggregating the hysteresis pattern by the *S* stages (Figure 3.5). The conceptual model

of storage stages in the present study thus advances ideas proposed by Fovet *et al.* (2018) and Spence *et al.* (2010) by applying them across the water/energy gradient.

3.5.3 Seasonal precipitation partitioning controls hysteretic behavior of runoff

This study documents relatively higher *RR* in the wet-up than in the dry-down stage for a given *S* value for the threshold catchments (Tilden, Calhoun; Figure 3.5). This essential distinguishing characteristic of the *S* and *RR* relationship illustrates the complexity of *S* variability at threshold catchments that we do not observe in the energy-limited systems (Figure 3.5). For systems at the threshold of water-/energy-limitation, the same *S* amount is partitioned to *ET* or *Q* differently throughout the year, depending on the *S* stage (Figure 3.5), which directly impacts how much water contributes to the stream (i.e., the *RR*).

Two different catchment storage reservoirs, direct and indirect storage, have been described to explain the dynamic behaviors in the *S*-*Q* relationships of watersheds (Dralle *et al.*, 2018), which can result in the hysteretic behavior of these two components of the water balance. Direct storage is hydraulically connected to the stream, and it explains the direct relationship between *S* and *Q* (i.e., *Q* is explicitly sensitive to variations of direct storage). In a saturated porous media, direct storage is the amount of water stored above field capacity. On the other hand, indirect storage is not hydraulically connected to the stream, and equals the amount of water stored below field capacity. Thus, indirect storage can change in amount without directly affecting *Q* (Dralle *et al.*,

2018). The wet-up and dry-down *S* stages highlight the transition between two extremes of catchment storage. We can see the predominant influence of indirect storage in a landscape at the beginning of the wet-up (or at the end of the dry-down), while complete saturation at the maximum direct storage could dominate during the plateau. Further, the difference in *RR* during the wet-up and dry-down could be a reflection of the redistribution of water between direct and indirect storages as a consequence of plant uptake during the growing season.

The present study does not address the role of *ET* in the redistribution of water into different *S* reservoirs during the dry-down directly, but we suspect that *ET* magnitude may influence whether *P* gets distributed into indirect or direct storage. This, in turn, may help explain the hysteretic behavior of the *SS*-*RR* relationships observed at Tilden and Calhoun. We hypothesize redistribution of the incoming *P* during the dry-down stage into less hydraulically active but more plant-accessible storage zones (Dralle *et al.*, 2018). This is consistent with the findings of ecohydrological studies of recent years that highlight how vegetation can tap into storage pools without affecting streamflow (Sprenger *et al.*, 2016; Evaristo and McDonnell, 2017; Chang *et al.*, 2019; Nehemy *et al.*, 2021). Moreover, it has been documented in the literature that plants can remove significant water volumes stored in saprolite and rock moisture (Rempe and Dietrich, 2018; Hahm *et al.*, 2019; McCormick *et al.*, 2021) which are commonly underappreciated parts of catchment storage, and that do not necessarily contribute directly to *Q*.

Even though the ecohydrology community has continued to improve collective knowledge on vegetation water use (e.g., Dawson and Ehleringer, 1991; Meißner *et al.*, 2014; McLaughlin *et al.*, 2017; Penna *et al.*, 2018; Li *et al.*, 2019; Oerter *et al.*, 2019), the

mechanisms that explain where vegetation access water are poorly known. For example, Volkmann *et al.* (2016) showed that different vegetation types growing in the same area used water from different depths. Similarly, Allen *et al.* (2019) showed that plant species in the same environment favored the use of water with different seasonal origins. With our analysis, we cannot assess the mechanisms by which plants access water in the watersheds studied. However, by showing the disparate *P* partitioning during the dry-down stage relative to the wet-up stage of catchment storage, the relatively simple analysis of the water balance in the present study highlights the necessity for understanding *ET* (especially transpiration) when modeling the terrestrial water budget (Jasechko *et al.*, 2013; Schlesinger and Jasechko, 2014).

The replenishment of these vegetation-preferred storage pools is relatively unexplored. How these stores are receive inflow during the wet-up stage may help to explain *S*-*RR* hysteresis (Figure 3.5), which highlights the effects of intra-annual *S* variations for runoff generation in catchments at the threshold. Using storage stages as a framework to separate periods of the water year with distinct hydrologic partitioning characteristics, we may be able to further enhance our understanding of the relative importance of *ET* as a controlling parameter in S-RR relationships in watersheds.

3.6 Implications and Conclusion

This study elucidates the intra-annual variability in runoff generation in response to changes in *S* in watersheds that exist over a range of hydroclimatic conditions. Our analysis sought to improve our conceptual understanding of the diversity of catchment behavior within long-term annual water balance classifications. We observed a

characteristic shape in daily storage across water years in watersheds at the water-/energy-limitation threshold, where systems experienced distinct runoff response across wet-up, plateau, and dry-down *S* stages.

The similarity in intra-annual *S* variability between the two threshold catchments, notwithstanding their different hydroclimatic zones and long-term positions on opposite sides of the threshold, suggests a characteristic behavior of catchments close to this threshold. This similitude indicates that for catchments such as Calhoun and Tilden, significant intra-annual changes in *S* induce marked shifts in runoff generation behavior that are characteristic of both humid and arid catchments (i.e., intra-annual switch between water- and energy-limited).

The semi-arid watershed (Tilden) shifted between energy-limited and water-limited for the wet and normal water years. This variability led to differences in the degree or presence of *S* stages that occurred during each individual water year. In a normal water year, Tilden displayed only a wet-up and dry-down stage, as water demands were insufficient to achieve the plateau. However, this catchment displayed the three *S* stages during the wet water year. In the humid Calhoun, we observed the three *S* stages for both water years, highlighting this system's position at the threshold of water-/energy-limited hydroclimates, where storage is depleted and recharged each water year. However, separating the annual hydroclimatic conditions by events (and monthly) at Calhoun showcased how this system switches from water-limited to energy-limited within the year, which is otherwise masked in aggregated annual averages (Figure 3.3).

Efforts to quantify or characterize hydroclimatic seasonality in most energy-limited systems have been poorly considered until recent years (Nippgen *et al.*, 2016). This is probably due to the relatively uniform and more considerable *P* that these systems receive. For example, the average monthly *P* in Calhoun was ~100 mm for every month during this study (Figure 3.2), which may indicate a lack of intra-annual variability. However, seasonality in *ET* due to the growing season led to marked seasonality in *S* and Calhoun displayed the three S stages. We expected *P* to drive seasonal patterns in *S* across the hydroclimatic spectrum. However, the plateau stage predominated in the maritime and tropical catchments, with only minor periods of dry-down. Perhaps, in these highly energy-limited landscapes, year-to-year variability in *P* might be more critical for the *S* stages than intra-annual variability in *P* (e.g., if the previous year was very dry, then we might observe a wet-up). Undoubtedly, the Mediterranean hydroclimate of Tilden produces stronger seasonality in *S* than the rest of the landscapes in our study (Feng *et al.*, 2019). However, given the evident seasonality in *ET*, it is unclear why little attention has been dedicated to understanding changes in intra-annual *S* dynamics in catchments at the threshold (e.g., Calhoun). In showing the marked seasonality of *S* in catchments at the threshold of water-/energy-limited hydroclimates, our work highlights a research area that requires more attention (e.g., Figure 3.5).

Categorizing watersheds as energy- or water-limited based on long-term annual water balances has been a fundamental approach for explaining variability in runoff generation across landscapes with various hydroclimatic conditions. However, annual water balance studies may "miss" the intra-annual variability in runoff generation, which

may obscure the differences and similarities between water- and energy-limited catchments, especially in landscapes with long-term hydrology that places them close to the threshold between water- and energy-limitation. We present a framework for comparing *S*-*RR* at intra-annual scales in catchments across the hydroclimatic spectrum that display different *S* stages across the water year. Our *S* stage framework can be used as a unifying concept to make more robust cross-catchment comparisons that include the nonstationarity of hydroclimates. Improving our knowledge of the *P* partitioning in catchments at the threshold of water-/energy-limited hydroclimates might arise from explaining these catchments' water balance components and multi-scale hydrologic controls (e.g., *S*, *RR*) rather than using the Budyko space.

3.7 Acknowledgement

This work was developed in collaboration with Dr. John Mallard. We would like to express our deepest gratitude to him for the many hours that we spent discussing this manuscript. The data from Calhoun was supported by the NSF, grant number EAR-1331846.The authors sincerely thank the East Bay Regional Park District, particularly Pamela Beitz for the support in collecting the Tilden data. Thanks also to the Center for Ecology and Hydrology, U.K, Ciaran Harman, and James Kirchner for creating and QA/QC the dataset from Lower Hafren. We would also like to thank the Luquillo CZO, particularly Miguel Leon for the precipitation data available at hydroshare (citation in text), and Jess Zimmerman for the meteorological data from El Verde Field Station, available through the EDI data portal (citation in text). EG was partially funded by a

Cota-Robles fellowship through the University of California Santa Cruz, and by a Margaret A. Davidson fellowship (NA20NOS4200122).

Bibliography

Abarca E, Karam H, Hemond HF, Harvey CF. 2013. Transient groundwater dynamics in a coastal aquifer: The effects of tides, the lunar cycle, and the beach profile. *Water Resources Research* **49** (5): 2473–2488 DOI: 10.1002/wrcr.20075

Addison PS. 2005. Wavelet transforms and the ECG: a review. *Physiological Measurement* **26** (5): R155-199 DOI: 10.1088/0967-3334/26/5/R01

Addy K, Gold A, Nowicki B, McKenna J, Stolt M, Groffman P. 2005. Denitrification capacity in a subterranean estuary below a Rhode Island fringing salt marsh. *Estuaries* **28** (6): 896–908 DOI: 10.1007/BF02696018

Adema EB, Grootjans AP. 2003. Possible positive-feedback mechanisms: plants change abiotic soil parameters in wet calcareous dune slacks. *Plant Ecology* **167** (1): 141–149 DOI: 10.1023/A:1023947411605

Aguilera R, Melack JM. 2018. Concentration-Discharge Responses to Storm Events in Coastal California Watersheds: C-Q STORM RESPONSES COASTAL CALIFORNIA. *Water Resources Research* **54** (1): 407–424 DOI: 10.1002/2017WR021578

Alexander AC, Levenstein B, Sanderson LA, Blukacz-Richards EA, Chambers PA. 2020. How does climate variability affect water quality dynamics in Canada's oil sands region? *Science of The Total Environment* **732**: 139062 DOI: 10.1016/j.scitotenv.2020.139062

Allen R, Pereira L, Raes D, Smith M. 1998. Crop evapotranspiration-Guidelines for computing crop water requirements, FAO

Allen ST, Kirchner JW, Braun S, Siegwolf RTW, Goldsmith GR. 2019. Seasonal origins of soil water used by trees. *Hydrology and Earth System Sciences* **23** (2): 1199–1210 DOI: 10.5194/hess-23-1199-2019

Almaraz M, Wong MY, Yang WH. 2020. Looking back to look ahead: a vision for soil denitrification research. *Ecology* **101** (1): e02917 DOI: https://doi.org/10.1002/ecy.2917

Andrea B, Francesc G, Jérôme L, Eusebi V, Francesc S. 2006. Cross-site Comparison of Variability of DOC and Nitrate c–q Hysteresis during the Autumn–winter Period in Three Mediterranean Headwater Streams: A Synthetic Approach. *Biogeochemistry* **77** (3): 327–349 DOI: 10.1007/s10533-005-0711-7

Arora B, Burrus M, Newcomer M, Steefel CI, Carroll RWH, Dwivedi D, Dong W, Williams KH, Hubbard SS. 2020. Differential C-Q Analysis: A New Approach to Inferring Lateral Transport and Hydrologic Transients Within Multiple Reaches of a Mountainous Headwater Catchment. *Frontiers in Water* **2** Available at: https://www.frontiersin.org/article/10.3389/frwa.2020.00024 [Accessed 9 April 2022]

Arora B, Dwivedi D, Hubbard SS, Steefel CI, Williams KH. 2016. Identifying geochemical hot moments and their controls on a contaminated river floodplain system using wavelet and entropy approaches. *Environmental Modelling & Software* **85**: 27–41 DOI: 10.1016/j.envsoft.2016.08.005

Arora B, Mohanty BP, McGuire JT, Cozzarelli IM. 2013. Temporal dynamics of biogeochemical processes at the Norman Landfill site: Temporal Dynamics at

the Norman Landfill Site. *Water Resources Research* **49** (10): 6909–6926 DOI: 10.1002/wrcr.20484

Aulenbach BT, Peters NE. 2018. Quantifying Climate-Related Interactions in Shallow and Deep Storage and Evapotranspiration in a Forested, Seasonally Water-Limited Watershed in the Southeastern United States. *Water Resources Research* **54** (4): 3037–3061 DOI: 10.1002/2017WR020964

Beecham S, Chowdhury RK. 2010. Temporal characteristics and variability of point rainfall: a statistical and wavelet analysis. *International Journal of Climatology* **30** (3): 458–473 DOI: 10.1002/joc.1901

Beheshti K, Endris C, Goodwin P, Pavlak A, Wasson K. 2022. Burrowing crabs and physical factors hasten marsh recovery at panne edges. *PLOS ONE* **17** (1): e0249330 DOI: 10.1371/journal.pone.0249330

Beheshti KM, Wasson K, Angelini C, Silliman BR, Hughes BB. 2021. Long-term study reveals top-down effect of crabs on a California salt marsh. *Ecosphere* **12** (8): e03703 DOI: 10.1002/ecs2.3703

Bieroza MZ, Heathwaite AL. 2015. Seasonal variation in phosphorus concentration–discharge hysteresis inferred from high-frequency in situ monitoring. *Journal of Hydrology* **524**: 333–347 DOI: 10.1016/j.jhydrol.2015.02.036

Birgand F, Aveni-Deforge K, Smith B, Maxwell B, Horstman M, Gerling AB, Carey CC. 2016. First report of a novel multiplexer pumping system coupled to a water quality probe to collect high temporal frequency in situ water chemistry measurements at multiple sites: High-Resolution Water Chemistry in Time and

Space. *Limnology and Oceanography: Methods* **14** (12): 767–783 DOI: 10.1002/lom3.10122

Bledsoe RB, Bean EZ, Austin SS, Peralta AL. 2020. A microbial perspective on balancing trade-offs in ecosystem functions in a constructed stormwater wetland. *Ecological Engineering* **158**: 106000 DOI: 10.1016/j.ecoleng.2020.106000

Blum LK, Christian RR, Cahoon DR, Wiberg PL. 2021. Processes Influencing Marsh Elevation Change in Low- and High-Elevation Zones of a Temperate Salt Marsh. *Estuaries and Coasts* **44** (3): 818–833 DOI: 10.1007/s12237-020-00796-z

Blume T, Zehe E, Bronstert A. 2007. Rainfall—runoff response, event-based runoff coefficients and hydrograph separation. *Hydrological Sciences Journal* **52** (5): 843–862 DOI: 10.1623/hysj.52.5.843

Bowen JL, Giblin AE, Murphy AE, Bulseco AN, Deegan LA, Johnson DS, Nelson JA, Mozdzer TJ, Sullivan HL. 2020. Not All Nitrogen Is Created Equal: Differential Effects of Nitrate and Ammonium Enrichment in Coastal Wetlands. *BioScience* **70** (12): 1108–1119 DOI: 10.1093/biosci/biaa140

Boyd CE. 2000. Dissolved Oxygen and Redox Potential. In *Water Quality: An Introduction*, Boyd CE (ed.).Springer US: Boston, MA; 69–94. DOI: 10.1007/978-1-4615-4485-2_5

Breier JA, Nidzieko N, Monismith S, Moore W, Paytan A. 2009. Tidally regulated chemical fluxes across the sediment—water interface in Elkhorn Slough, California: Evidence from a coupled geochemical and hydrodynamic approach. *Limnology and Oceanography* **54** (6): 1964–1980 DOI: https://doi.org/10.4319/lo.2009.54.6.1964

Breslow N. 1970. A Generalized Kruskal-Wallis Test for Comparing K Samples Subject to Unequal Patterns of Censorship. *Biometrika* **57** (3): 579–594 DOI: 10.2307/2334776

Broenkow WW, Breaker LC. 2019. A 30-Year History of the Tides and Currents in Elkhorn Slough, California. *Estuaries and Coastal Zones - Dynamics and Response to Environmental Changes* DOI: 10.5772/intechopen.88671

Brunel H, Gallardo-Chacón J-J, Buil A, Vallverdú M, Soria JM, Caminal P, Perera A. 2010. MISS: a non-linear methodology based on mutual information for genetic association studies in both population and sib-pairs analysis. *Bioinformatics* **26** (15): 1811–1818 DOI: 10.1093/bioinformatics/btq273

Budyko MI. 1974. *Climate and Life*. Academic Press: New York.

Buffington KJ, Janousek CN, Dugger BD, Callaway JC, Schile-Beers LM, Sloane EB, Thorne KM. 2021. Incorporation of uncertainty to improve projections of tidal wetland elevation and carbon accumulation with sea-level rise. *PLOS ONE* **16** (10): e0256707 DOI: 10.1371/journal.pone.0256707

Bulseco AN, Giblin AE, Tucker J, Murphy AE, Sanderman J, Hiller-Bittrolff K, Bowen JL. 2019. Nitrate addition stimulates microbial decomposition of organic matter in salt marsh sediments. *Global Change Biology*: gcb.14726 DOI: 10.1111/gcb.14726

Burke DJ, Hamerlynck EP, Hahn D. 2002. Interactions among Plant Species and Microorganisms in Salt Marsh Sediments. *Applied and Environmental Microbiology* **68** (3): 1157–1164 DOI: 10.1128/AEM.68.3.1157-1164.2002

Buss HL, Brantley SL, Scatena FN, Bazilievskaya EA, Blum A, Schulz M, Jiménez R, White AF, Rother G, Cole D. 2013. Probing the deep critical zone beneath the Luquillo Experimental Forest, Puerto Rico. *Earth Surface Processes and Landforms* **38** (10): 1170–1186 DOI: 10.1002/esp.3409

Caetano M, Bernárdez P, Santos-Echeandia J, Prego R, Vale C. 2012. Tidally driven N, P, Fe and Mn exchanges in salt marsh sediments of Tagus estuary (SW Europe). *Environmental Monitoring and Assessment* **184** (11): 6541–6552 DOI: 10.1007/s10661-011-2439-2

Caffrey JM. 2002. Chapter 3: Climate. In *Changes in a California Estuary: An Ecosystem Profile of Elkhorn Slough*, Caffrey JM, , Brown M, , Tyler B, , Silberstain M (eds).Elkhorn Slough Fundation: Moss Landing, California; 25–28. Available at: http://library.elkhornslough.org/attachments/Caffrey_2002_Changes_In_A_California.pdf [Accessed 20 March 2022]

Caffrey JM, Broenkow W. 2002. Chapter 4: Hydrography. In *Changes in a California Estuary: An Ecosystem Profile of Elkhorn Slough*, Caffrey JM, , Brown M, , Tyler B, , Silberstain M (eds).Elkhorn Slough Fundation: Moss Landing, California; 29–42. Available at: http://library.elkhornslough.org/attachments/Caffrey_2002_Changes_In_A_California.pdf [Accessed 20 March 2022]

Caffrey JM, Harrington N, Ward B. 2002. Biogeochemical processes in a small California estuary. 1. Benthic fluxes and pore water constituents reflect high nutrient freshwater inputs. *Marine Ecology Progress Series* **233**: 39–53 DOI: 10.3354/meps233039

California Actual Evapotranspiration (CalETa) Mapping Program.

California Data Exchange Center - Query Tools. Available at: https://cdec.water.ca.gov/ [Accessed 9 May 2019]

Camporese M, Paniconi C, Putti M, McDonnell JJ. 2019. Fill and Spill Hillslope Runoff Representation With a Richards Equation-Based Model. *Water Resources Research* **55** (11): 8445–8462 DOI: 10.1029/2019WR025726

Chanat JG, Rice KC, Hornberger GM. 2002a. Consistency of patterns in concentration-discharge plots: PATTERNS IN CONCENTRATION-DISCHARGE PLOTS. *Water Resources Research* **38** (8): 22-1-22–10 DOI: 10.1029/2001WR000971

Chanat JG, Rice KC, Hornberger GM. 2002b. Consistency of patterns in concentration-discharge plots. *Water Resources Research* **38** (8): 22-1-22–10 DOI: 10.1029/2001WR000971

Chang E, Li P, Li Z, Xiao L, Zhao B, Su Y, Feng Z. 2019. Using water isotopes to analyze water uptake during vegetation succession on abandoned cropland on the Loess Plateau, China. *CATENA* **181**: 104095 DOI: 10.1016/j.catena.2019.104095

Chapin TP, Caffrey JM, Jannasch HW, Coletti LJ, Haskins JC, Johnson KS. 2004. Nitrate sources and sinks in Elkhorn Slough, California: Results from long-term continuous in situ nitrate analyzers. *Estuaries* **27** (5): 882–894 DOI: 10.1007/BF02912049

Contra Costa Soil Survey. 1981.

Cover TM, Thomas JA. 2006. *ELEMENTS OF INFORMATION THEORY*. Wiley-Interscience: Hoboken, N.J.

Cramer MD, Hoffman MT. 2015. The Consequences of Precipitation Seasonality for Mediterranean-Ecosystem Vegetation of South Africa. *PLOS ONE* **10** (12): e0144512 DOI: 10.1371/journal.pone.0144512

Crotty SM, Ortals C, Pettengill TM, Shi L, Olabarrieta M, Joyce MA, Altieri AH, Morrison E, Bianchi TS, Craft C, et al. 2020. Sea-level rise and the emergence of a keystone grazer alter the geomorphic evolution and ecology of southeast US salt marshes. *Proceedings of the National Academy of Sciences* **117** (30): 17891–17902 DOI: 10.1073/pnas.1917869117

Daubechies I. 1992. *Ten Lectures on Wavelets*. Society for Industrial and Applied Mathematics. DOI: 10.1137/1.9781611970104

Davies JAC, Beven K. 2015. Hysteresis and scale in catchment storage, flow and transport. *Hydrological Processes* **29** (16): 3604–3615 DOI: 10.1002/hyp.10511

Dawson TE, Ehleringer JR. 1991. Streamside trees that do not use stream water. *Nature* **350** (6316): 335–337 DOI: 10.1038/350335a0

Detty JM, McGuire KJ. 2010. Topographic controls on shallow groundwater dynamics: implications of hydrologic connectivity between hillslopes and riparian zones in a till mantled catchment. *Hydrological Processes* **24** (16): 2222–2236 DOI: 10.1002/hyp.7656

Devol AH. 2015. Denitrification, Anammox, and N2 Production in Marine Sediments. *Annual Review of Marine Science* **7** (1): 403–423 DOI: 10.1146/annurev-marine-010213-135040

Dralle DN, Hahm WJ, Rempe DM, Karst NJ, Thompson SE, Dietrich WE. 2018. Quantification of the seasonal hillslope water storage that does not drive

streamflow: Catchment storage that does not drive streamflow. *Hydrological Processes* **32** (13): 1978–1992 DOI: 10.1002/hyp.11627

Ensign SH, Piehler MF, Doyle MW. 2008. Riparian zone denitrification affects nitrogen flux through a tidal freshwater river. *Biogeochemistry* **91** (2): 133–150 DOI: 10.1007/s10533-008-9265-9

Etheridge JR, Birgand F, Osborne JA, Osburn CL, Burchell MR, Irving J. 2014. Using in situ ultraviolet-visual spectroscopy to measure nitrogen, carbon, phosphorus, and suspended solids concentrations at a high frequency in a brackish tidal marsh: In situ spectroscopy to monitor N, C, P, TSS. *Limnology and Oceanography: Methods* **12** (1): 10–22 DOI: 10.4319/lom.2014.12.10

Evaristo J, McDonnell JJ. 2017. Prevalence and magnitude of groundwater use by vegetation: a global stable isotope meta-analysis. *Scientific Reports* **7** (1): 44110 DOI: 10.1038/srep44110

Evers SM, Knight TM, Inouye DW, Miller TEX, Salguero-Gómez R, Iler AM, Compagnoni A. 2021. Lagged and dormant season climate better predict plant vital rates than climate during the growing season. *Global Change Biology* **27** (9): 1927–1941 DOI: 10.1111/gcb.15519

Falkowski PG, Fenchel T, Delong EF. 2008. The Microbial Engines That Drive Earth's Biogeochemical Cycles. *Science* **320** (5879): 1034–1039 DOI: 10.1126/science.1153213

Fan C, Zhang D, Zhang C-H. 2011. On sample size of the kruskal-wallis test with application to a mouse peritoneal cavity study. *Biometrics* **67** (1): 213–224 DOI: 10.1111/j.1541-0420.2010.01407.x

Feng X, Thompson SE, Woods R, Porporato A. 2019. Quantifying Asynchronicity of Precipitation and Potential Evapotranspiration in Mediterranean Climates. *Geophysical Research Letters* **46** (24): 14692–14701 DOI: 10.1029/2019GL085653

Fine RA, Millero FJ. 1973. Compressibility of water as a function of temperature and pressure. *The Journal of Chemical Physics* **59** (10): 5529–5536 DOI: 10.1063/1.1679903

Foufoula-Georgiou E, Kumar P. 1994. Wavelet Analysis in Geophysics: An Introduction. In *Wavelet Analysis and Its Applications*, Foufoula-Georgiou E, , Kumar P (eds).Academic Press; 1–43. DOI: 10.1016/B978-0-08-052087-2.50007-4

Fovet O, Ruiz L, Hrachowitz M, Faucheux M, Gascuel-Odoux C. 2015. Hydrological hysteresis and its value for assessing process consistency in catchment conceptual models. *Hydrology and Earth System Sciences* **19** (1): 105–123 DOI: 10.5194/hess-19-105-2015

Fox J, Weisberg S. 2019. *An R Companion to Applied Regression*. Sage: Thousand Oaks, CA\. Available at: https://socialsciences.mcmaster.ca/jfox/Books/Companion/

Fuka D, Walter M, Archibald D, Steenhuis T, Easton Z. 2018. *EcoHydRology*.

Garcia ES, Tague CL. 2015. Soil storage influences climate–evapotranspiration interactions in three western United States catchments. *Hydrology and Earth System Sciences Discussions* **12** (8): 7893–7931 DOI: 10.5194/hessd-12-7893-2015

Gastwirth JL, Gel YR, Miao W. 2009. The Impact of Levene's Test of Equality of Variances on Statistical Theory and Practice. *Statistical Science* **24** (3): 343–360 DOI: 10.1214/09-STS301

Giblin A, Tobias C, Song B, Weston N, Banta G, Rivera-Monroy V. 2013. The Importance of Dissimilatory Nitrate Reduction to Ammonium (DNRA) in the Nitrogen Cycle of Coastal Ecosystems. *Oceanography* **26** (3): 124–131 DOI: 10.5670/oceanog.2013.54

Gnann SJ, Howden NJK, Woods RA. 2020. Hydrological signatures describing the translation of climate seasonality into streamflow seasonality. *Hydrology and Earth System Sciences* **24** (2): 561–580 DOI: 10.5194/hess-24-561-2020

Gouhier T, Grinsted A, Simko V. 2021. Biwavelet. Available at: https://cran.r-project.org/web/packages/biwavelet/biwavelet.pdf [Accessed 2 August 2021]

Grande E, Arora B, Visser A, Montalvo M, Braswell A, Seybold E, Tatariw C, Beheshti K, Zimmer M. 2022. Tidal frequencies and quasiperiodic subsurface water level variations dominate redox dynamics in a salt marsh system. *Hydrological Processes* **36** (5): 1–16 DOI: 10.1002/hyp.14587

Grande E, Visser A, Beitz P, Moran J. 2019. Examination of Nutrient Sources and Transport in a Catchment with an Audubon Certified Golf Course. *Water* **11** (9): 1923 DOI: 10.3390/w11091923

Grande E, Visser A, Moran JE. 2020. Catchment storage and residence time in a periodically irrigated watershed. *Hydrological Processes* **34** (14): 1–17 DOI: 10.1002/hyp.13798

Graymer RW. 2000. Geologic Map and Map Database of the Oakland Metropolitan Area, Alameda, Contra Costa, and San Francisco Counties, California

Grinsted A, Moore JC, Jevrejeva S. 2004. Application of the cross wavelet transform and wavelet coherence to geophysical time series. *Nonlinear Processes in Geophysics* **11** (5/6): 561–566 DOI: https://doi.org/10.5194/npg-11-561-2004

Guan K, Thompson SE, Harman CJ, Basu NB, Rao PSC, Sivapalan M, Packman AI, Kalita PK. 2011. Spatiotemporal scaling of hydrological and agrochemical export dynamics in a tile-drained Midwestern watershed. *Water Resources Research* **47** (10) DOI: 10.1029/2010WR009997

Guimond J, Tamborski J. 2021. Salt Marsh Hydrogeology: A Review. *Water* **13** (4): 543 DOI: 10.3390/w13040543

Guimond JA, Seyfferth AL, Moffett KB, Michael HA. 2020a. A physical-biogeochemical mechanism for negative feedback between marsh crabs and carbon storage. *Environmental Research Letters* **15** (3): 034024 DOI: 10.1088/1748-9326/ab60e2

Guimond JA, Yu X, Seyfferth AL, Michael HA. 2020b. Using Hydrological-Biogeochemical Linkages to Elucidate Carbon Dynamics in Coastal Marshes Subject to Relative Sea Level Rise. *Water Resources Research* **56** (2): e2019WR026302 DOI: https://doi.org/10.1029/2019WR026302

Haavisto VF. 1974. Effects of a heavy rainfall on redox potential and acidity of a waterlogged peat. *Canadian Journal of Soil Science* **54** (2): 133–135 DOI: 10.4141/cjss74-019

Haberer CM, Cirpka OA, Rolle M, Grathwohl P. 2014. Experimental Sensitivity Analysis of Oxygen Transfer in the Capillary Fringe. *Groundwater* **52** (1): 37–49 DOI: 10.1111/gwat.12028

Hahm WJ, Rempe DM, Dralle DN, Dawson TE, Lovill SM, Bryk AB, Bish DL, Schieber J, Dietrich WE. 2019. Lithologically Controlled Subsurface Critical Zone Thickness and Water Storage Capacity Determine Regional Plant Community Composition. *Water Resources Research* **55** (4): 3028–3055 DOI: 10.1029/2018WR023760

Hailegeorgis TT, Alfredsen K, Abdella YS, Kolberg S. 2016. Evaluation of storage–discharge relationships and recession analysis-based distributed hourly runoff simulation in large-scale, mountainous and snow-influenced catchment. *Hydrological Sciences Journal* **61** (16): 2872–2886 DOI: 10.1080/02626667.2016.1170939

Hamersley MR, Howes BL. 2005. Coupled nitrification–denitrification measured in situ in a Spartina alterniflora marsh with a 15NH4+ tracer. *Marine Ecology Progress Series* **299**: 123–135 DOI: 10.3354/meps299123

Hammer DA, Bastian RK. 1989. Wetlands Ecosystems: Natural Water Purifiers? In *Constructed Wetlands for Wastewater Treatment*CRC Press.

Hariprasath S, Mohan V. 2008. Biometric personal identification based on iris recognition using complex wavelet transforms. In *2008 International Conference on Computing, Communication and Networking*1–5. DOI: 10.1109/ICCCNET.2008.4787736

Harman CJ. 2015. Time-variable transit time distributions and transport: Theory and application to storage-dependent transport of chloride in a watershed. *Water Resources Research* **51** (1): 1–30 DOI: 10.1002/2014WR015707

Hay CH, Irmak S. 2009. Actual and Reference Evaporative Losses and Surface Coefficients of a Maize Field during Nongrowing (Dormant) Periods. *Journal of Irrigation and Drainage Engineering* **135** (3): 313–322 DOI: 10.1061/(ASCE)IR.1943-4774.0000001

Henderson RD, Day-Lewis FD, Lane JW, Harvey CF, Liu L. 2008. Characterizing Submarine Groundwater Discharge Using Fiber-Optic Distributed Temperature Sensing and Marine Electrical Resistivity. In *Symposium on the Application of Geophysics to Engineering and Environmental Problems 2008*Environment and Engineering Geophysical Society; 775–785. DOI: 10.4133/1.2963319

Hewlett JD, Hibbert AR. 1967. Factors affecting the response of small watersheds to precipitation in humid areas. *Forest hydrology* **33**: 275–290

Hicks K, Jeppesen R, Haskins J, Wasson K. 2019. Long-term trends and spatial patterns of water quality in estuarine wetlands of central California. Elkhorn Slough Technical Report Series. Scientific Report 2019:1. Elkohrn Slough NERR, Moss Landing, California. Available at: http://library.elkhornslough.org/research/bibliography/Hicks_2019_Long-term_trends_and_spatial.pdf [Accessed 11 April 2022]

Jasechko S, Sharp ZD, Gibson JJ, Birks SJ, Yi Y, Fawcett PJ. 2013. Terrestrial water fluxes dominated by transpiration. *Nature* **496** (7445): 347–350 DOI: 10.1038/nature11983

Jeppesen R, Rodriguez M, Rinde J, Haskins J, Hughes B, Mehner L, Wasson K. 2018. Effects of Hypoxia on Fish Survival and Oyster Growth in a Highly Eutrophic Estuary. *Estuaries and Coasts* **41** (1): 89–98 DOI: 10.1007/s12237-016-0169-y

Johnson DS, Warren RS, Deegan LA, Mozdzer TJ. 2016. Saltmarsh plant responses to eutrophication. *Ecological Applications* **26** (8): 2649–2661 DOI: 10.1002/eap.1402

Jones JA, Creed IF, Hatcher KL, Warren RJ, Adams MB, Benson MH, Boose E, Brown WA, Campbell JL, Covich A, et al. 2012. Ecosystem Processes and Human Influences Regulate Streamflow Response to Climate Change at Long-Term Ecological Research Sites. *BioScience* **62** (4): 390–404 DOI: 10.1525/bio.2012.62.4.10

Joye SB, Hollibaugh JT. 1995. Influence of Sulfide Inhibition of Nitrification on Nitrogen Regeneration in Sediments. *Science* **270** (5236): 623–625

Kantelhardt JW, Rybski D, Zschiegner SA, Braun P, Koscielny-Bunde E, Livina V, Havlin S, Bunde A. 2003. Multifractality of river runoff and precipitation: comparison of fluctuation analysis and wavelet methods. *Physica A: Statistical Mechanics and its Applications* **330** (1): 240–245 DOI: 10.1016/j.physa.2003.08.019

Kincaid DW, Seybold EC, Adair EC, Bowden WB, Perdrial JN, Vaughan MCH, Schroth AW. 2020. Land Use and Season Influence Event-Scale Nitrate and Soluble Reactive Phosphorus Exports and Export Stoichiometry from Headwater Catchments. *Water Resources Research* **56** (10): e2020WR027361 DOI: https://doi.org/10.1029/2020WR027361

Koop-Jakobsen K, Giblin AE. 2009. New approach for measruing denitrification in the rhizosphere. *Limnology and Oceanography: Methods* (7): 626–637

Koop-Jakobsen K, Giblin AE. 2010. The effect of increased nitrate loading on nitrate reduction via denitrification and DNRA in salt marsh sediments. *Limnology and Oceanography* **55** (2): 789–802 DOI: 10.4319/lo.2010.55.2.0789

Koop-Jakobsen K, Wenzhöfer F. 2015. The Dynamics of Plant-Mediated Sediment Oxygenation in Spartina anglica Rhizospheres—a Planar Optode Study. *Estuaries and Coasts* **38** (3): 951–963 DOI: 10.1007/s12237-014-9861-y

Krause JR, Watson EB, Wigand C, Maher N. 2020. Are Tidal Salt Marshes Exposed to Nutrient Pollution more Vulnerable to Sea Level Rise? *Wetlands* **40** (5): 1539–1548 DOI: 10.1007/s13157-019-01254-8

Kumar P, Foufoula-Georgiou E. 1997. Wavelet analysis for geophysical applications. *Reviews of Geophysics* **35** (4): 385–412 DOI: 10.1029/97RG00427

Kumar P, Dasgupta R, Johnson BA, Saraswat C, Basu M, Kefi M, Mishra BK. 2019. Effect of Land Use Changes on Water Quality in an Ephemeral Coastal Plain: Khambhat City, Gujarat, India. *Water* **11** (4): 724 DOI: 10.3390/w11040724

Kvålseth TO. 2017. On Normalized Mutual Information: Measure Derivations and Properties. *Entropy* **19** (11): 631 DOI: 10.3390/e19110631

Labat D, Ronchail J, Callede J, Guyot JL, Oliveira ED, Guimarães W. 2004. Wavelet analysis of Amazon hydrological regime variability. *Geophysical Research Letters* **31** (2) DOI: 10.1029/2003GL018741

Lahiri C, Davidson GR. 2020. Heterogeneous oxygenation of wetland soils with increasing inundation: Redox potential, water depth, and preferential flow paths. *Hydrological Processes*: hyp.13654 DOI: 10.1002/hyp.13654

Li H, Si B, Wu P, McDonnell JJ. 2019. Water mining from the deep critical zone by apple trees growing on loess. *Hydrological Processes* **33** (2): 320–327 DOI: 10.1002/hyp.13346

Liland KH, Mevik B, Wehrens R, Hiemstra P. 2021. pls: Partial Least Squares and Principal Component Regression. Available at: https://github.com/khliland/pls

Liu W, Birgand F, Tian S, Chen C. 2021. Event-scale hysteresis metrics to reveal processes and mechanisms controlling constituent export from watersheds: A review☆. *Water Research* **200**: 117254 DOI: 10.1016/j.watres.2021.117254

Liu W, Maxwell B, Birgand F, Youssef M, Chescheir G, Tian S. 2020a. Multipoint High-Frequency Sampling System to Gain Deeper Insights on the Fate of Nitrate in Artificially Drained Fields. *Journal of Irrigation and Drainage Engineering* **146** (1): 06019012 DOI: 10.1061/(ASCE)IR.1943-4774.0001438

Liu W, Youssef MA, Birgand FP, Chescheir GM, Tian S, Maxwell BM. 2020b. Processes and mechanisms controlling nitrate dynamics in an artificially drained field: Insights from high-frequency water quality measurements. *Agricultural Water Management* **232**: 106032 DOI: 10.1016/j.agwat.2020.106032

Lloyd CEM, Freer JE, Johnes PJ, Collins AL. 2016. Using hysteresis analysis of high-resolution water quality monitoring data, including uncertainty, to infer controls on nutrient and sediment transfer in catchments. *Science of The Total Environment* **543**: 388–404 DOI: 10.1016/j.scitotenv.2015.11.028

Maeda EE, Ma X, Wagner FH, Kim H, Oki T, Eamus D, Huete A. 2017. Evapotranspiration seasonality across the Amazon Basin. *Earth System Dynamics* **8** (2): 439–454 DOI: 10.5194/esd-8-439-2017

Mallard J. 2020. Hydrologic Functioning of Low-Relief, Deep Soil Watersheds and Hydrologic Legacies of Intensive Agriculture in the Calhoun Critical Zone Observatory, South Carolina, USA.Doctor od Philosophy, Duke University,

North Carolina, USA. Available at: https://dukespace.lib.duke.edu/dspace/bitstream/handle/10161/20983/Mallard_duke_0066D_15696.pdf?sequence=1 [Accessed 10 February 2021]

Mallat S. 1999. *A Wavelet Tour of Signal Processing: The Sparse Way (Wavelet Analysis & Its Applications).* Academic Press: Burlington, MA 01803, USA.

Malzone CM. 1999. Tidal scour and its relation to erosion and sediment transport in Elkhorn Slough.Master Thesis, San Jose State University, San Jose, California, United States.

Martínez B, Gilabert MA. 2009. Vegetation dynamics from NDVI time series analysis using the wavelet transform. *Remote Sensing of Environment* **113** (9): 1823–1842 DOI: 10.1016/j.rse.2009.04.016

McCarter CPR, Sebestyen SD, Eggert SL, Kolka RK, Mitchell CPJ. 2020. Changes in hillslope hydrology in a perched, shallow soil system due to clearcutting and residual biomass removal. *Hydrological Processes* **34** (26): 5354–5369 DOI: https://doi.org/10.1002/hyp.13948

McCormick EL, Dralle DN, Hahm WJ, Tune AK, Schmidt LM, Chadwick KD, Rempe DM. 2021. Widespread woody plant use of water stored in bedrock. *Nature* **597** (7875): 225–229 DOI: 10.1038/s41586-021-03761-3

McGlynn BL, McDonnell JJ. 2003a. Role of discrete landscape units in controlling catchment dissolved organic carbon dynamics. *Water Resources Research* **39** (4) DOI: 10.1029/2002WR001525

McGlynn BL, McDonnell JJ. 2003b. Quantifying the relative contributions of riparian and hillslope zones to catchment runoff: SMALL CATCHMENT RUNOFF SOURCES. *Water Resources Research* **39** (11) DOI: 10.1029/2003WR002091

McLaughlin BC, Ackerly DD, Klos PZ, Natali J, Dawson TE, Thompson SE. 2017. Hydrologic refugia, plants, and climate change. *Global Change Biology* **23** (8): 2941–2961 DOI: 10.1111/gcb.13629

Meerveld HJ van, Seibert J, Peters NE. 2015. Hillslope–riparian-stream connectivity and flow directions at the Panola Mountain Research Watershed. *Hydrological Processes* **29** (16): 3556–3574 DOI: 10.1002/hyp.10508

Meinzer OE. 1927. Plants as Indicators of Groundwater. Scientific Investigations Report. United States Geological Survey, Washington, DC. Available at: https://pubs.usgs.gov/wsp/0577/report.pdf [Accessed 26 January 2022]

Meißner M, Köhler M, Schwendenmann L, Hölscher D, Dyckmans J. 2014. Soil water uptake by trees using water stable isotopes (δ2H and δ18O)—a method test regarding soil moisture, texture and carbonate. *Plant and Soil* **376** (1–2): 327–335 DOI: 10.1007/s11104-013-1970-z

Menció A, Casamitjana X, Mas-Pla J, Coll N, Compte J, Martinoy M, Pascual J, Quintana XD. 2017. Groundwater dependence of coastal lagoons: The case of La Pletera salt marshes (NE Catalonia). *Journal of Hydrology* **552**: 793–806 DOI: 10.1016/j.jhydrol.2017.07.034

Merz R, Blöschl G, Parajka J. 2006. Spatio-temporal variability of event runoff coefficients. *Journal of Hydrology* **331** (3–4): 591–604 DOI: 10.1016/j.jhydrol.2006.06.008

Messer TL, Birgand F, Burchell MR. 2019. Diel fluctuations of high level nitrate and dissolved organic carbon concentrations in constructed wetland mesocosms. *Ecological Engineering* **133**: 76–87 DOI: 10.1016/j.ecoleng.2019.04.027

Michael HA, Mulligan AE, Harvey CF. 2005. Seasonal oscillations in water exchange between aquifers and the coastal ocean. *Nature* **436** (7054): 1145–1148 DOI: 10.1038/nature03935

Minamikawa K, Sakai N. 2007. Soil carbon budget in a single-cropping paddy field with rice straw application and water management based on soil redox potential. *Soil Science and Plant Nutrition* **53** (5): 657–667 DOI: 10.1111/j.1747-0765.2007.00172.x

Murphy AE, Bulseco AN, Ackerman R, Vineis JH, Bowen JL. 2020. Sulphide addition favours respiratory ammonification (DNRA) over complete denitrification and alters the active microbial community in salt marsh sediments. *Environmental Microbiology* **22** (6): 2124–2139 DOI: 10.1111/1462-2920.14969

Nehemy MF, Benettin P, Asadollahi M, Pratt D, Rinaldo A, McDonnell JJ. 2021. Tree water deficit and dynamic source water partitioning. *Hydrological Processes* **35** (1): e14004 DOI: 10.1002/hyp.14004

NERR. 2021. NOAA National Estuarine Research Reserve System (NERRS). System-wide Monitoring Program. Data accessed from the NOAA NERRS Centralized Data Management Office website: www.nerrsdata.org

Nezlin NP, Kamer K, Hyde J, Stein ED. 2009. Dissolved oxygen dynamics in a eutrophic estuary, Upper Newport Bay, California. *Estuarine, Coastal and Shelf Science* **82** (1): 139–151 DOI: 10.1016/j.ecss.2009.01.004

Nippgen F, McGlynn BL, Emanuel RE, Vose JM. 2016. Watershed memory at the Coweeta Hydrologic Laboratory: The effect of past precipitation and storage on hydrologic response: WATERSHED MEMORY AT THE COWEETA HYDROLOGIC LABORATORY. *Water Resources Research* **52** (3): 1673–1695 DOI: 10.1002/2015WR018196

Nivala J, Murphy C, Freeman A. 2020. Recent Advances in the Application, Design, and Operations & Maintenance of Aerated Treatment Wetlands. *Water* **12** (4): 1188 DOI: 10.3390/w12041188

NOAA. 2015. National Centers for Environmental Information, State of the Climate: Hurricanes and Tropical Storms for September 2015 Available at: https://www.ncdc.noaa.gov/sotc/tropical-cyclones/201509 [Accessed 12 May 2020]

O'Dell JW. 1996. DETERMINATION OF NITRATE-NITRITE NITROGEN BY AUTOMATED COLORIMETRY. In *Methods for the Determination of Metals in Environmental Samples*Elsevier; 464–478. DOI: 10.1016/B978-0-8155-1398-8.50026-4

Oerter EJ, Siebert G, Bowling DR, Bowen G. 2019. Soil water vapour isotopes identify missing water source for streamside trees. *Ecohydrology* **12** (4): e2083 DOI: 10.1002/eco.2083

Oeurng C, Sauvage S, Sánchez-Pérez J-M. 2010. Temporal variability of nitrate transport through hydrological response during flood events within a large agricultural catchment in south-west France. *Science of The Total Environment* **409** (1): 140–149 DOI: 10.1016/j.scitotenv.2010.09.006

Orduña-Gaytán F, Vallejo-Cantú NA, Alvarado-Vallejo A, Rosas-Mendoza ES, Sandoval-Herazo LC, Alvarado-Lassman A. 2022. Evaluation of the Removal of Organic Matter and Nutrients in the Co-Treatment of Fruit and Vegetable Waste Using a Bioreactor-Constructed Wetlands System. *Processes* **10** (2): 278 DOI: 10.3390/pr10020278

Osif TL. 1988. The Effects of Salt, Gas, Temperature, and Pressure on the Compressibility of Water. *SPE Reservoir Engineering* **3** (01): 175–181 DOI: 10.2118/13174-PA

Partal T. 2012. Wavelet analysis and multi-scale characteristics of the runoff and precipitation series of the Aegean region (Turkey). *International Journal of Climatology* **32** (1): 108–120 DOI: 10.1002/joc.2245

Paul G, Townsend P, Schmid B, Chong C, Roberson M, Hawkins T, Smith A, Williams D, Kellar C. 2017. California Actual Evapotranspiration Program Available at: http://www.cwemf.org/AMPresentations/2017/s8/3.George_Paul.pdf [Accessed 30 January 2019]

Pedescoll A, Uggetti E, Llorens E, Granés F, García D, García J. 2009. Practical method based on saturated hydraulic conductivity used to assess clogging in subsurface flow constructed wetlands. *Ecological Engineering* **35** (8): 1216–1224 DOI: 10.1016/j.ecoleng.2009.03.016

Penna D, Hopp L, Scandellari F, Allen ST, Benettin P, Beyer M, Geris J, Klaus J, Marshall JD, Schwendenmann L, et al. 2018. Tracing ecosystem water fluxes using hydrogen and oxygen stable isotopes: challenges and opportunities from an

interdisciplinary perspective. *Biogeosciences Discussions*: 1–23 DOI: 10.5194/bg-2018-286

Petersen NR-, Rysgaard S, Nielsen LP, Revsbech NP. 1994. Diurnal variation of denitrification and nitrification in sediments colonized by benthic microphytes. *Limnology and Oceanography* **39** (3): 573–579 DOI: 10.4319/lo.1994.39.3.0573

Peterson RN, Moore WS, Chappel SL, Viso RF, Libes SM, Peterson LE. 2016. A new perspective on coastal hypoxia: The role of saline groundwater. *Marine Chemistry* **179**: 1–11 DOI: 10.1016/j.marchem.2015.12.005

Quiroz R, Yarlequé C, Posadas A, Mares V, Immerzeel WW. 2011. Improving daily rainfall estimation from NDVI using a wavelet transform. *Environmental Modelling & Software* **26** (2): 201–209 DOI: 10.1016/j.envsoft.2010.07.006

R Core Team. 2019. *R: A Language and Environment for Statistical Computing*. R Fundation for Statistical Computing. Available at: https://www.R-project.org/

R Core Team. 2021. *R: A language and environment for statistical computing. R Foundation for Statistical Computing*. Vienna, Austria. Available at: https://www.R-project.org/

Reading MJ, Santos IR, Maher DT, Jeffrey LC, Tait DR. 2017. Shifting nitrous oxide source/sink behaviour in a subtropical estuary revealed by automated time series observations. *Estuarine, Coastal and Shelf Science* **194**: 66–76 DOI: 10.1016/j.ecss.2017.05.017

Reaver NGF, Kaplan DA, Klammler H, Jawitz JW. 2022. Theoretical and empirical evidence against the Budyko catchment trajectory conjecture. *Hydrology and Earth System Sciences* **26** (5): 1507–1525 DOI: 10.5194/hess-26-1507-2022

Rempe DM, Dietrich WE. 2018. Direct observations of rock moisture, a hidden component of the hydrologic cycle. *Proceedings of the National Academy of Sciences* **115** (11): 2664–2669 DOI: 10.1073/pnas.1800141115

Richter DD, Markewitz D, Heine PR, Jin V, Raikes J, Tian K, Wells CG. 2000. Legacies of agriculture and forest regrowth in the nitrogen of old-field soils. *Forest Ecology and Management* **138** (1): 233–248 DOI: 10.1016/S0378-1127(00)00399-6

Rinderer M, Meerveld I van, Stähli M, Seibert J. 2016. Is groundwater response timing in a pre-alpine catchment controlled more by topography or by rainfall? *Hydrological Processes* **30** (7): 1036–1051 DOI: https://doi.org/10.1002/hyp.10634

Robinson CE, Xin P, Santos IR, Charette MA, Li L, Barry DA. 2018. Groundwater dynamics in subterranean estuaries of coastal unconfined aquifers: Controls on submarine groundwater discharge and chemical inputs to the ocean. *Advances in Water Resources* **115**: 315–331 DOI: 10.1016/j.advwatres.2017.10.041

Rose S, Peters NE. 2001. Effects of urbanization on streamflow in the Atlanta area (Georgia, USA): a comparative hydrological approach. *Hydrological Processes* **15** (8): 1441–1457 DOI: https://doi.org/10.1002/hyp.218

Rosner B, Grove D. 1999. Use of the Mann–Whitney U-test for clustered data. *Statistics in Medicine* **18** (11): 1387–1400 DOI: 10.1002/(SICI)1097-0258(19990615)18:11<1387::AID-SIM126>3.0.CO;2-V

Rossi MW, Whipple KX, Vivoni ER. 2016. Precipitation and evapotranspiration controls on daily runoff variability in the contiguous United States and Puerto Rico. *Journal of Geophysical Research: Earth Surface* **121** (1): 128–145 DOI: 10.1002/2015JF003446

Rouholahnejad Freund E, Kirchner JW. 2017. A Budyko framework for estimating how spatial heterogeneity and lateral moisture redistribution affect average evapotranspiration rates as seen from the atmosphere. *Hydrology and Earth System Sciences* **21** (1): 217–233 DOI: 10.5194/hess-21-217-2017

Russo TA, Fisher AT, Winslow DM. 2013. Regional and local increases in storm intensity in the San Francisco Bay Area, USA, between 1890 and 2010: STORM INTENSITY IN THE SFBA. *Journal of Geophysical Research: Atmospheres* **118** (8): 3392–3401 DOI: 10.1002/jgrd.50225

Santos IR, Eyre BD, Huettel M. 2012. The driving forces of porewater and groundwater flow in permeable coastal sediments: A review. *Estuarine, Coastal and Shelf Science* **98**: 1–15 DOI: 10.1016/j.ecss.2011.10.024

Sarkar S, Pandey B. 2020. A study on the statistical significance of mutual information between morphology of a galaxy and its large-scale environment. *Monthly Notices of the Royal Astronomical Society* **497** (4): 4077–4090 DOI: 10.1093/mnras/staa2236

Schlesinger WH, Jasechko S. 2014. Transpiration in the global water cycle. *Agricultural and Forest Meteorology* **189–190**: 115–117 DOI: 10.1016/j.agrformet.2014.01.011

Schultz BB. 1985. Levene's Test for Relative Variation. *Systematic Biology* **34** (4): 449–456 DOI: 10.1093/sysbio/34.4.449

Shannon CE, Weaver W. 1949. The mathematical theory of communication

Shapiro SS, Wilk MB. 1965. An Analysis of Variance Test for Normality (Complete Samples). *Biometrika* **52** (3/4): 591–611 DOI: 10.2307/2333709

Silver W, Leon M. 2019. Precipitation, Reservoir Height, Streamflow / Discharge -- Schoolyard Data Jam -- Puerto Rico -- (1990-2016). *HydroShare*

Singh NK, Emanuel RE, Nippgen F, McGlynn BL, Miniat CF. 2018. The Relative Influence of Storm and Landscape Characteristics on Shallow Groundwater Responses in Forested Headwater Catchments. *Water Resources Research* **54** (12): 9883–9900 DOI: https://doi.org/10.1029/2018WR022681

Sinha E, Michalak AM, Balaji V. 2017. Eutrophication will increase during the 21st century as a result of precipitation changes. *Science* **357** (6349): 405–408 DOI: 10.1126/science.aan2409

Søndergaard M. 2009. Redox Potential. In *Encyclopedia of Inland Waters*, Likens GE (ed.).Academic Press: Oxford; 852–859. DOI: 10.1016/B978-012370626-3.00115-0

Soulsby C, Birkel C, Geris J, Dick J, Tunaley C, Tetzlaff D. 2015. Stream water age distributions controlled by storage dynamics and nonlinear hydrologic connectivity: Modeling with high-resolution isotope data. *Water Resources Research* **51** (9): 7759–7776 DOI: 10.1002/2015WR017888

Spence C. 2010. A Paradigm Shift in Hydrology: Storage Thresholds Across Scales Influence Catchment Runoff Generation: Paradigm shift in hydrology. *Geography Compass* **4** (7): 819–833 DOI: 10.1111/j.1749-8198.2010.00341.x

Spence C, Guan XJ, Phillips R, Hedstrom N, Granger R, Reid B. 2010. Storage dynamics and streamflow in a catchment with a variable contributing area. *Hydrological Processes* **24** (16): 2209–2221 DOI: 10.1002/hyp.7492

Sprenger M, Leistert H, Gimbel K, Weiler M. 2016. Illuminating hydrological processes at the soil-vegetation-atmosphere interface with water stable isotopes. *Reviews of Geophysics* **54** (3): 674–704 DOI: 10.1002/2015RG000515

Steinmuller HE, Chambers LG. 2019. Characterization of coastal wetland soil organic matter: Implications for wetland submergence. *Science of The Total Environment* **677**: 648–659 DOI: 10.1016/j.scitotenv.2019.04.405

Stieglitz TC, Clark JF, Hancock GJ. 2013. The mangrove pump: The tidal flushing of animal burrows in a tropical mangrove forest determined from radionuclide budgets. *Geochimica et Cosmochimica Acta* **102**: 12–22 DOI: 10.1016/j.gca.2012.10.033

Sujono J, Shikasho S, Hiramatsu K. 2004. A comparison of techniques for hydrograph recession analysis. *Hydrological Processes* **18** (3): 403–413 DOI: 10.1002/hyp.1247

Swain DL, Langenbrunner B, Neelin JD, Hall A. 2018. Increasing precipitation volatility in twenty-first-century California. *Nature Climate Change* **8** (5): 427–433 DOI: 10.1038/s41558-018-0140-y

Taillardat P, Ziegler AD, Friess DA, Widory D, David F, Ohte N, Nakamura T, Evaristo J, Thanh-Nho N, Van Vinh T, et al. 2019. Assessing nutrient dynamics in mangrove porewater and adjacent tidal creek using nitrate dual-stable isotopes: A new approach to challenge the Outwelling Hypothesis? *Marine Chemistry* **214**: 103662 DOI: 10.1016/j.marchem.2019.103662

Tait DR, Maher DT, Macklin PA, Santos IR. 2016. Mangrove pore water exchange across a latitudinal gradient. *Geophysical Research Letters* **43** (7): 3334–3341 DOI: 10.1002/2016GL068289

Taniguchi M. 2000. Evaluations of the saltwater-groundwater interface from borehole temperature in a coastal region. *Geophysical Research Letters* **27** (5): 713–716 DOI: 10.1029/1999GL002366

Tatariw C, Mortazavi B, Ledford TC, Starr SF, Smyth E, Griffin Wood A, Simpson LT, Cherry JA. 2021. Nitrate reduction capacity is limited by belowground plant recovery in a 32-year-old created salt marsh. *Restoration Ecology* **29** (1): e13300 DOI: 10.1111/rec.13300

The MathWorks I. 2021. MATLAB Wavelet Toolbox. MathWorks, Inc.: Natick, Massachusetts, US.

Thornthwaite CW. 1948a. An approach toward a rational classification of climate. *Geographical review* **38** (1): 55–94

Thornthwaite CW. 1948b. An Approach toward a Rational Classification of Climate. *Geographical Review* **38** (1): 55–94 DOI: 10.2307/210739

Torrence C, Compo GP. 1998. A Practical Guide to Wavelet Analysis. *Bulletin of the American Meteorological Society* **79** (1): 18

Tromp-van Meerveld HJ, McDonnell JJ. 2006. Threshold relations in subsurface stormflow: 2. The fill and spill hypothesis. *Water Resources Research* **42** (2) DOI: 10.1029/2004WR003800

Turner IL, Coates BP, Acworth RI. 1997. Tides, Waves and the Super-elevation of Groundwater at the Coast. *Journal of Coastal Research* **13** (1): 46–60

Valiela I, Cole ML. 2002. Comparative Evidence that Salt Marshes and Mangroves May Protect Seagrass Meadows from Land-derived Nitrogen Loads. *Ecosystems* **5** (1): 92–102 DOI: 10.1007/s10021-001-0058-4

Van Dop M, Hall A, Calhoun K, Kislik C. 2019. Linking land cover and water quality in Elkhorn Slough. Elkhorn Slough Technical Report Series. Elkhorn Slough, CA. Available at:

http://library.elkhornslough.org/attachments/VanDop_2019_Linking_Land_Cover_And.pdf [Accessed 11 April 2022]

Van Dyke E, Wasson K. 2005. Historical ecology of a central California estuary: 150 years of habitat change. *Estuaries* **28** (2): 173–189 DOI: 10.1007/BF02732853

Vaughan MCH, Bowden WB, Shanley JB, Vermilyea A, Sleeper R, Gold AJ, Pradhanang SM, Inamdar SP, Levia DF, Andres AS, et al. 2017. High-frequency dissolved organic carbon and nitrate measurements reveal differences in storm hysteresis and loading in relation to land cover and seasonality. *Water Resources Research* **53** (7): 5345–5363 DOI: 10.1002/2017WR020491

Vaughan MCH, Bowden WB, Shanley JB, Vermilyea A, Wemple B, Schroth AW. 2018. Using in situ UV-Visible spectrophotometer sensors to quantify riverine phosphorus partitioning and concentration at a high frequency. *Limnology and Oceanography: Methods* **16** (12): 840–855 DOI: 10.1002/lom3.10287

Venkatesh S, Arora B, Dwivedi D, Vezhapperambu S, Ramesh MV. 2021. Temporal Variability of Water Quality Parameters at the Elkhorn Slough Estuary using Wavelets. In *2021 6th International Conference for Convergence in Technology (I2CT)*1–5. DOI: 10.1109/I2CT51068.2021.9418159

Volkmann THM, Kühnhammer K, Herbstritt B, Gessler A, Weiler M. 2016. A method for in situ monitoring of the isotope composition of tree xylem water using laser spectroscopy. *Plant, Cell & Environment* **39** (9): 2055–2063 DOI: 10.1111/pce.12725

Vorenhout M, van der Geest HG, Hunting ER. 2011. An improved datalogger and novel probes for continuous redox measurements in wetlands. *International Journal of*

Environmental Analytical Chemistry **91** (7–8): 801–810 DOI: 10.1080/03067319.2010.535123

Vorenhout M, van der Geest HG, van Marum D, Wattel K, Eijsackers HJP. 2004. Automated and Continuous Redox Potential Measurements in Soil. *Journal of Environmental Quality* **33** (4): 1562–1567 DOI: 10.2134/jeq2004.1562

Wagener T, Sivapalan M, Troch P, Woods R. 2007. Catchment Classification and Hydrologic Similarity. *Geography Compass* **1** (4): 901–931 DOI: 10.1111/j.1749-8198.2007.00039.x

Wallace CD, Soltanian MR. 2021. Underlying riparian lithology controls redox dynamics during stage-driven mixing. *Journal of Hydrology* **595**: 126035 DOI: 10.1016/j.jhydrol.2021.126035

Wallace CD, Sawyer AH, Barnes RT. 2019. Spectral analysis of continuous redox data reveals geochemical dynamics near the stream–aquifer interface. *Hydrological Processes* **33** (3): 405–413 DOI: 10.1002/hyp.13335

Wang F, Xiao K, Santos IR, Lu Z, Tamborski J, Wang Y, Yan R, Chen N. 2022. Porewater exchange drives nutrient cycling and export in a mangrove-salt marsh ecotone. *Journal of Hydrology* **606**: 127401 DOI: 10.1016/j.jhydrol.2021.127401

Wang QJ, Pagano TC, Zhou SL, Hapuarachchi HAP, Zhang L, Robertson DE. 2011. Monthly versus daily water balance models in simulating monthly runoff. *Journal of Hydrology* **404** (3): 166–175 DOI: 10.1016/j.jhydrol.2011.04.027

Wankel SD, Germanovich LN, Lilley MD, Genc G, DiPerna CJ, Bradley AS, Olson EJ, Girguis PR. 2011. Influence of subsurface biosphere on geochemical fluxes from

diffuse hydrothermal fluids. *Nature Geoscience* **4** (7): 461–468 DOI: 10.1038/ngeo1183

Wankel SD, Kendall C, Paytan A. 2009. Using nitrate dual isotopic composition (δ^{15} N and δ^{18} O) as a tool for exploring sources and cycling of nitrate in an estuarine system: Elkhorn Slough, California. *Journal of Geophysical Research* **114** (G1): G01011 DOI: 10.1029/2008JG000729

Wlostowski AN, Molotch N, Anderson SP, Brantley SL, Chorover J, Dralle D, Kumar P, Li L, Lohse KA, Mallard JM, et al. 2021. Signatures of Hydrologic Function Across the Critical Zone Observatory Network. *Water Resources Research* **57** (3): e2019WR026635 DOI: https://doi.org/10.1029/2019WR026635

Wong LS, Hashim R, Ali FH. 2009. A Review on Hydraulic Conductivity and Compressibility of Peat. *Journal of Applied Sciences* **9** (18): 3207–3218 DOI: 10.3923/jas.2009.3207.3218

Woolfolk A, Labadie Q. 2012. The significance of pickleweed-dominated tidal salt marsh in Elkhorn Slough, California: A literature review. Technical Report Series. Elkhorn Slough.

Xie T, Li S, Cui B, Bai J, Wang Q, Shi W. 2019. Rainfall variation shifts habitat suitability for seedling establishment associated with tidal inundation in salt marshes. *Ecological Indicators* **98**: 694–703 DOI: 10.1016/j.ecolind.2018.11.056

Yokoo Y, Sivapalan M, Oki T. 2008. Investigating the roles of climate seasonality and landscape characteristics on mean annual and monthly water balances. *Journal of Hydrology* **357** (3): 255–269 DOI: 10.1016/j.jhydrol.2008.05.010

Zbili M, Rama S. 2021. A Quick and Easy Way to Estimate Entropy and Mutual Information for Neuroscience. *Frontiers in Neuroinformatics* **15**: 25 DOI: 10.3389/fninf.2021.596443

Zehe E, Becker R, Bárdossy A, Plate E. 2005. Uncertainty of simulated catchment runoff response in the presence of threshold processes: Role of initial soil moisture and precipitation. *Journal of Hydrology* **315** (1–4): 183–202 DOI: 10.1016/j.jhydrol.2005.03.038

Zhang X, Zhao X-M, He K, Lu L, Cao Y, Liu J, Hao J-K, Liu Z-P, Chen L. 2012. Inferring gene regulatory networks from gene expression data by path consistency algorithm based on conditional mutual information. *Bioinformatics* **28** (1): 98–104 DOI: 10.1093/bioinformatics/btr626

Zheng Y, Hou L, Liu M, Liu Z, Li X, Lin X, Yin G, Gao J, Yu C, Wang R, et al. 2016. Tidal pumping facilitates dissimilatory nitrate reduction in intertidal marshes. *Scientific Reports* **6** (1): 21338 DOI: 10.1038/srep21338

Zhou Q, Birkholzer JT, Javandel I, Jordan PD. 2003. Simulation of Groundwater Flow at the LBNL Site using TOUGH2. *Proceedings, TOUGH Symposium 2003. Lawrence Berkeley National Laboratory, Berkeley, California, May12-14, 2003*: 8

Zimmerman J. 2018. Meteorological data from El Verde Field Station: NADP Tower ver 1676158. *Environmental Data Initiative* Available at: https://doi.org/10.6073/pasta/d62b391ee1c4e26f918526095a8531ab [Accessed 23 April 2020]

Zuecco G, Penna D, Borga M, van Meerveld HJ. 2016. A versatile index to characterize hysteresis between hydrological variables at the runoff event timescale: A

Hysteresis Index for Variables at the Runoff Event Timescale. *Hydrological Processes* **30** (9): 1449–1466 DOI: 10.1002/hyp.10681